Hydrodynamic coefficients of a free floating barrier in regular waves

J.M.P. Flick

TU Delft

Hydrodynamic coefficients of a free floating barrier in regular waves

by

J.M.P. Flick

to obtain the degree of Master of Science
at the Delft University of Technology,
to be defended publicly on Tuesday May 29, 2018

Student number:	1533916	
Project duration:	December 1, 2015 – May 29, 2018	
Thesis committee:	Prof. dr. ir. M.L. Kaminski,	TU Delft, chairman
	Dr. ir. P.R. Wellens,	TU Delft
	Dr. ir. S.A. Miedema,	TU Delft
	Dr. ir. B. Sainte-Rose,	The Ocean Cleanup, daily supervisor

An electronic version of this thesis is available at http://repository.tudelft.nl/.

Abstract

The Ocean Cleanup plans to deploy a barrier array, to concentrate and capture plastic in the North Pacific gyre by 2020. Both shape and behaviour of the barrier are quite different from the most marine structures.

To get an estimation of the behaviour and loads on the system, the system has been modelled by The Ocean Cleanup in Orcaflex. This software uses the Morison equation. The hydrodynamic coefficients used in this equation are obtained from experiments with cylinders far from the free surface. Using these coefficients with the Morison equation is a generally accepted method to estimate the loads on submerged cylinders such as piles. However, the barrier is in the free surface and free to move.

This research focuses on the determination of the hydrodynamic coefficients of an unconstrained floating barrier. A model has been set up to evaluate the hydrodynamic coefficients of a floating barrier in regular waves. The barrier was simulated using a numerical model as wave tank. This numerical wave tank has been preliminarily verified with the linear wave theory, in order to optimise the mesh resolution. The numerical model uses fluid-structure interaction to model the flow around a rigid body, the barrier. The hydrodynamic coefficients were in post-processing determined from the response of the numerical model, with the Morison equation, by means of a least squares method.

The barrier with 2 degrees of freedom, sway and heave, has been compared to model tests performed at MARIN with 3 degrees of freedom, sway, heave and roll. The model with 2 degrees of freedom shows reasonable comparison in waves. These results found in this thesis indicate that the mass coefficient, C_m of the barrier in both the horizontal and vertical plane is close to zero. The drag coefficient, C_d in the vertical plane is close to zero, in the horizontal plane C_d is close to 0.5, both show resemblance to results found in literature.

Contents

List of Figures

List of Tables

List of Scripts

Nomenclature

Abbreviation

TOC	The Ocean Cleanup	

List of Symbols

α_g	gravity scaling factor	$[-]$
α_L	length scaling factor	$[-]$
α_T	time scaling factor	$[-]$
α_v	velocity scaling factor	$[-]$
$\dot{Q}$	rate of heat	$[\mathcal{J}]$
$\dot{W}$	rate of work	$[\mathcal{J}]$
η	surface elevation	$[m]$
λ	bulk viscosity coefficient	$[-]$
λ	wave length	$[m]$
$\mathbf{V}$	velocity vector	$[m/s]$
$\mathcal{J}$	Joule	$[kg \cdot m^2/s^2]$
$\mathcal{V}$	volume	$[m^3]$
μ	dynamic viscosity	$[kg/m \cdot s]$
ω	angular frequency, $\omega = 2\pi/T$	$[rad/s]$
ρ	density	$[kg/m^3]$
dof-yz	system free in sway and heave	$[-]$
dof-y	system free in sway	$[-]$
dof-z	system free in heave	$[-]$
a	wave amplitude, $H/2$	$[m]$
A_h	projected average area in heave, or Area$\perp_z$,	$[m^2]$
a_{ij}	added mass	$[kg]$
A_{s_h}	high water level projected area in sway,	$[m^2]$
A_s	projected average area in sway, or Area$\perp_y$,	$[m^2]$
b_{ij}	damping	$[N/ms]$
C_a	added mass, or added mass moment of inertia coefficient	$[-]$
C_d	damping coefficient	$[-]$
C_d	drag coefficient	$[-]$

C_m	mass or inertia coefficient	$[-]$
c_{ij}	restoring constant	$[N/m]$
CFL	Courant Friedrichs Lewy number	$[-]$
D	diameter	$[m]$
d	water depth	$[m]$
e	internal energy per unit mass	$[J/kg]$
F	force	$[N]$
f	force per length	$[N/m]$
Fr	Froude number	$[-]$
H	wave height	$[m]$
K	deep water wave number	$[-]$
k	wave number, $k = 2\pi/L$	$[rad/m]$
KC	Keulegan Carpenter number	$[-]$
L	length scale	$[m]$
L	wave length	$[m]$
m_{ij}	mass, or mass moment of inertia	$[kg]$
p	pressure	$[N/m^2]$
R	radius, $D/2$	$[m]$
r	motion of the structure	$[m]$
Re	Reynolds number	$[-]$
S	surface	$[m^2]$
T	wave period	$[s]$
U	Velocity	$[m/s]$
V	submerged volume	$[m^3]$
V	velocity	$[m/s]$
bay	acceleration of the system in the sway	$[m/s^2]$
baz	acceleration of the system in the heave direction	$[m/s^2]$
buy	y location of the system relative to its starting position	$[m]$
buz	z location of the system relative to its starting position	$[m]$
bvy	velocity of the system in the sway	$[m/s]$
bvz	velocity of the system in heave	$[m/s]$
wvy	wave velocity in sway at $[2 \cdot \lambda,\ d + (H/2 - \overline{A_s})]$	$[m/s]$
wvz	wave velocity in heave at $[2 \cdot \lambda,\ d - H/2]$	$[m/s]$

1 Introduction

In this thesis project, the dynamic behaviour of a barrier in waves will be investigated. This will be done using computational fluid dynamics.

The project was sponsored by The Ocean Cleanup, a company focused on removing plastic from the ocean. Yearly about 8 million tons of plastic enters the ocean, which accumulates in the 5 ocean gyres. A third of the plastic is concentrated in the Great Pacific Gyre (or garbage patch). The plastic causes harm to the economy, for example beaches filled are with plastic, for example the environment when birds and fish eat the plastic or the plastic serves as a carrier to invasive species, and lastly to our health. The plastic adsorbs chemicals and is accumulated in the food chain. The Ocean Cleanup's goal is to extract, prevent and intercept plastic pollution. The objective of The Ocean Cleanup is to deploy a barrier array, to concentrate and capture plastic in the North Pacific Gyre by 2020.

To get an estimation of the behaviour and the loads on the system, it has been modelled in Orcaflex by The Ocean Cleanup. In these simulations, the flow is idealised and the influence of the system on the flow field is neglected. This results in underestimation of the high frequency loads, and an overestimation of the low frequency loads [42].
Another approach to get an estimation of the loads is to model the flow around a constrained barrier, which has been done with both ANANAS and Fluent. With this approach the deformation and motion of the system due to the wave loads are neglected. Both approaches disregard the (strong) coupling between the flow and the structure.

Initially, this thesis aimed to model both transient flow as well as structural mechanics, providing a better representation of the behaviour of the system. However this proved to be too complex and the aim has been simplified. Now this thesis aims to determine the hydrodynamic coefficients for a system with 2 degrees of freedom, sway and heave.
The hydrodynamic coefficients currently used are obtained from experiments with cylinders far from the free surface. Using these coefficients with the Morison equation is a generally accepted method to estimate loads on vertical cylinders such as piles. However, the barrier, is free to move and in the free surface.

The validation will be performed with flume tests carried out with MARIN in 2016.

2 The Ocean Cleanup

2.1. The Ocean Cleanup barrier

The Ocean Cleanup aims to concentrate, catch and remove the floating plastic. This will be done by means of an artificial coast line, the barrier. The barrier consists of a floater, the boom, and a screen, or skirt. The boom and the skirt will concentrate and catch the plastic. A visualisation of a barrier can be found in Figure 2.1.

The Ocean Cleanup array is made of long floating barriers which capture and concentrate the plastic, making mechanical extraction possible [41].
The objective of The Ocean Cleanup ("TOC") is to deploy this type of array in the North Pacific gyre by 2020. The boom will have a diameter of approximately 1.2 m, and the skirt will have a depth between 1 and 2 m. The boom will be flexible, such that it follows the waves, see Figure 2.1a. Two mooring setup were considered. Figure 2.1b shows the high mooring setup and Figure 2.1c shows the low mooring setup.

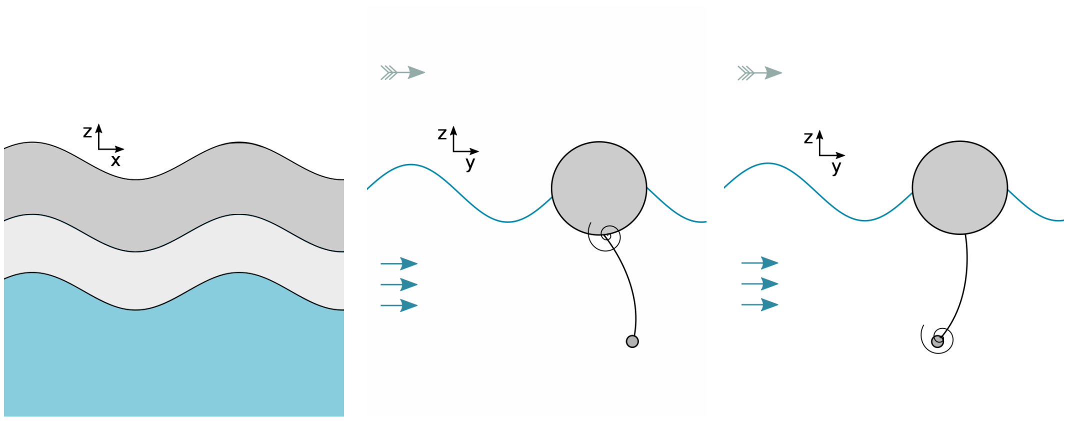

(a) front view of the array (b) High mooring (c) Low mooring

Figure 2.1: Schematic view of the flexible barrier concepts, as of spring 2016

An overview of the environmental conditions in the North pacific gyre is given in Table 2.1. The temperature of the top water can be assumed to be constant over the depth due to mixing by wind and waves [34].

2.2. Model tests

To investigate the forces on a barrier, several tests have been performed at both Deltares and MARIN, as well as the prototype being tested in the North Sea.
In June 2015, a model was tested at Deltares. The aim of the tests performed at Deltares was to determine the behaviour of plastic in the ocean in relation to the barrier, and to measure forces on the barrier due to wave and current action for future validation of numerical models [14], [42].

Table 2.1: Median values in location (31°N - 142 °W) [41]

Quantity	Value	Unit
wind velocity at 10 m height	6.05	m/s
current	0.13	m/s
significant wave height	2.09	m
mean wave period	8.09	s
sea surface temperature	22	$^\circ C$
water density	1025	kg/m^3

In October 2015 a flexible model was tested in MARIN in the Offshore Basin at scale 1:18 with respect to the concept for the pacific. The tests were used to validate and calibrate 3D models for the design of the barrier and the mooring system in the vertical plane and to provide an understanding of the response of a system in waves and current [33]

In June 2016, a semi 2D flexible model, similar to the North Sea Prototype Desmi barrier, was tested in the MARIN Concept Basin, at 1:5 scale.

In this thesis, the system is modelled in a flow solver, ANSYS Fluent, as a rigid body, with up to two degrees of freedom, sway and heave.

3

Ocean Waves

3.1. Linear wave theory

An ocean wave can be modelled with linear wave theory, with the following assumptions and idealisations:

- The fluid is incompressible or the density is constant. This assumption can be made in the open ocean, as the scales, both vertical and horizontal, over which the density varies are much larger than the wave length.
- The fluid is assumed to be inviscid. Viscous forces are important on a small scale, but for a regular ocean wave these internal forces can be neglected.
- The wave generation due to wind induced pressure is neglected.
- The surface tension can be neglected. This means that the waves have to be bigger than a few centimetres. On a larger scale, the Coriolis force is neglected. As the scale of the Coriolis forces comes into play on a scale of several kilometres, see Appendix E.3.6, this simplification is allowed.
- The bottom friction is neglected as well. This assumption can be made as the bottom friction is a local effect. The disturbances caused by the friction do not influence the main water body.
- The flow is irrotational, this assumption follows from the assumption that the flow has no friction, because the disturbances which would be generated at the bottom, do not travel into the main water body. [15]

3.2. Linearised balance equations

If the assumptions are applied to the balance equations as described in Appendix E, the following equations are obtained. The coordinate system is shown in Figure 3.1

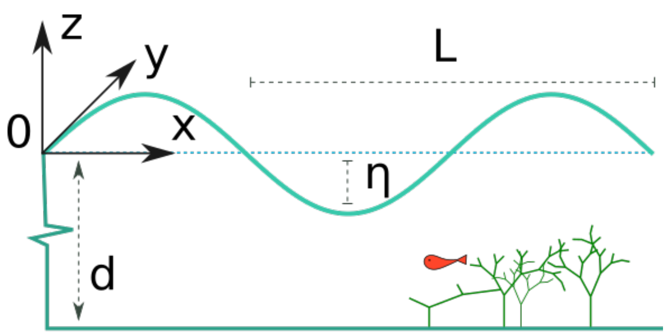

Figure 3.1: Coordinate system

In 3.1, L, or λ represents the wave length, η the water level and d the water depth.

3.2.1. Continuity equation

Starting with mass conservation, 3.1

$$\frac{\partial \rho}{\partial t} + \nabla \cdot (\rho \mathbf{V}) = 0 \tag{3.1}$$

For incompressible flows this reduces to

$$\nabla \cdot (\rho \mathbf{V}) = 0 \tag{3.2}$$

If the density is assumed to be constant, the derivatives of ρ are zero, and the density can be removed from the equation. This results in

$$\nabla \cdot \mathbf{V} = \frac{\partial u_x}{\partial x} + \frac{\partial u_y}{\partial y} + \frac{\partial u_z}{\partial z} = 0 \tag{3.3}$$

In this equation **V** represents the velocity vector. If the flow is assumed to be irrotational, the vorticity is zero, $\xi = \nabla \times \mathbf{V} = 0$. If ϕ is a scalar function, then

$$\nabla \times (\nabla \phi) = 0 \tag{3.4}$$

[2],the gradient of scalar function is zero, and

$$\mathbf{V} = \nabla \phi \tag{3.5}$$

Substituting Equation 3.5 into Equation 3.3, results in the Laplace equation

$$\frac{\partial^2 \phi}{\partial x^2} + \frac{\partial^2 \phi}{\partial y^2} + \frac{\partial^2 \phi}{\partial z^2} = 0 \tag{3.6}$$

3.2.2. Momentum equations

To create the momentum equation describing the ocean wave, the momentum balance along the x direction, can b written as

$$\frac{\rho \partial (u)}{\partial t} + \nabla \cdot (\rho u \mathbf{V}) = \frac{\partial p}{\partial x} + \rho f_x + (F_x)_{viscous}$$

The flow is assumed to be incompressible, $\frac{\rho \partial}{\partial t} = 0$, and inviscid, $F_{x viscous} = 0$,

$$\frac{\partial (\rho u)}{\partial t} + \nabla \cdot (\rho u \mathbf{V}) = \frac{\partial p}{\partial x} + \rho f_x \tag{3.7}$$

Linearising the equations results in

$$\begin{aligned}
\frac{\delta u}{\delta t} &= -\frac{1}{\rho}\frac{\delta p}{\delta x} \\
\frac{\delta v}{\delta t} &= -\frac{1}{\rho}\frac{\delta p}{\delta y} \\
\frac{\delta w}{\delta t} &= -\frac{1}{\rho}\frac{\delta p}{\delta z} - g
\end{aligned} \tag{3.8}$$

3.2.3. Boundary conditions

In order to model the problem, boundary conditions have to be set. The first kinematic boundary condition states that water cannot penetrate the bottom. In the following equation, d represents the depth,

$$u_z = \frac{\partial \phi}{\partial z} = 0 \qquad \text{at } z = -d \tag{3.9}$$

The second kinematic boundary condition; water cannot leave the surface, thus the water velocity is equal to the velocity of the surface

$$u_z = \frac{\partial \phi}{\partial z} = \frac{\partial \eta}{\partial t} \qquad \text{at } z = 0 \tag{3.10}$$

At the water surface the pressure is constant, and is set to zero, resulting in the dynamic surface boundary condition. Substituting this in Equation 3.8 and rearranging, this results in

$$p = 0 \qquad \text{at } z = 0 \tag{3.11}$$

$$\frac{\partial \phi}{\partial t} + \frac{p}{\rho} + gz = \frac{\partial \phi}{\partial t} + gz = 0 \qquad \text{at } z = 0 \tag{3.12}$$

3.3. Harmonic wave

The surface elevation of a harmonic propagating wave can be described with equation 3.13, which is an analytical solution the Laplace equation, Equation 3.6.

$$\eta(x,t) = a\sin(\omega t - kx) \tag{3.13}$$

a is the wave amplitude with $a = H/2$, where H is the wave height, $\omega = \frac{2\pi}{T}$, represents the wave frequency and $k = \frac{2\pi}{L}$, the wave number.
The velocity with which the wave propagates, or the wave speed, can be described as

$$c = \frac{dx}{dt} = \frac{\omega}{k} = \frac{L}{T} \tag{3.14}$$

The velocity potential of the function is given in the following equation

$$\phi = \hat{\phi}\cos(\omega t - kx) \qquad \text{with } \hat{\phi} = \frac{\omega a}{k}\frac{\cosh[k(d+z)]}{\sinh(kd)} \tag{3.15}$$

The particle velocity can be obtained from the velocity potential ϕ with Equation 3.5, recall

$$u_x = \hat{u}_x\sin(\omega t - kx) \qquad \text{with } \hat{u}_x = \omega a\frac{\cosh[k(d+z])}{\sinh(kd)} \tag{3.16}$$

$$u_z = \hat{u}_z\cos(\omega t - kx) \qquad \text{with } \hat{u}_z = \omega a\frac{\sinh[k(d+z])}{\sinh(kd)} \tag{3.17}$$

Substituting Equation 3.13 and 3.15 in Equation 3.10 results in the dispersion relationship, which gives the relation between the radian frequency ω and the wave number k. From the dispersion relationship the wave length as a function of the water depth can be determined:

$$\omega^2 = gk\tanh(kd) \tag{3.18}$$

As the water becomes less deep, the wave length decreases. The wave length as function of the water depth can be determined with the dispersion relationship:

$$L = \frac{gT^2}{2\pi}\tanh\left(\frac{2\pi d}{L}\right) \tag{3.19}$$

Linear wave theory assumes that a random ocean wave consists of a summation of several independent harmonic waves:

$$\eta(x,t) = \sum_{i=1}^{N} a_i\cos(\omega_i t - k_i x) \tag{3.20}$$

The water elevation at location x, due to a series of waves can also be written as

$$\eta(t) = \sum_{i=1}^{N} a_i\cos(2\pi f_i t + \alpha_i) \tag{3.21}$$

Where $f_i = \frac{i}{D}$, represents a component with frequency f_i, D represents the duration and $D = \frac{i}{f_i} = iT_i$ where T_i is the wave period, [15]. With the trigonometric identities this can be rewritten to

$$\eta(t) = \sum_{i=1}^{N}\big(A_i\cos(2\pi f_i t) + B_i\sin(2\pi f_i t)\big) \tag{3.22}$$

where

$$a_i = \sqrt{A_i^2 + B_i^2} \qquad \text{and } \alpha_i = \arctan\left(-\frac{B_i}{A_i}\right) \tag{3.23}$$

A series of waves measured over a longer time, forms a spectrum.

$$E(f) = \lim_{\Delta f\to 0}\frac{1}{\Delta f}E\{\frac{1}{2}a_i^2\} \tag{3.24}$$

A wave can be described with the linear wave theory when the wave steepness is small and the influence of the water depth is small. Together the wave steepness, $\frac{H}{gT^2}$ and water depth to wave length ratio, $\frac{d}{gT^2}$, remains within the boundaries shown in 3.2. [15] [21]

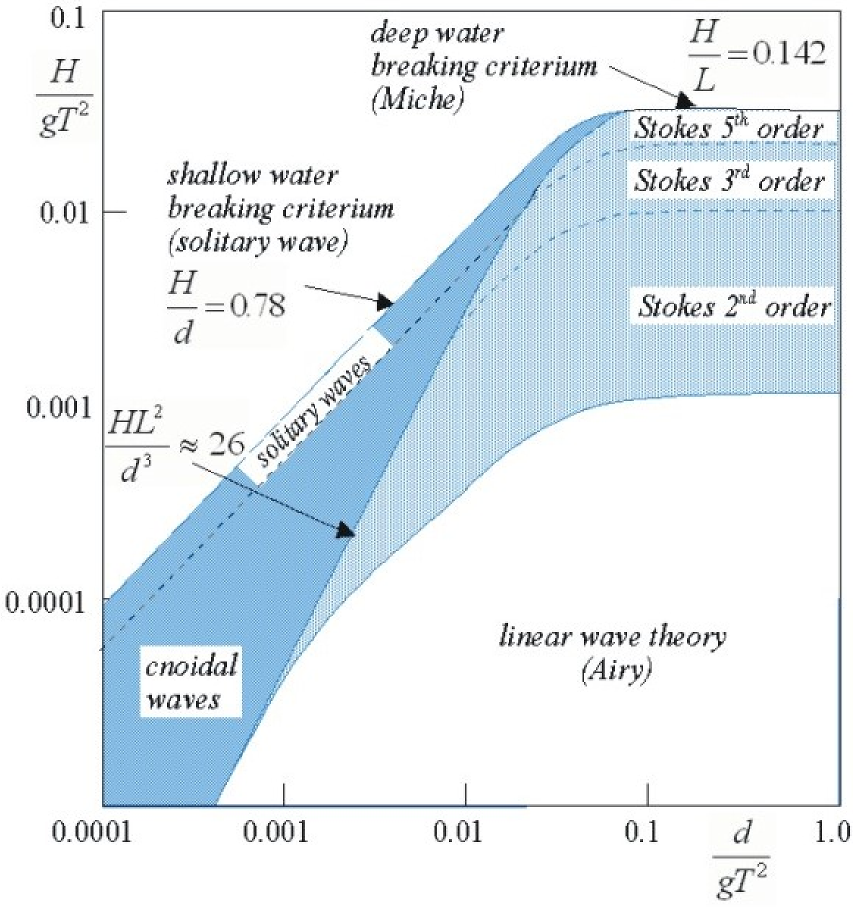

Figure 3.2: Wave theory applicability, [15]

3.4. Loads on fixed structures

The loads on a fixed structure can be divided in static and dynamic loads [4]. Static loads on a structure are due to gravity, hydrostatic loads and current loads. Dynamic loads are due to environmental loading such as wind and waves. The loads on a structure can be identified by the following parameters

$$\frac{F}{\rho U^2 D} = \phi\left(\frac{t}{T}, \frac{UT}{D}, \frac{UD}{\nu}, \frac{\pi D}{\lambda}, e, \frac{U}{f_n D}\right) \tag{3.25}$$

$$\text{Keulegan-Carpenter number } (KC) = \frac{UT}{D} \tag{3.26}$$

$$\text{Reynolds number } (Re) = \frac{\rho U D}{\mu} = \frac{UD}{\nu} \tag{3.27}$$

$$\text{Diffraction parameter} = \frac{\pi D}{\lambda} \tag{3.28}$$

$$\text{Relative roughness } (e) = \frac{K_r}{D} \tag{3.29}$$

$$\text{Reduced velocity} = \frac{U}{f_n D} \tag{3.30}$$

$$\text{frequency parameter } (\beta) = \frac{Re}{KC} = \frac{D^2}{T\nu} \tag{3.31}$$

(3.32)

The Keulegan Carpenter number is a measure of the relative contribution of the inertia and the drag loads, where U is the water velocity amplitude and T is the water velocity period. The Reynolds number is a measure of the inertia to the viscous forces. The diffraction parameter, is sometimes referred to as the dimensionless wave number KR, or Ka, where R, or a, represent the radius of the structure. The diffraction parameter is for deep water waves, equal to the squared Froude number, $Fr = \frac{u}{gL} = \omega\sqrt{\frac{R}{g}} = \sqrt{KR}$. The deep water wave number K is defined as

$$K = \begin{cases} \frac{\omega^2}{g} = \frac{2\pi}{\lambda} \\ k \tanh kd \end{cases} \tag{3.33}$$

The relative roughness, e, is a measure of the surface roughness to the diameter of the structure. The reduced velocity is similar in form to the KC number, and represents a measure of the cross-flow vibration of the structure in steady flow. The frequency parameter is a measure between Re and KC number helps group the drag coefficient, C_d and mass coefficient, C_m, [37]. Figure 3.3 shows which loads dominate the structure. Following [4], For region I, when $H/D < 0.25$ and $\pi D/\lambda < 0.5$, the drag terms are negligible, and inertia dominates the loads. The inertia part of the Morison equation should suffice for the wave calculation. When $\pi D/\lambda > 0.5$, a diffraction analysis should be included. For $H/D > 2$, in regions II, V, VI, the Morison equation should be used for the force computation on a submerged structural member.

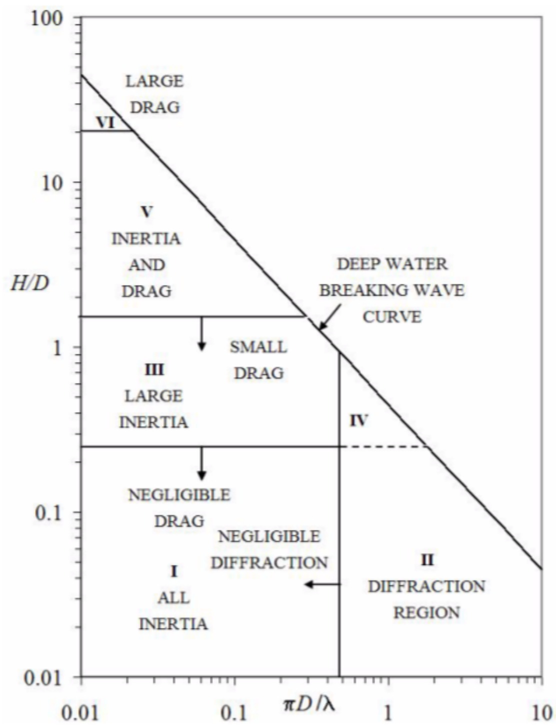

Figure 3.3: Limits of application [4], [1]

3.4.1. Equations of motion

When the system is allowed to respond to the wave excitation, the equation of motion for $i = 1, 2, ...6$ (surge, sway, heave, roll, pitch, yaw) can be written as:

$$\sum_{j=1}^{6} (m_{ij} + a_{ij})\ddot{\xi}_i + b_{ij}\dot{\xi}_i + c_{ij}\xi_i = F_i \cos(\omega t + \beta_i) \tag{3.34}$$

m_{ij} is the mass or mass moment of inertia, a_{ij}, the added mass, b_{ij} represents the wave-making damping, c_{ij} the restoring constants, F_i the wave-exciting force or moment, ω, the wave frequency and β_i the phase angle with respect to the wave motion above the centre of mass of the body.

Equation 3.34 can be separated into the hydrodynamic forces, $\sum_{j=1}^{6}(m_{ij}+a_{ij})\ddot{\xi}_i + b_{ij}\dot{\xi}_i$ and the hydrostatic forces, $\sum_{j=1}^{6} c_{ij}\xi_i$, [26] [19] [18].
The added mass and damping can be nondimensionalised, resulting in the hydrodynamic coefficients. Using the submerged volume, V, and the water density, ρ, the added mass coefficient, C_a , can be written as

$$C_a = \frac{a}{\rho V} = \frac{m_a}{\rho V} \tag{3.35}$$

The hydrodynamic coefficients can be determined experimentally. The damping is in phase with the velocity and the added mass and the spring constant are in phase with the displacement and acceleration, see Equation 3.34. Using this, the coefficients can be determined by subjecting the system to a decay test or a forced oscillation, see also A.1.1.

3.4.2. Determining hydrodynamic coefficients with potential flow

The hydrodynamic forces on a rolling ship on a free surface under the influence of incoming waves can be determined with potential theory under the following assumptions:

- Ideal fluid (incompressible, inviscid and irrotational)
- Relative wave amplitudes are small
- Oscillations of the hull are small

The velocity potential can now be represented as:

$$\phi(x,y,z,t) = \phi_1(x,y,z) + \phi_2(x,y,z,t) + \phi_3(x,y,z,t) + \phi_4(x,y,z,t) \tag{3.36}$$

ϕ_1 is the potential corresponding to stationary movement of the ship, with constant linear and angular velocities on a still free surface, ϕ_2 is the Froude-Kriloff potential or incoming wave potential, ϕ_3 represents the diffraction potential, ϕ_4 represents the radiation potential or potential of the forced oscillations.
In the computation of the added mass of a rolling ship, ϕ_1 is neglected, only the frequency of incoming waves are taken into account,[23] [7] [18].

3.5. Fixed structure in waves

3.5.1. Morison Equation

The loads on a structure in waves can be estimated with an empirical equation, the Morison equation. This relation was initially defined for a slender submerged cylinder or pile, but can be applied to other structures when the wavelength is much larger than the size of the structure [1], [20].

$$\lambda > 5 \cdot D$$

The Morison equation for a constrained vertical submerged cylinder defines the force per length, f, as

$$f(t) = \frac{\pi}{4}\rho C_m D^2 \cdot \dot{u}(t) + \frac{1}{2}\rho C_d D \cdot u|u| \tag{3.37}$$

C_m the non-dimensional mass or inertia, coefficient, which is defined as, $C_m = 1 + C_a$ [18]. u is the free stream velocity,
Following [20], the force per unit length in the direction of the flow, on a 2D object is assumed to consist of three parts:

$$f = A_0\rho\frac{d(ku)}{dt} + \oint p_x dS + \frac{1}{2}C_d D\rho u|u| \tag{3.38}$$

The first term is the added mass contribution or the diffraction force, k is a virtual mass coefficient and area $A_0 = \pi D^2/4$. Next is the Froude-Kriloff force or load due to the ambient pressure along the wave direction, p_y, integrated over dS, an element of the surface area. The last term describes the load due to drag. If the dimensions of the virtual term are compared with the load of the ambient pressure, with $A = rA_0$, where r represents the area ratio, the following holds

$$\oint p_y dS = \rho r A_0 \frac{du}{dt}$$
$$f = A_0 \rho \left[\frac{d(ku)}{dt} + r\frac{du}{dt} \right] + \frac{1}{2} C_d D \rho u|u| \tag{3.39}$$

as k is not dependent on time, it can be written as

$$\frac{d}{dt}(ku) = k' \frac{du}{dt} \tag{3.40}$$

and C_m can be defined as

$$C_m = (k' + r) \tag{3.41}$$

resulting in the Morison equation:

$$F = F_{inertia} + F_{drag}$$
$$f = C_m \rho A_0 \frac{du}{dt} + \frac{1}{2} C_d D \rho u|u| \tag{3.42}$$

Or, assuming the velocity is constant over the depth of the barrier, Equation 3.42 can be integrated of the depth for the whole structure, resulting in, [18], [20],[24],

$$F(t) = \rho C_m V \dot{v}(t) + \frac{1}{2} \rho C_d A u(t)|u(t)| \tag{3.43}$$

3.5.2. Determining the hydrodynamic coefficients

The hydrodynamic coefficients can be determined with different methods, a two approaches will be presented here

Fourier averaging method

The coefficients can be de determined using a Fourier series. The loads are assumed to vary harmonically, and can be written as a Fourier series. The average hydrodynamic coefficients can be approximated relatively well using on the first Fourier coefficients. For more information, see Appendix A.

Least Squares Method

The average hydrodynamic coefficients can also be found with the least squares method. With this method the squared difference between the assumed solution $f(x_i, a_1, a_2, ..a_n)$ and the force is minimized,

$$S \equiv \sum [y - f(t, a_1, a_2, ..a_n)]^2 \tag{3.44}$$

If applied to Equation 3.37 this would result in

$$f(t_i, C_m, C_d) = \frac{\pi}{4} \rho C_m D^2 \cdot \dot{u}(t_i) + \frac{1}{2} \rho C_d D \cdot u(t_i)|u(t_i)|$$
$$R^2 \equiv \sum [y_i - f(t_i, C_m, C_d)]^2$$

All data points in the time series have equal influence on the C_m and C_d coefficients [48].

3.6. Moving structure in still water

The sectional force on a moving slender structure in still water is defined as

$$f(t) = -\rho(C_m - 1) A \ddot{r}(t) - \frac{1}{2} \rho C_d D \dot{r}(t)|\dot{r}(t)| \tag{3.45}$$
$$\tag{3.46}$$

where $\dot{r}(t)$ represents the velocity of the structure. Assuming the velocity is constant over the depth of the barrier, Equation 3.45 can be written for the whole structure as

$$F(t) = -\rho(C_m - 1) V \ddot{r}(t) - \frac{1}{2} \rho C_d A \dot{r}(t)|\dot{r}(t)| \tag{3.47}$$

Here C_d represents the hydrodynamic damping.

3.7. Moving structure in waves

Combining Equation 3.45 with 3.42, the sectional force on a moving slender cylinder in non-uniform flow normal to the axis is defined as

$$f(t) = -\rho(C_m - 1)A\ddot{r}(t) + \rho C_m A\dot{v}(t) + \frac{1}{2}\rho C_d D v_r(t)|v_r(t)| \tag{3.48}$$

$$v_r(t) = v(t) - \dot{r}(t) \tag{3.49}$$

This is formulation is also known as the relative velocity formulation, [1]. Assuming the velocity is constant over the depth of the barrier, Equation 3.48 can be written for the whole structure as:

$$F(t) = -\rho(C_m - 1)V\ddot{r}(t) + \rho C_m V\dot{v}(t) + \frac{1}{2}\rho C_d A v_r(t)|v_r(t)| \tag{3.50}$$

Vertical loads

The Morison equation only accounts for the loads due to wave and current on a submerged structure. To apply the Morison equation to a structure in the free surface, the equation has to be modified. By including the body forces, the total load in the vertical direction for a system which is free to float can be written as

$$\begin{aligned} F_z(t) = & -\rho(C_m - 1)V\ddot{r}(t) + \rho C_m V\dot{v}(t) + \frac{1}{2}\rho C_d A_h v_r(t)|v_r(t)| \\ & + \rho \cdot V(t) \cdot 9.81 \end{aligned} \tag{3.51}$$

$V(t)$, the total submerged volume, consists of a static component, V_0, which for a free floating system, in still water, should confirm to $\rho V_0 \cdot 9.81 = \rho \overline{V} \cdot 9.81 = m \cdot 9.81$, and a dynamic component, $(V(t) - V_0)$, [6]

Horizontal loads

The water level on the left and the right side of the system can differ. This difference in submergence on the left and the right side of the barrier, will result in a load. The difference is denoted as dh, which multiplied with projected area of the high water level side of the barrier, A_{s_h}. If the barrier is free to move, this load should equal to the spring force.

$$\rho \cdot 9.81 \cdot \Delta h \cdot A_{s_h} = F_s = k \cdot (y(t) - y_0 - y_{\text{offset}}) \tag{3.52}$$

The spring force consists of the difference between the instantaneous location, the starting location and the pretension. The total load formulation in the horizontal direction depends on whether the system is constrained, or free to move in the sway direction.

$$\begin{aligned} F_y(t) = & -\rho(C_m - 1)V\ddot{r}(t) + \rho C_m V\dot{v}(t) + \frac{1}{2}\rho C_d A_s v_r(t)|v_r(t)| \\ & + k \cdot (y(t) - y_0 - y_{\text{offset}}) \end{aligned} \tag{3.53}$$

$$\begin{aligned} F_y(t) = & -\rho(C_m - 1)V\ddot{r}(t) + \rho C_m V\dot{v}(t) + \frac{1}{2}\rho C_d A_s v_r(t)|v_r(t)| \\ & + \rho \cdot 9.81 \cdot \Delta h \cdot A_s \end{aligned} \tag{3.54}$$

3.7.1. Independent flow form of the Morison equation

For the case of low frequency oscillation body in a high frequency flow, or vice versa, the relative velocity equation might not be applicable [49], [1]. For an oscillating cylinder in waves, the following formulation was proposed by Layla [25]:

$$\begin{aligned} f_y = & \rho \frac{\pi}{4} D^2 C_m^w \frac{du_w}{dt} + \frac{1}{2}\rho D C_d^w u_w|u_w| \\ & - \rho \frac{\pi}{4} D^2 C_a^b \frac{d\dot{y}}{dt} - \frac{1}{2}\rho D C_d^b \dot{y}|\dot{y}| \end{aligned} \tag{3.55}$$

Here u_w represents the wave velocity, and $\dot{y}$ represents the body velocity.

$C_d^w,\ C_m^w = f\left(\frac{U_w D}{\nu}, \frac{U_w T_w}{D}\right),\ C_d^b,\ C_a^b = f\left(\frac{U_b D}{\nu}, \frac{U_b T_b}{D}\right)$, [1]

3.8. Cm and Cd

The C_m and C_d coefficients vary with KC and Re. The coefficients are also related to the surroundings of the object. The hydrodynamic coefficients of an object placed in an infinite fluid will be different from an object close to the free surface. The values between 2D and 3D coefficients differ as well, but only 2D coefficients will be discussed here, [26] [19] [18].

3.8.1. In an infinite fluid

Sarpkaya, [38] performed experiments in a u-tube, a vertical water tunnel in which the flow oscillates, to determine the mass and drag coefficients of completely submerged shapes. In Figure 3.4a, C_m is plotted against the KC, for constant β and Re. In these experiments the C_m coefficient drops below 1, for $8 > \mathrm{KC} < 30$, which means that $C_a < 0$, as $C_m = C_a + 1$. $8 > \mathrm{KC} < 30$ is the transition region from the inertia dominated to the drag dominated regime. A negative added mass coefficient means the fluid force has the same sign as the acceleration of the cylinder, [36] [43], [30]. The mass and drag coefficients are equal in sway and heave $C_{m_y} = C_{m_z}$, $C_{d_y} = C_{d_z}$, [23] [13].

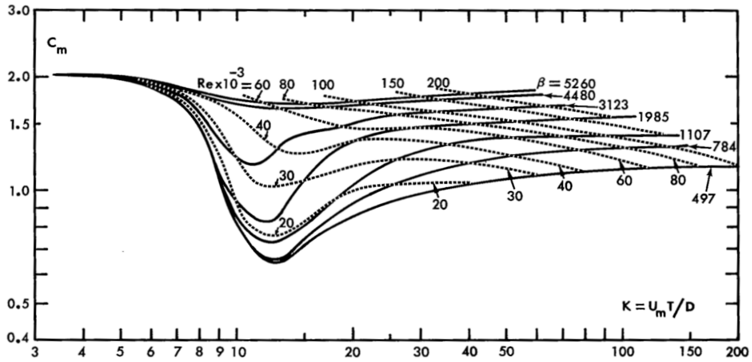

(a) Mass coefficient, C_m versus KC, for a cylinder in a u-tube [38]

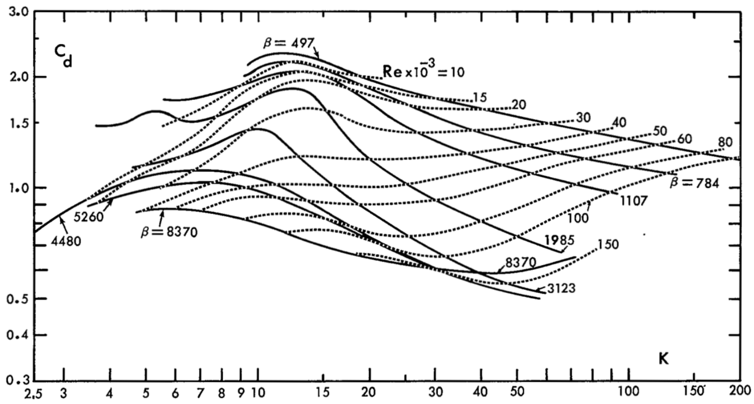

(b) Drag coefficient, C_d versus KC, for a cylinder in a u-tube [38]

Figure 3.4: Hydrodynamic coefficients, determined by Sarpkaya in a u-tube

3.8.2. Near a boundary

The added mass is dependent on the distance to a boundary or free surface. This is illustrated in Figure 3.5, for H/R, at a KR= 0.25, the added mass peaks to $C_a \approx 4.6$, while at KR= 0.5 it reaches a minimum, with $C_a \approx -1$. The added mass in Figure 3.5 was determined with potential flow by [13], [31].

3.8.3. Surface piercing

As the body is in the free surface, the coefficients for added mass in heave and sway are no longer equivalent, as can be seen in Figure 3.6. The peaks found in the added mass near and on a boundary disappear as the circular cylinder is less submerged. Greenhow, [13], also determined the damping coefficients for a cylinder

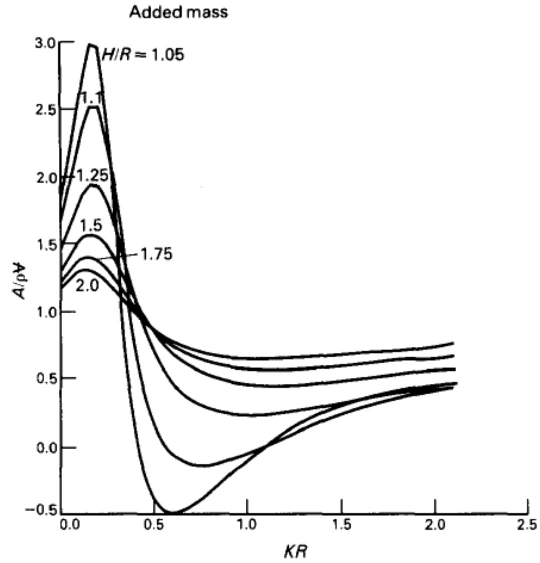

(a) C_a [13]

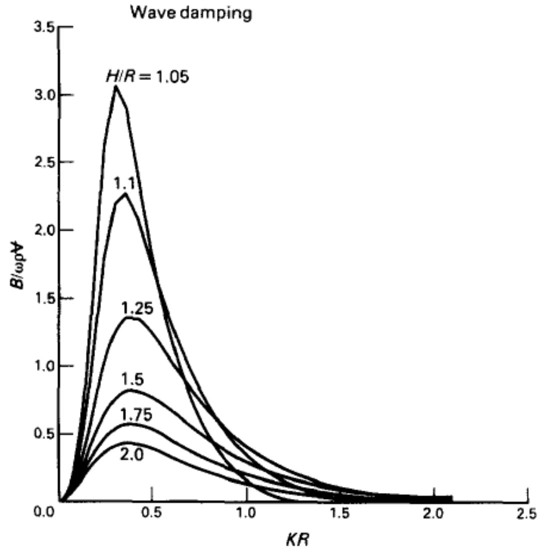

(b) C_d [13]

Figure 3.5: C_a and C_d close to a free surface

on the surface. However, his results for a heaving cylinder do not seem to match the experiments performed by Vugts, see Figure 3.7, note the different scales, KR and $\sqrt{KR}$. Vugts also tested rectangular cylinders with different breadth to draft ratios. In heave he tested different amplitudes. In Figure 3.7d the influence of the heave amplitude is more visible than in Figure 3.7b. Both figures show that the amplitude has influence on the hydrodynamic coefficients, but it's effect is small.

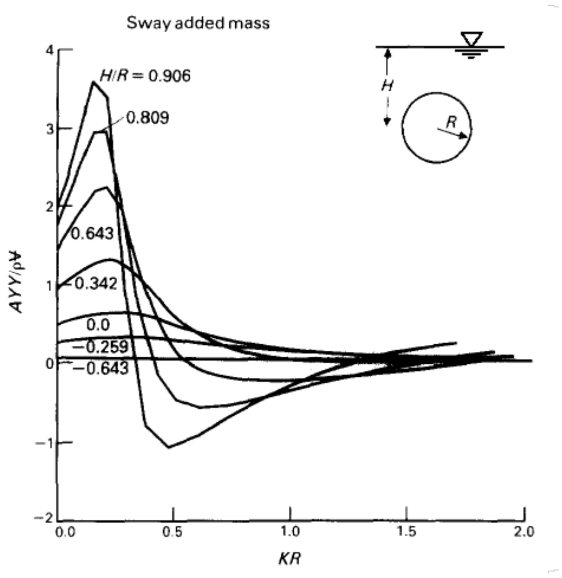

(a) C_a in sway [13]

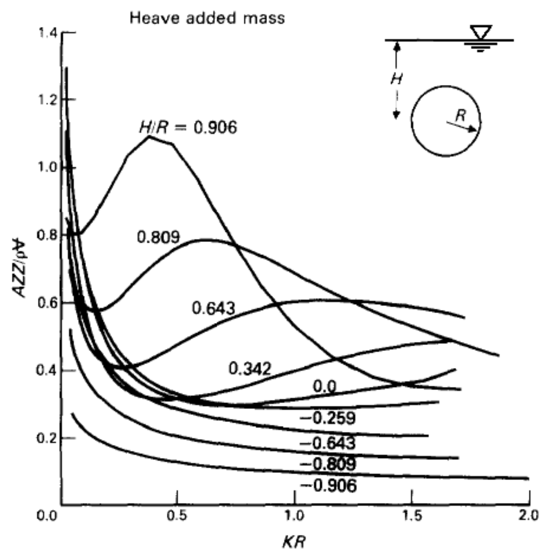

(b) C_a in heave [13]

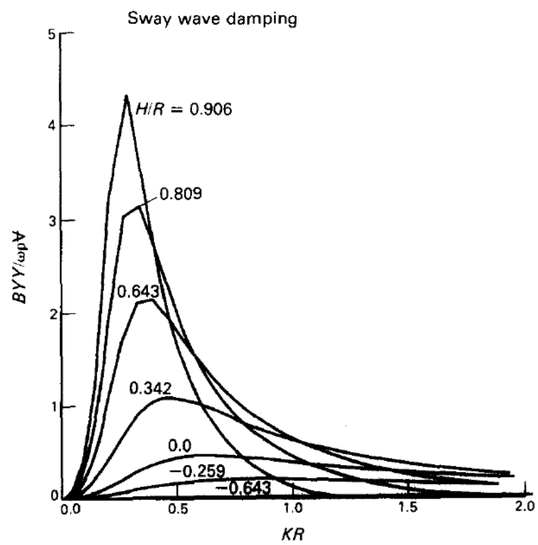

(c) C_d in sway [13]

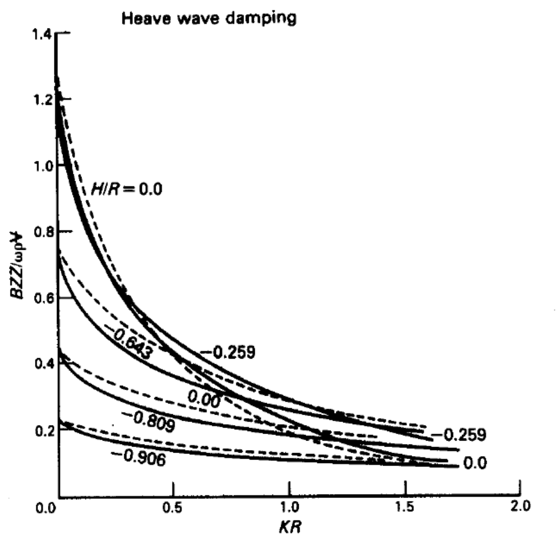

(d) C_d in heave, less than half submerged [13]

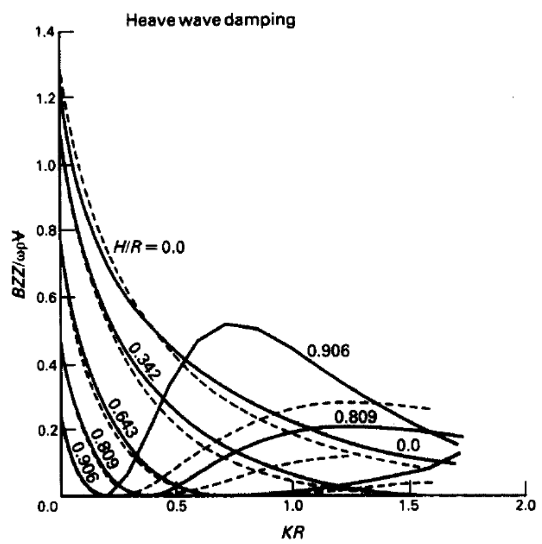

(e) C_d in heave, more than half submerged[13]

Figure 3.6: Added mass and damping coefficients versus KR, for a surface piercing cylinder, when $H/r < 0$ the cylinder is less than half submerged [13]

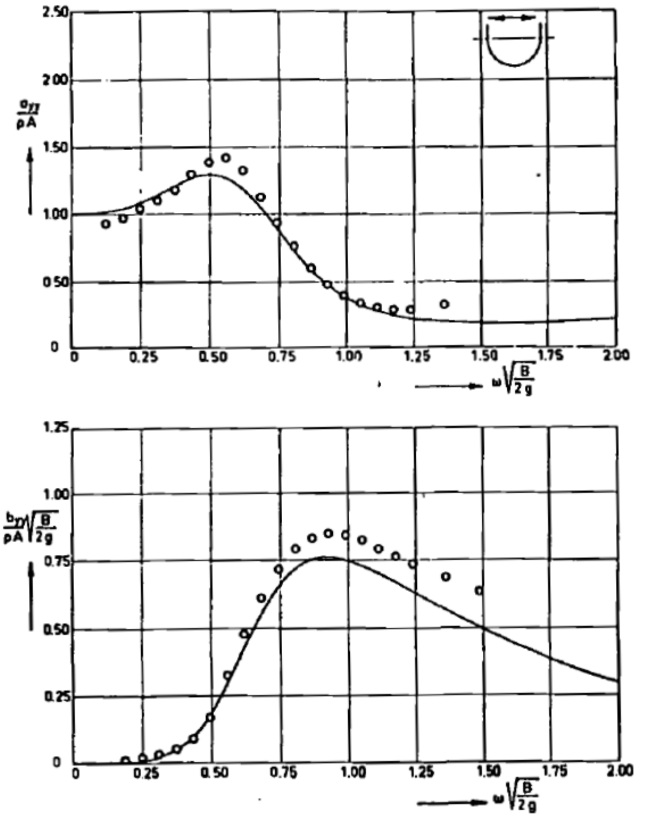

(a) C_a and C_d in sway for a half submerged cylinder, versus $\sqrt{KR}$ [45]

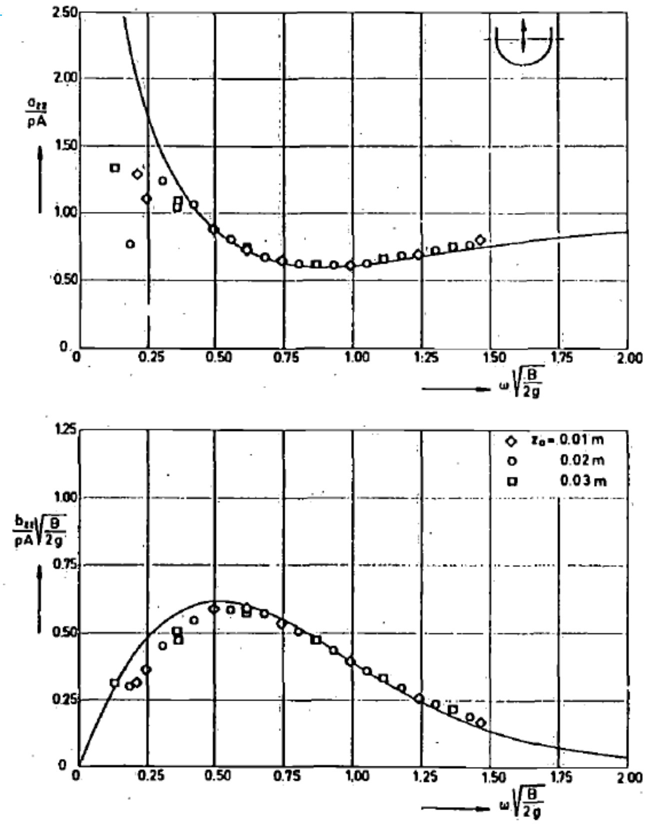

(b) C_a and C_d in heave for a half submerged cylinder, for different amplitudes, versus $\sqrt{KR}$ [45]

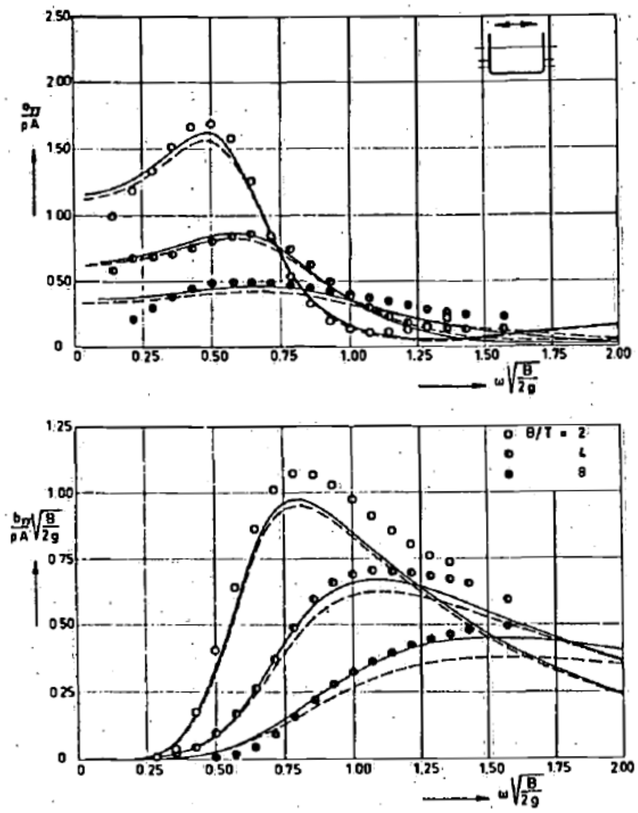

(c) C_a and C_d in sway for a half submerged rectangle, for different ratios of breadth to draft, versus $\sqrt{KR}$ [45]

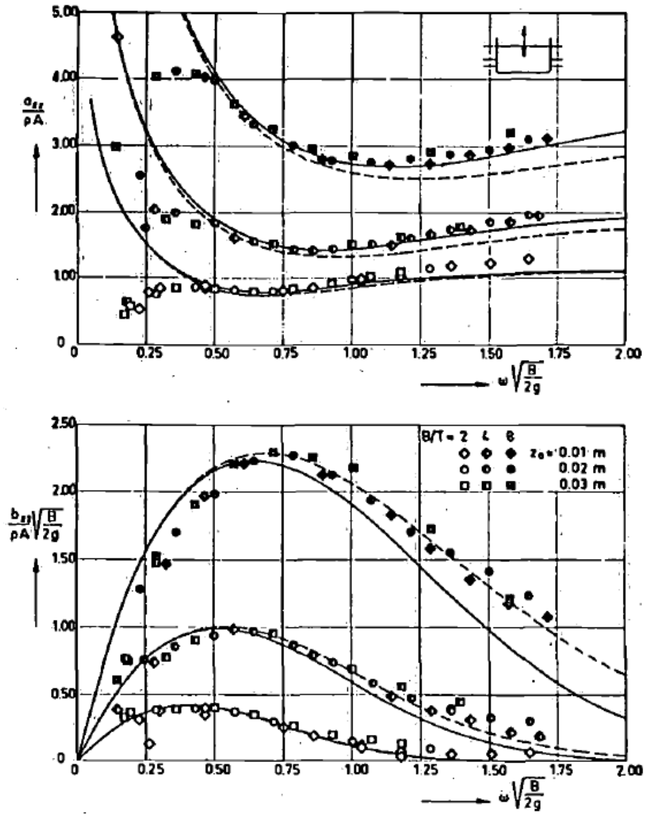

(d) C_a and C_d in sway for a half submerged rectangle, for different ratios of breadth to draft, and amplitudes, versus $\sqrt{KR}$ [45]

Figure 3.7: Added mass and damping calculations, the points represent experiments by Vugts, the line represent theoretical results [45]

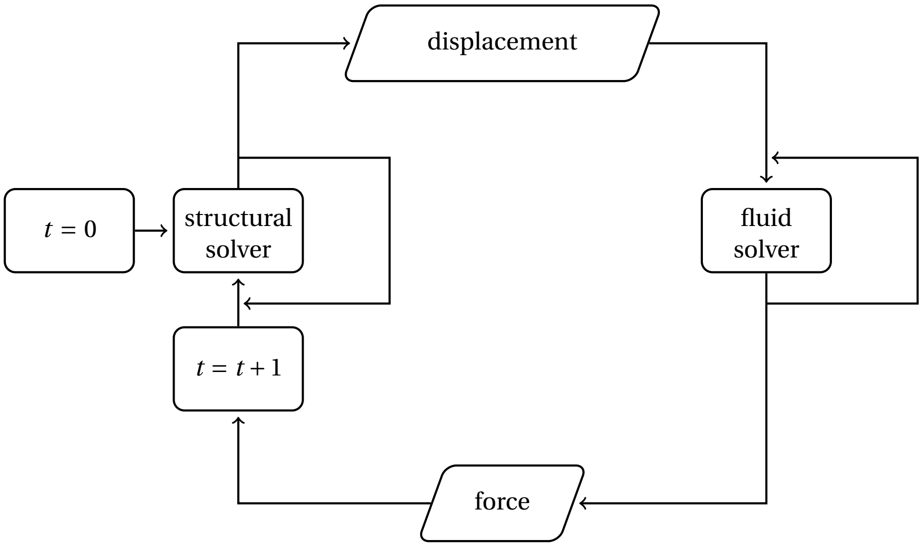

Figure 3.8: One way fluid-structure interaction

3.9. Fluid-structure interaction

Most models handle one kind of physics. A simulation on the stresses in a propeller blade could be performed by imposing a distributed lift and drag force on a blade. The blade will deform due to the load and the pressure distribution will change. An aerodynamic model will only incorporate the obstruction of the flow due to the blade, but will neglect the structural deformation of the blade. Solving both the structural deformation and the flow field can be done with two different approaches, the monolithic approach and the partitioned approach.

In the monolithic approach, the fluid and structural system are solved simultaneously within one solver. Because the systems are solved within a single set of equations, the system can be fully coupled.

In the partitioned approach the fluid and structural domain are solved each in their respective solver. The setup of the system determines to what extent the problem is coupled.

3.10. One way coupled fluid-structure interaction

In one way coupled fluid-structure interaction, the output of the structural solver is fed to the fluid solver. The fluid solver iterates until convergence criteria are met. The result is fed to the structural solver. This is visualised in Figure 3.8.

3.11. Two way coupled fluid-structure interaction

In two way coupled interaction, the solvers individually have to reach convergence, and their shared results, have to reach an equilibrium. Only when an equilibrium is reached, the solvers can move on to the next time step. The amount of iterations till the shared result has converged and the convergence criteria determine the strength of the coupling system.

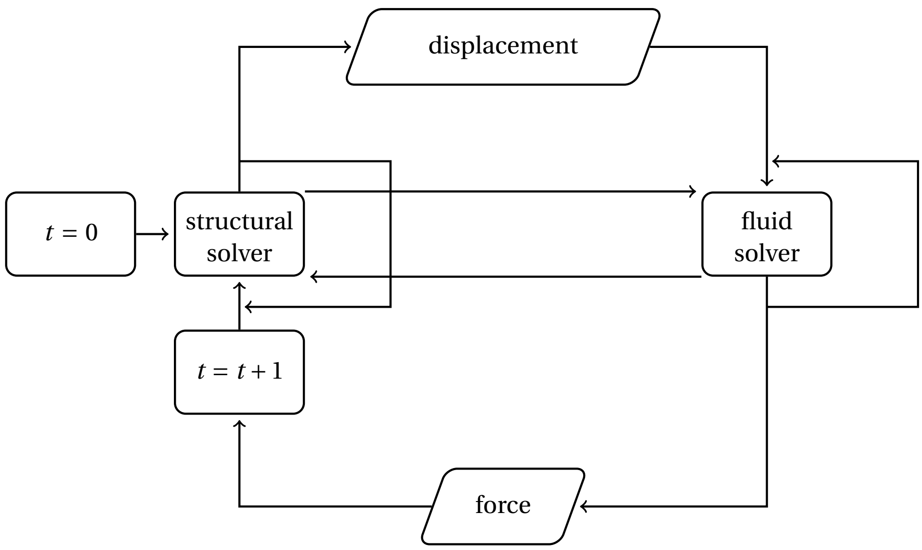

Figure 3.9: Two way fluid-structure interaction

4
Setup

4.1. Models used and tried

Initially, the objective of this thesis was to model the fully coupled fluid-structure interaction semi-2D with a flexible body. This resulted in multiple, hard-to-pinpoint problems with instabilities, for both an elastic case and a rigid case. The troubles could be attributed to the fluid solver, the structural solver or the coupling, or a combination of these.
Lastly, a rigid 2D, coupled system using only a fluid solver was tried, which proved to be more successful. The fluid solver solves the flow and the equations of motion of the rigid body, resulting in a two way coupled fluid body interaction. This rigid 2D system will be discussed in here.

In hindsight, it would have been a better approach to set up a 2D system first. This system could have been expanded to a rigid semi-2D system, which in turn could have been expanded to a fully coupled flexible system.

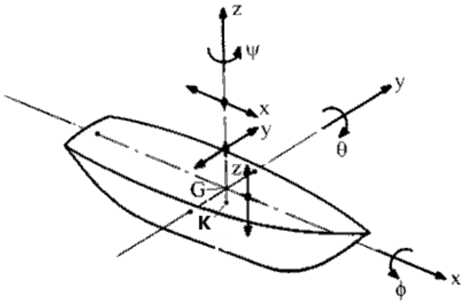

hb

Figure 4.1: Ship axis convention [29]

4.1.1. Scaling laws

Froude law was used to keep similarity in forces, see also E.16

$$Fr = \frac{V}{\sqrt{g \cdot L}} = \frac{\alpha_v}{\alpha_g \cdot \alpha_L}$$

As the gravity will not be scaled $\alpha_g = 1$, $\alpha_v = \alpha_L / \alpha_T$, thus $\alpha_T = \sqrt{\alpha_L}$

Table 4.1: Scaling laws, using Froude [18]

Symbol	Scale factor	Relationship
Length	α_L	$L_f = \alpha_L \cdot L_m$
Time	α_T	$T_f = \sqrt{\alpha_L} \cdot T_m$
Velocity	α_V	$V_f = \sqrt{\alpha_L} \cdot V_m$
Gravity	α_g	$g_f = \alpha_g \cdot g_m$
Density	α_ρ	$\rho_f = \alpha_\rho \cdot \rho_m$
Viscosity	α_μ	$\mu_f = \alpha_\mu \cdot \mu_m$
Area	α_S	$A_f = \alpha_L^2 \cdot A_m$
Volume	α_∇	$\nabla_f = \alpha_L^3 \cdot \nabla_m$
Inertia	α_I	$I_f = \alpha_\rho \cdot \alpha_L^5 \cdot I_m$
Mass	α_M	$M_f = \alpha_\rho \cdot \alpha_L^3 \cdot M_m$
Force	α_F	$F_f = \alpha_\rho \cdot \alpha_L^3 \cdot F_m$
Spring stiffness	α_k	$k_f = \alpha_\rho \cdot \alpha_L^2 \cdot k_m$

4.1.2. Coordinate system

In maritime engineering a ship moves along its axis, surge, and orthogonal in plane to this axis is called sway, see Figure 4.1. The Ocean Cleanup barrier has an unusual shape, unlike a ship, it moves orthogonal to its axis. The Ocean Cleanup calls this direction surge. To simplify the comparison to literature, in this thesis, the barrier moves is sway. Figure 4.1 and Figure 4.2a show the axis convention.

4.2. MARIN 2016 test

In the tests performed at MARIN, two barriers were tested, for two mooring configurations. The tested barriers were a flexible barrier made by DESMI and a rigid barrier made by MARIN.
Only the rigid barrier will be discussed in this report, as the flexible barrier shows no similarity to either the rigid body barrier from MARIN or the Deltares flexible barrier.

The experiment consisted of irregular wave tests, regular wave tests, current tests and tests to investigate the plastic capture efficiency of the system. End plates were used to lessen 3D effects, still 3D effects were observed. The plastic capture efficiency test helped visualise the different flow pattern along the width of the barrier. This has been described in more detail in [5].
The regular waves had wave lengths (on model scale) of $\lambda = 10.89$ $[m]$, $T = 2.68$ $[s]$ to $\lambda = 17.27$ $[m]$, $T =$

3.58 $[s]$ and wave heights $H = 0.15$ $[m]$ to $H = 0.36$ $[m]$. These were all second order stokes waves.
To simplify the numerical model, a lower wave height was chosen for the simulation, such that it falls in the airy wave regime, see Table 4.2. An overview of the original values can be found in **??**. The current-only tests were performed with velocities between $v = 0.05$ $[m/s]$ and $v = 0.224$ $[m/s]$.

Table 4.2: Modelled waves

				Unit
Wave length, λ	14.329	17.27	20.427	$[m]$
Wave period, T	3.17	3.577	4.08	$[s]$
		0.084		$[m]$
Wave height, H	0.1	0.1	0.1	$[m]$
		0.12		$[m]$

Table 4.3: Chosen model scale and the numerical model test setup

	MARIN model, 3D	Symbol	Numerical model, 2D	Unit
Tank length	220		$6 \cdot \lambda$	$[m]$
Tank width	4		–	$[m]$
Tank depth	3.6	d	3.6	
Spring stiffness	1447	k_s	289.46	$[N/m]$
Barrier width	2.62		-	$[m]$
Boom diameter	0.2	D	0.2	$[m]$
Skirt length	0.275	l_{sk}	0.275	$[m]$
Skirt thickness	0.0055	t_s	0.0055	$[m]$
Ballast diameter	0.025	D_b	0.025	$[m]$
Moment of inertia per meter	0.17	I_{xx}	0.17	$[kg/m^2]$
Centre of gravity relative to the bottom of the system	0.18	cg_{z_s}	0.18	$[m]$
Centre of gravity relative to the bottom of the tank		cg_{z_o}	0.3446	$[m]$
dynamic viscosity	$1.308 \cdot 10^{-3}$	μ	$1.308 \cdot 10^{-3}$	$[kg \cdot s/m]$
water density	998.2	ρ	998.2	$[kg/m^3]$
Reynolds number		$Re = \frac{uD\rho}{\mu}$	$(1.25 - 1.9) \cdot 10^4$	[-]
Keuler-Carpenter number		$KC = \frac{uT}{D}$	$(1.2 - 1.9)$	[-]
KR number		$KR = k \tanh kd \cdot \frac{D}{2}$	$0.01 - 0.05$	[-]
pretension		y_{offset}	0.002	$[m]$

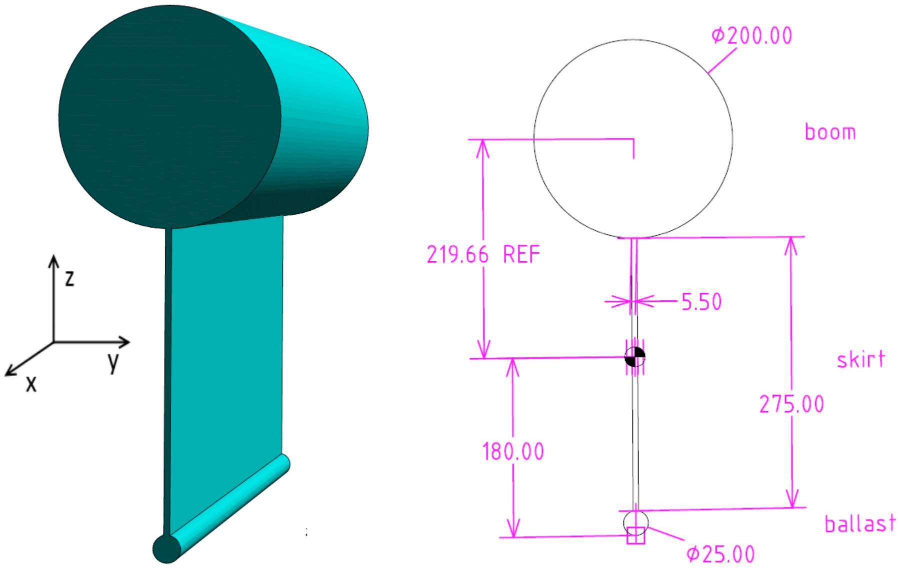

(a) 3D view of the model.

(b) Dimensions of the barrier in mm

Figure 4.2: Overview of the model

4.3. Numerical model

The barrier is modelled in a two dimensional numerical wave tank. The governing equations, the incompressible inviscid Navier-Stokes equations, or Euler equations, are solved with a pressure-based solver with ANSYS Fluent. The multiphase flow is solved by means of a Volume of Fluid method. The PISO-scheme was used for the pressure-velocity coupling. The temporal discretisation was 1st order implicit as this proved to be more stable than the 2nd order implicit scheme.

4.3.1. Domain

A schematic overview of the domain is given in 4.3b. The different patterns denote refinement regions. Two setups were used. The first setup, a numerical wave tank, was used to determine the undisturbed velocity and acceleration in the Morison equation. The second setup consisted of a numerical wave tank with a barrier, to determine the loads on the barrier. The meshes were generated using ANSYS Meshing. The cell size can be found in Table 4.4 and Table 4.5.

Numerical wave tank

The domain has a size of $(6\cdot\lambda)x(d\cdot 1.5+H/2)$. The test section is at $2\cdot\lambda$ from the inlet. Close to the free surface, the cells are more refined. The height of the free surface region is H. Above and below the free surface are transition regions, denoted as "transition a" and "transition w". In these regions the mesh changes from a refined mesh, to a more coarse mesh (along the z axis). Both the free surface region and the transition regions consist of quadrilateral cells. The regions denoted as air and water have a coarser mesh consisting of triangles. They gradually change from broader to coarse at the edge. Grid damping is used to dampen the reflection at the outlet. The cells stretch from fine to coarse over a distance $3\cdot\lambda$.

Numerical wave tank with barrier

The wave tank and the wave tank with barrier are as geometrically similar as possible. A schematic overview of the setup can be found in Figure 4.3. The barrier is placed in a box and within this box the barrier is free to move. The top of the box is placed $2\cdot H+2.5\cdot D$ from the water line, the bottom is placed at $2\cdot H+$ heigth of the barrier from the waterline. The left and the right side are at $5\cdot D$ from the centre of the barrier. The box is meshed with triangles and the resolution in the free surface was kept in line with the rest of the wave tank. On the left and right of the box, there is a small transition region with a width of $\lambda/3$. Within the transition region the mesh is spaced such that the cells close to the box are approximately square and that the transition to the triangles is smooth. An overview of the parameters can be found in Table 4.5. The barrier was meshed with a grid size of $5\cdot 10^{-3}$ $[m]$. This mesh size was chosen because it both conserves the shape

Table 4.4: Overview the discretisation of the domain

	region	dy	bias	dz	bias
computation zone					
	free surface	$\lambda/150$	–	$H/20$	–
	transition w	$\lambda/150$	–	$(3.5 \cdot H)/30$	5
	water	60	–	$(d-4 \cdot H)/6$	4
	transition a	$\lambda/150$	–	$(H \cdot 1.5)/10$	7
	air	60	–	$(0.5 \cdot d - 1.5 \cdot H)/4$	3
damping zone					
	free surface	$\lambda/150$	–	$H/20$	–
	transition w	22	27	6	4
	water	22	27	$(d-4 \cdot H)/2$	1.5
	transition a	22	27	$(H \cdot 1.5)/10$	7
	air	22	27	$(0.5 \cdot d - 1.5 \cdot H)/2$	1.5

of the barrier, the barrier is relatively round and the ballast resembles a circle and it helps enforce the free surface mesh resolution in the box. A close up of the box can be found in Figure D.1.

Table 4.5: Overview the discretisation of the domain with barrier, the discretisation in the other regions follows Table 4.4

	region	dy	bias	dz	bias
computation zone					
	transition box	$\lambda/3/70$	4	$H/20$	–
	box	25	–	6	–
		dl	unit	inflation	unit
	barrier	$5 \cdot 10^{-3}$	$[m]$	$5 \cdot 10^{-3}$	$[m]$

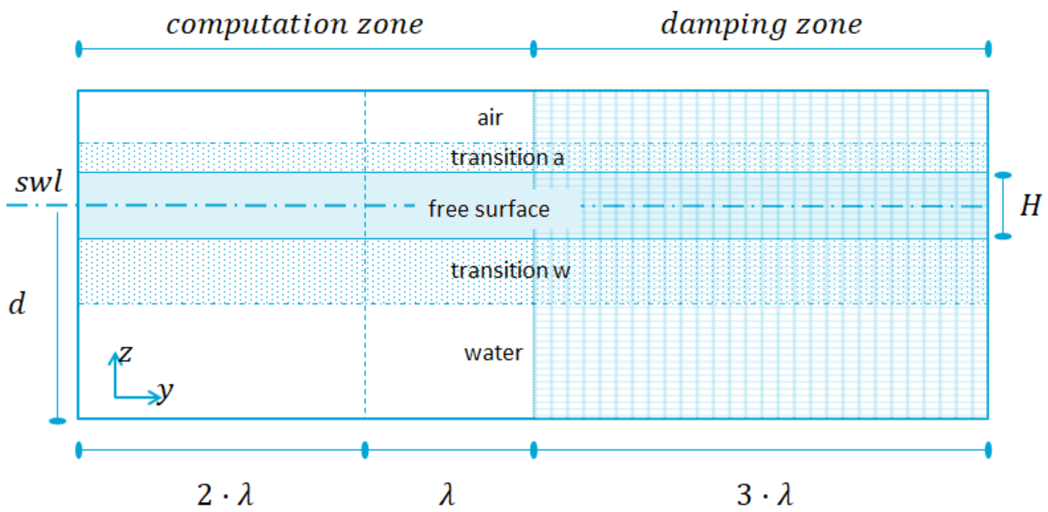

(a) Numerical wave tank

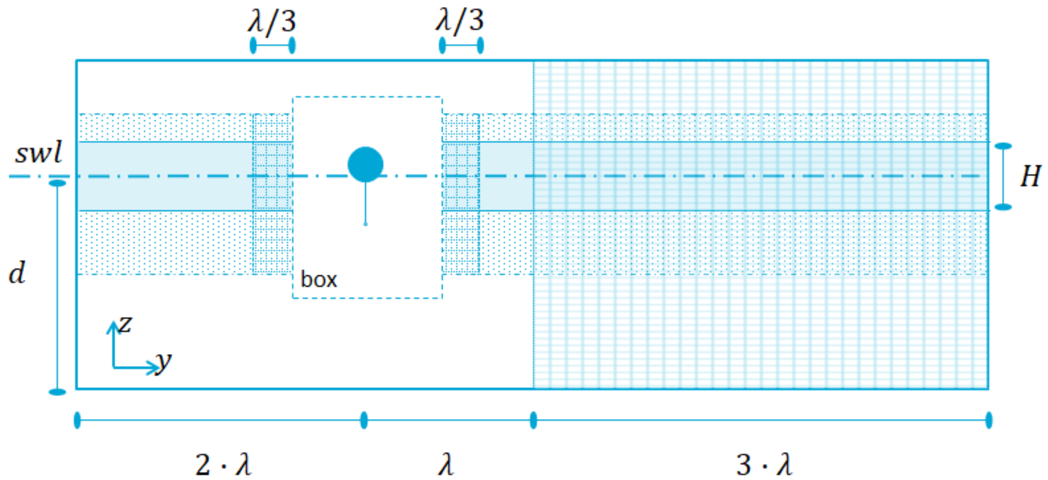

(b) Numerical wave tank with barrier

Figure 4.3: Schematic overview of the numerical wave tank

4.4. Test setup

Two cases have been modelled. The first case is a forced oscillation in still water. The second case is the system responding to an imposed wave. The direction of oscillation, or the degree of freedom of the system is varied for both cases.

4.4.1. Imposed motion, still water

The forced oscillation in still water is often used to determine the hydrodynamic coefficients. Two motion were tested, sway and heave.
In sway, a velocity bvy, is imposed on the system, with

$$\mathrm{bvy} = \frac{H}{2} \cdot \omega \cdot \cos(\omega \cdot t + 0.5 \arccos(-1)) \tag{4.1}$$

In heave a velocity bvz, is imposed on the system,
with

$$\mathrm{bvz} = \frac{H}{2} \cdot \omega \cdot \cos(\omega \cdot t + 0.5 \arccos(-1)) \tag{4.2}$$

The water is patched onto the domain. Every simulation is first allowed to stabilise for 20 time steps, before the forced oscillation is started.

Table 4.6: Boundary conditions for imposed motion, still water

Location	Boundary condition
Left side domain	Symmetry
Right side domain	Symmetry
Bottom domain	Symmetry
Top domain	Pressure outlet
Barrier	Wall

$$\tag{4.3}$$

4.4.2. Imposed waves

This test setup consists of a numerical wave tank for the model simulation and a numerical wave tank for the determination of the undisturbed velocity.
The wave is generated at the inlet with the Open Channel Wave Boundary condition, which imposes the following conditions at the inlet:

$$\eta(z,t) = A\cos(k_y y + k_z z - \omega t + \epsilon) \tag{4.4}$$

$$u_x(z,t) = \hat{u}_x \cos(\omega t - kx) \qquad \text{with } \hat{u}_x = \frac{gka}{\omega} \frac{\cosh[k(d+)]}{\cosh(kd)} \tag{4.5}$$

$$u_z(z,t) = \hat{u}_z \sin(\omega t - kx) \qquad \text{with } \hat{u}_z = \frac{gka}{\omega} \frac{\sinh[k(d+z)]}{\cosh(kd)} \tag{4.6}$$

The domain is initialised with a flat free surface. The simulation is first allowed to stabilise for 20 time steps, before the barrier is allowed to move.

Four cases were tested with waves imposed on the body. The first case, fixed, means the barrier has no degrees of freedom. A barrier free in heave constrained in sway (dof-z) was tested for the second case. The third case is a barrier constrained in heave, with a degree of freedom in sway (dof-y) kept in place by a spring force, F_s.

$$F_s = -ks \cdot (y - y0 - y_{\text{offset}})$$

Lastly, the case which resembles the behaviour of the floating object most, a barrier with 2 degrees of freedom, dof-yz. The Morison equation is defined for f, a force per meter. To simplify the calculations, the wave velocity in the horizontal direction is measured at the starting location of the system, halfway between the top of the wave and the bottom of the model, $[2 \cdot \lambda,\ d + (H/2 - \overline{A_s})]$. The wave velocity in the vertical direction were initially measured at $[2 \cdot \lambda,\ d - \overline{A_s}]$, [24]. The tests by Kristiansen [24] contained a rectangular cylinder

Table 4.7: Overview of the cases with imposed waves

	Freedom in		
	y, sway	z, heave	F_s
fixed	-	-	
dof-z	-	✔	-
dof-y	✔	-	✔
dof-yz	✔	✔	✔

in the free surface. He chose the bottom of the model as representative point. However, the barrier has a very small surface at the bottom, to say that the loads at the bottom are representative for the whole structure is perhaps too far fetched. Therefore $[2 \cdot \lambda,\ d - H/2]$ was chosen as the representative value.

The movement of the barrier is not taken into account when determining the wave velocity. This will induce an error, as the motion the system could have a small phase and magnitude difference. This error is not accounted for in the determination of the hydrodynamic coefficients these differences are neglected.

Table 4.8: Boundary conditions for imposed waves

Location	Boundary condition
Left side domain	inlet - Open Channel Wave Boundary
Right side domain	Outlet
Bottom domain	Symmetry
Top domain	Symmetry
Barrier	Wall

Rigid body dynamics in Fluent

ANSYS Fluent has a built in solver to solve the interaction between a solid body and a fluid. This six degree of freedom (DOF) solver calculates the hydrodynamic forces by integrating pressure over the surface in order to estimate the motion of a rigid object.

4.5. Post-processing

The output from the simulation are the loads, location, velocity and acceleration and the submerged area of the barrier. In order to determine the hydrodynamic coefficients, first the submerged volume and projected area need to be determined. The procedure can be found in Appendix B. After these values have been approximated, the hydrodynamic coefficients can be determined using the procedure described in Subsection 4.5.

Submerged volume and area

To give the reader some feeling about the magnitude and quantities of the numbers involved, Table 4.9 shows the mean submerged area and volume of the barrier.

Table 4.9: The average submerged volume and projected area and the total volume and projected area of the barrier

	Average	Total	Unit
Volume	0.0058	0.0334	$[m^3]$
Area$\perp_z$, $\overline{A_h}$	0.154	0.2	$[m^2]$
Area$\perp_y$, $\overline{A_s}$	0.336	0.5	$[m^2]$

Determining the hydrodynamic coefficients

The hydrodynamic coefficients of the modified relative velocity relation, Equation 3.51, 3.53 and 3.54 will be determined using the least squares method. As described in Section 3.7, 3.53 and 3.54 should lead to the same value. Equation 3.53 applies to cases free in sway, Equation 3.54 to cases constrained in y.

$$F_z(t) = -\rho(C_M - 1)V(t)\ddot{r}(t) + \rho C_M V(t)\dot{v}(t) + \frac{1}{2}\rho C_D A_h(t) v_r(t)|v_r(t)|$$
$$+\rho \cdot V(t) \cdot 9.81$$
$$F_y(t) = -\rho(C_M - 1)V(t)\ddot{r}(t) + \rho C_M V(t)\dot{v}(t) + \frac{1}{2}\rho C_D A_s(t) v_r(t)|v_r(t)|$$
$$+k \cdot (y(t) - y_0 - y_{\text{offset}})$$
$$F_y(t) = -\rho(C_M - 1)V(t)\ddot{r}(t) + \rho C_M V(t)\dot{v}(t) + \frac{1}{2}\rho C_D A_s(t) v_r(t)|v_r(t)|$$
$$+\rho \cdot 9.81 \cdot \Delta h(t) \cdot A_s(t)$$

The window of time for which the simulation is performed is determined as follows: The barrier is at $2 \cdot \lambda$ from the inlet, which means it takes 2 wave periods to arrive at the barrier. It takes roughly 3 periods to establish a stable wave. As the simulation progresses, the mesh quality deteriorates due to the deformations and waves reflecting from the barrier, inlet and outlet. These effects could influence the results. A window of $t = [6 \cdot T_p : 11 \cdot T_p]$ was chosen for the determination of the coefficients, to keep mesh deformations and other instabilities in check.

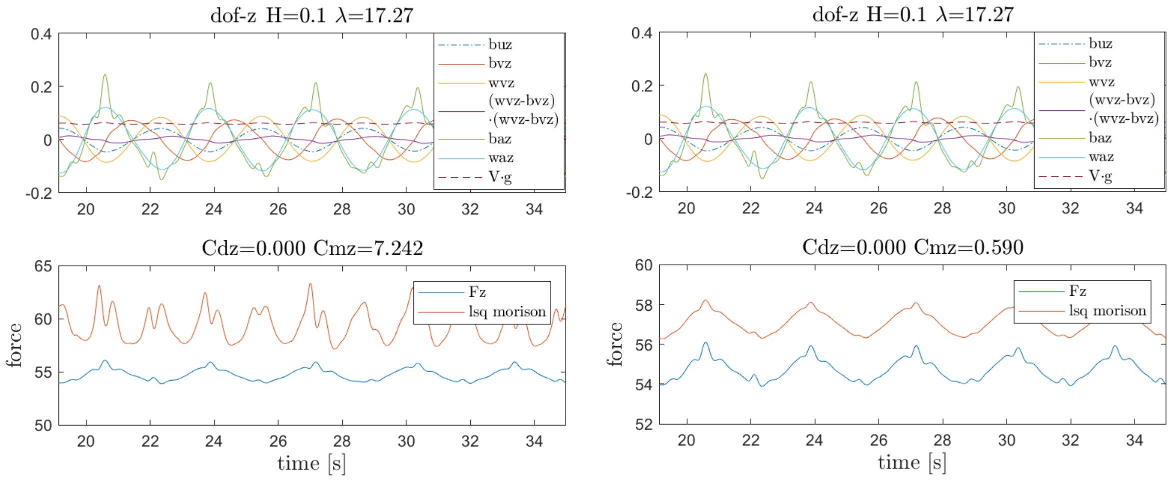

(a) 2 parameter fit, using $V(t)$

(b) 2 parameters fit, using $\overline{V}$

Figure 4.4: Hydrodynamic coefficients for a system free in heave, calculated with instantaneous and mean volume

In the formula for the varying vertical load, F_z, the use of the instantaneous volume for the varying buoyancy force, [6], does not seem to be the right approach in cases unconstrained in heave, namely dof-z and dof-yz. Figure 4.4a, shows the force F_z and the least squares fit. The shape of the body acceleration, baz, resembles the load Fz, but the approximation is dominated by the instantaneous volume. Replacing the instantaneous volume in Equation 3.51 with the mean still water volume, $\overline{V}$, leads to a better approximation of the loads on the system. This is shown in Figure 4.4b.
For dof-z and dof-yz the modified relative velocity equation becomes:

$$F_z(t) = -\rho(C_M - 1)V(t)\ddot{r}(t) + \rho C_M V(t)\dot{v}(t) + \frac{1}{2}\rho C_D A_h(t) v_r(t)|v_r(t)|$$
$$+\rho \cdot \overline{V} \cdot 9.81 \tag{4.7}$$

The mean of the approximation shows both in Figure 4.4b and 4.4a an offset with respect to the load. Upon inspection, it seems the geometry changed between design software, meshing software and the solver.
The difference in circumference is on the order of $(2-4) \cdot 10^{-4} m^3$, which on an prescribed volume of $0.0334 m^3$ is 0.6%. This volume difference results in a mass discrepancy of 5%, which explains the 5% discrepancy in the load.
The volume difference can be corrected for, if the system is free to move in heave. Then, difference can be quantified with $(\overline{V} \cdot \rho \cdot 9.81 - 9.81 \cdot \text{mass})$. In Equation 3.51, $\overline{V} \cdot \rho \cdot 9.81$ is replaced with $9.81 \cdot \rho \cdot \overline{V} - (\overline{V} \cdot \rho \cdot 9.81 - 9.81 \cdot \text{mass})$.

$$F_y(t) = -\rho(C_M - 1)V\ddot{r}(t) + \rho C_M V\dot{v}(t) + \frac{1}{2}\rho C_D A_h v_r(t)|v_r(t)| + \overline{V}\cdot\rho\cdot 9.81 - (\overline{V}\cdot\rho\cdot 9.81 - 9.81\cdot\text{mass}) \tag{4.8}$$

Lastly, the difference between the geometry in the solver and the prescribed volume can be accounted for by adding an extra parameter to create a better fit.

An overview of the different approaches used to find the hydrodynamic coefficients is given in the following sections.

The 2-parameter fit

Using 2 parameters, C_d and C_m, for Equation 3.51, 3.53 and 3.54 can be determined using:

$$R^2 \equiv \sum[y_i - f(t_i, C_m, C_d)]^2$$

$$\begin{aligned}
F_z(t) &= -\rho(C_M - 1)V\ddot{r}(t) + \rho C_M V\dot{v}(t) + \frac{1}{2}\rho C_D A_s v_r(t)|v_r(t)| \\
&\quad + \rho\cdot V(t)\cdot 9.81 \\
F_y(t) &= -\rho(C_M - 1)V\ddot{r}(t) + \rho C_M V\dot{v}(t) + \frac{1}{2}\rho C_D A_s v_r(t)|v_r(t)| \\
&\quad + k\cdot(y(t) - y_0 - y_{\text{offset}}) \\
F_y(t) &= -\rho(C_M - 1)V\ddot{r}(t) + \rho C_M V\dot{v}(t) + \frac{1}{2}\rho C_D v_r(t)|v_r(t)| \\
&\quad + \rho\cdot 9.81\cdot\Delta h\cdot A_{s_h}
\end{aligned}$$

The 2-parameter fit with volume correction

The hydrodynamic coefficients in heave, C_{m_z} and C_{d_z}, of the 2 parameter fit and the hydrodynamic coefficients of the 2 parameter fit with volume correction should be the same.

$$R^2 \equiv \sum[y_i - f(t_i, C_m, C_d)]^2$$

$$\begin{aligned}
F_z(t) &= -\rho(C_M - 1)V\ddot{r}(t) + \rho C_M V\dot{v}(t) + \frac{1}{2}\rho C_D A_h v_r(t)|v_r(t)| \\
&\quad + \rho\cdot V(t)\cdot 9.81 && (4.9) \\
F_z(t) &= -\rho(C_M - 1)V\ddot{r}(t) + \rho C_M V\dot{v}(t) + \frac{1}{2}\rho C_D A_h v_r(t)|v_r(t)| && (4.10) \\
&\quad + \overline{V}\cdot\rho\cdot 9.81 - (\overline{V}\cdot\rho\cdot 9.81 - 9.81\cdot\text{mass}) && (4.11) \\
F_y(t) &= -\rho(C_M - 1)V\ddot{r}(t) + \rho C_M V\dot{v}(t) + \frac{1}{2}\rho C_D A_s v_r(t)|v_r(t)| \\
&\quad + k\cdot(y(t) - y_0 - y_{\text{offset}}) && (4.12) \\
F_y(t) &= -\rho(C_M - 1)V\ddot{r}(t) + \rho C_M V\dot{v}(t) + \frac{1}{2}\rho C_D A_s v_r(t)|v_r(t)| \\
&\quad + \rho\cdot 9.81\cdot\Delta h\cdot A_{s_h} && (4.13)
\end{aligned}$$

The 3-parameter fit

$$R^2 \equiv \sum[y_i - f(t_i, C_m, C_d, f_3)]^2 \tag{4.14}$$

The 3 parameter fit is similar to the 2 parameter fit with correction, but instead of manually correcting for the discrepancy between the geometry and simulation geometry, this difference is included in the least squares equation as an unknown, f_3. This approach should lead to similar results for the cases unconstrained in heave and should help find the results for the other cases.

$$
\begin{aligned}
F_z(t) =& -\rho(C_M-1)V\ddot{r}(t) + \rho C_M V\dot{v}(t) + \frac{1}{2}\rho C_D A_h v_r(t)|v_r(t)| \\
& + \rho \cdot V(t) \cdot 9.81 + f_{z3} \\
F_y(t) =& -\rho(C_M-1)V\ddot{r}(t) + \rho C_M V\dot{v}(t) + \frac{1}{2}\rho C_D A_s v_r(t)|v_r(t)| \\
& + k \cdot (y(t) - y_0 - y_{\text{offset}}) + f_{y3} \\
F_y(t) =& -\rho(C_M-1)V\ddot{r}(t) + \rho C_M V\dot{v}(t) + \frac{1}{2}\rho C_D A_s v_r(t)|v_r(t)| \\
& + \rho \cdot 9.81 \cdot \Delta h \cdot A_{s_h} + f_{y3}
\end{aligned}
$$

5

Verification

With this study, a beginning will be made to quantify the error and uncertainty of the numerical wave tank. First, the definition of verification will be laid out in Section 5.1. Then next a convergence of the numerical wave tank will be presented.

5.1. Convergence and verification

Following the methodology given in [39], the simulation error δ_S is defined as the difference between the truth T and the simulation result S:

$$\delta_S = S - T = \delta_{SM} + \delta_{SN}$$

δ_{SM} represents the additive modelling error and δ_{SN} the numerical error. The numerical error consists of the iteration number δ_I, the grid size δ_G, time step δ_T and other input parameters δ_p. It is assumed that the other input parameters do not influence the error of the simulation, $\delta_P = 0$. The simulation was performed with double precision, indicating that the round-off error should be at least 15 digits, meaning it is negligible compared to the other errors. The numerical error results in

$$\delta_{SN}{=}\delta_I + \delta_G + \delta_T = \delta_I + \sum_{J}^{j=1} \delta_j \tag{5.1}$$

The uncertainty of the simulation can be described with

$$U_{SN}^2{=}U_I^2 + U_G^2 + U_T^2 \tag{5.2}$$

The Euler flow was used in Fluent with default settings. A time step is considered converged when the absolute difference between the scaled residuals is less then 0.001. Fluent reports scaled residuals, which is defined as scaled residual $= \frac{\text{residual}_{iteration\ N}}{max(\text{residual}_{iteration\ 1:5})}$. When the residual drops to 0.001 from the scaled residual, the equation is assumed to be converged. The iterative error and uncertainty is assumed to be equal to the convergence criteria, $\delta_I = 0.001$, $U_I = 0.001$.

In a convergence study for a (structured) grid with a uniform refinement ratio, the errors and uncertainties are defined with method presented below:

ϕ_i numerical solution, where $i = 1$ represents the finest mesh and the highest i represents the coarsest mesh. ϕ_{exact} represents the exact solution, The grid refinement ratio is defined as $r = h_{i+1}/h_i$ where h_i is the typical cell size and the lowest number corresponds to the finest mesh.

Roache,[35] and Ster, [39], define the convergence ratio, R, for a uniform grid refinement ratio r ,

$$R = \frac{\phi_2 - \phi_1}{\phi_3 - \phi_2} \tag{5.3}$$

with the following conditions

$0 < R < 1$	monotonic convergence
$-1 < R < 0$	oscillatory convergence
$R > 1$	monotonic divergence
$R < -1$	oscillatory divergence

For $-1 < R < 0$, the uncertainties can be determined using the oscillation maximum S_u and minimum, S_l, with $U_k = \frac{1}{2}(S_u - S_l)$.
For $0 < R < 1$, the error uncertainty can be defined with the following process for parameter k, first the refinement ratio r_k is defined and the order of accuracy is determined.

$$r_k = \frac{h_{i+1}}{h_i} = \left(\frac{N_i}{N_{i+1}}\right)^{(1/D)} \tag{5.4}$$

$$p_k = \frac{\ln(1/R)}{\ln r_k} \tag{5.5}$$

For a structured grid, the representative parameter size, h, is used to determine the r_k, for an unstructured grid N the number of nodes is used, where D represents the dimension (for a 2D simulation, $D = 2$) For a non-uniform refinement ratio, the order of accuracy is defined as:

$$p_k = \frac{\ln(1/R)}{\ln(r_{21})} - \frac{1}{\ln(r_{k_{21}})}\left(\ln(r_{32}^{p_k} - 1) - \ln(r_{21}^{p_k} - 1)\right) \tag{5.6}$$

The one-term term estimate of the error is defined as:

$$\delta^*_{RE_{k_1}} = \frac{\phi_2 - \phi_1}{r_k^{p_k} - 1} \tag{5.7}$$

Two methods for the estimation of the uncorrected uncertainties will be presented here. The highest uncertainty factor, between both method represents the uncertainty of the model.

Estimating errors and uncertainties with correction factor

According to Stern [39], correction factors provide a quantitative metric for defining the distance between the solution and the asymptotic range. Correction factors can be used to improve the error, $\delta^*_{RE_{k_1}}$ to $\delta^*_{k_1}$. The correction factor can be determined with:

$$C_k = \frac{r_k^{p_k} - 1}{r_k^{p_{k_{est}}} - 1} \tag{5.8}$$

$$\delta^*_{k_1} = C_k \delta^*_{REk_1} \tag{5.9}$$

The uncertainty factor U_k can now be determined with:

$$U_k = \begin{cases} [9.6(1 - C_k)^2 + 1.1]|\delta_{RE_{k_1}}| & |1 - C_k < 0| \quad (5.9a) \\ [2|1 - C_k| + 1]|\delta_{RE_{k_1}}| & |1 - C_k \geq 0| \quad (5.9b) \end{cases}$$

Estimating errors and uncertainties with Factors of Safety (CGI)

The Convergence Grid Index, or CGI, was developed by Roache. The uncertainty U_k is defined using the error estimate $|\delta^*_{REk_1}|$, multiplied by a factor of safety F_S.

$$U_k = F_S|\delta^*_{REk_1}| \tag{5.10}$$

for careful grid studies, $F_S = 1.25$ For unstructured grids, $F_S = 1.5$, [10].

5.2. Verification of the numerical wave tank

To help select a grid, and quantify the numerical error and uncertainty of the wave tank, a mesh convergence study has been performed.

5.2.1. Spatial convergence

A convergence study could be performed in several ways. One could keep one parameter constant, or keep a constant ratio, for example using the CFL number or by expressing dy, dz and dt as a function of the wave parameters. The order in which the convergence is studied could influence the result as well. Within literature there doesn't seem to be preference to a specific approach. ITTC, [16], states to only change one parameter, for example Δx, while Eça, [9] changes both Δx and Δy with H. Next Maguire, [27], uses a constant CFL for the convergence study while Kim, [22] changes only the number of cells along the wave length, locking the other parameters. It seems that at least 100 time steps per wave period are needed to get a good representation of the wave [17], and roughly 20 cells per wave height; these are chosen as the base mesh parameters for the convergence study. The number of cells per wave length varies: 150 cells per wave length was chosen for the base mesh (medium), [47], [22], [27] [44] [17] [50] [40] [11].

Table 5.1: Parameters of the mesh refinement study

	Extra coarse	Coarse	Medium	Fine
λ/dy	67	100	150	225
H/dz	9	14	20	30
T_p/dt	100	100	100	100
Node count, N	5354	10949	21330	44985

The domain can be found in Figure 4.3, the test section is at $2\cdot\lambda$ from the inlet, followed by a region of λ before the damping region starts. The size of the damping region was initially set to $1.5\cdot\lambda$, but this was increased to $3\cdot\lambda$ to lower the height of the reflected waves and put them further away from the test section, see Table 5.2.

Table 5.2: Convergence study for medium mesh, $1/2\ \lambda$ or 3λ, for wave amplitude a at location $i\cdot\lambda$ along the domain

Length damping region	airy wave	$\overline{a_{1\cdot\lambda}}$	$\overline{a_{2\cdot\lambda}}$	$\overline{a_{\text{outlet}-\lambda/4}}$
$1.5\cdot\lambda$	0.05	0.0378	0.0294	0.0123
$3\cdot\lambda$	0.05	0.0377	0.0294	0.0019

Table 5.3: Convergence study for $dt = T_p/100$

Location	airy wave, ϕ_{exact}	extra coarse, ϕ_4	coarse, ϕ_3	medium, ϕ_2	fine, ϕ_1
$\overline{a_{1\cdot\lambda}}$ $[m]$	0.05	0.0375	0.0377	0.0377	0.0378
$\overline{a_{2\cdot\lambda}}$ $[m]$	0.05	0.0291	0.0293	0.0294	0.0294
$\overline{a_{5.75\cdot\lambda}}$ $[m]$	0.05	0.0023	0.0020	0.0019	0.0019

The mean amplitude at $2\cdot\lambda$ from the inlet, see Table 5.3, was used to to determine R_G,

$$R_{Gc}=\frac{\phi_3-\phi_2}{\phi_4-\phi_3}=0.105, \qquad R_{Gf}=\frac{\phi_2-\phi_1}{\phi_3-\phi_2}=1.92$$

When considering the convergence ratio of the coarser meshes, R_{G_c}, the system converges monotonically. However the convergence ratio of the finer meshes, R_{G_f} diverges. Both R_{G_c} and R_{G_f} should lead to the same result. As R_{G_c} falls in the converging regime, and R_{G_f} in the diverging, it is assumed the solution converges in an oscillatory manner. The grid uncertainty can now be estimated with

$$U_G = \frac{1}{2}(S_U - S_L) = 1.56\cdot 10^{-4}$$

S_u represents the oscillation maximum, and S_L represents the oscillation minimum.
As the difference between the medium mesh and the fine mesh is relatively small, the medium mesh was chosen for the temporal convergence.

5.2.2. Temporal convergence

The temporal convergence ratio will be determined using the medium mesh, for 3 time step sizes. Table 5.4 shows tested time step sizes and the mean amplitude at along at the domain.
The mean amplitude improves significantly improves with a decreasing time step:

$$R_T=\frac{\phi_1-\phi_2}{\phi_2-\phi_3}=0.659$$

Table 5.4: Convergence study for the medium mesh

	airy wave, ϕ_{exact}	$T_p/100$, ϕ_3	$T_p/200$, ϕ_2	$T_p/400$, ϕ_1
$\overline{a_{1\cdot\lambda}}$ $[m]$	0.05	0.0377	0.0438	0.0474
$\overline{a_{2\cdot\lambda}}$ $[m]$	0.05	0.0294	0.0387	0.0448
$\overline{a_{5.75\cdot\lambda}}$ $[m]$	-	0.0019	0.0028	0.0035

R_T is in the monotonic convergence region The simulations were carried out with the following parameters:

$$
\begin{aligned}
r_T =& 2 \\
p_T =& \frac{\ln(1/R)}{\ln r_T} = 0.6016 \\
\delta^*_{RE_{T1}} =& \frac{\phi_2 - \phi_1}{r_T^{p_T} - 1} = -0.0118
\end{aligned}
$$

Using the correction factor approach, the error and uncertainty can be defined with the following.

$$
\begin{aligned}
C_T =& \frac{r_T^{p_T} - 1}{r_T^{p_{Test}} - 1} = \frac{2^{0.6016} - 1}{2^1 - 1} &= 0.5174 \\
\delta^*_{T_1} =& C_k \delta^*_{RET_1} &= 0.0061 \\
U_T =& [2|1 - C_T| + 1]|\delta_{RE_{T_1}}| &= 0.0232
\end{aligned}
$$

$p_{T_{est}} = 1$, as a 1st order implicit method was used for the time stepping. Using the CGI approach results in the following error and uncertainty, with $F_S = 1.5$ [10]

$$U_T = F_S |\delta^*_{REk_1}| = 0.0018$$

5.2.3. Numerical error and uncertainty

In the previous sections the numerical errors and uncertainties of the wave height were estimated. The iterative error and uncertainty, were unclear.

$$
\begin{aligned}
U^2_{SN} =& U^2_I + U^2_G + U^2_T \\
U_{SN} =& \sqrt{0.001^2 + (1.56 \cdot 10{-}4)^2 + 0.0018^2} = 0.0021
\end{aligned}
$$

The simulation error is incomplete, as the error δ_G is undefined. If δ_G is assumed to be zero, the order of δ_{SN} can be guestimated with:

$$
\begin{aligned}
\delta_{SN} =& \delta_I + \delta_G + \delta_T \\
\delta_{SN} =& 0.001 + (-0.0118) = -0.0128
\end{aligned}
$$

6

Results

In this chapter, the simulation results are evaluated. The hydrodynamic coefficients presented in this Chapter are plotted for a selected range of C_m and C_d against the KC number, KR and $\sqrt{KR}$, so that they can be compared to the data presented in Section 3.8. The full results can be found in Appendix C.

6.1. Results & discussion

6.1.1. 2 parameter fit

First, a global overview of the results will be given, after which the results will be discussed per motion. In section 3.8.3, the C_m and C_d for both a circle and rectangle with levels of submergence were shown. Even though the shapes are different, the coefficients cover a similar span. It is assumed the results from the barrier should fall within similar limits. Figure 6.2 gives an overview of the results, with the $y-$axis limited to expected values. Figure 6.3 shows the hydrodynamic coefficients of the cases with free motion in their corresponding unconstrained direction.

Coefficients in z

Figure C.1, shows the added mass in the heave direction. C_{m_z} has a large variation, with values ranging from -0.1 to 27.7. The drag ranges from -5.3 to 52.6. The outliers seem to be the cases 'fixed' and 'dof-y'. The common factor between these cases is their constraint in the z direction. One would expect the same outliers for the 'sway' and 'dof-yz' case, as these cases share a sway motion. Figure 6.2 shows the results of the different cases, capped to ranges similar to those found by Vugts.

C_{m_z} and C_{d_z} for the fixed cases are high compared to Vugts, with mass coefficients and drag coefficients ranging from -5 to 27.7. These results do not seem realistic.

Comparing the C_{m_z} results in heave for a cylinder and a rectangle to Vugts, as shown in Figure 6.2d, shows that the results are a order lower, as $C_{m_z} = C_{a_z} + 1$. Additionally the drag coefficient in heave are all negative. This does not seem feasible.

C_{m_z} and C_{d_z} for sway can not be determined, as both the velocity and the acceleration of the barrier in the z direction are zero.

The case that is free in heave, dof-z, shows much lower results, around 0.5. C_{d_z} is small, 0.05. Both C_{m_z} and C_{d_z} show good resemblance to the theoretical data from Greenhow, Figure 3.6b, for $(H/R \approx -0.8)$

C_{m_z} for dof-y varies between 4.5 and 27.7, C_{d_z} varies between 3.6 and 52.6. These values do not seem feasible as the values of both coefficients are high.

C_{m_z} for dof-yz spans a large band, resembling both heave and dof-z. The coefficient drops below 0 for λ_{short}. C_{d_z} is small and similar to the drag coefficients of dof-z.

Coefficients in y

The coefficients in the y direction vary between -12 and 2. The outliers are the cases constrained in y, opposite to what was found with C_{m_z}.

C_{m_y} in the fixed cases lies between -8 and -11, the drag coefficient between -1.6 to 2.0. The mass coefficients are all outside of the expected range of $C_{m_y} = 0$ to $C_{m_y} = 8$.

C_{m_y} and C_{d_y} can not be determined in heave, as the velocity and acceleration in the y direction are zero. Looking at Figure C.8, heave, one can see that the load is only due to the water level difference.

C_{m_y} due to sway are all negative, between -0.9 and -2.4. C_{d_y} varies between -0.2 and 1.9

For dof-z, $C_{m_y} \approx -11$, C_{d_y} varies between -0.8 and 1.9.

C_{m_y} with dof-y, lies between 0.2 and 0.5, this lies in a similar regime as Figure 3.7c. C_{d_y} lies between 0.3 and 0.8, both Vugts and Greenhow found $C_{d_y} \approx 0$, for a circle and a rectangle. However, Vugts presents in his report also a triangle, where the drag coefficients from the experiment are an order 0.2 higher than the predicted theoretical value (comparable to Figure 3.7c). While $C_{d_y} = 0.8$ is probably too high, the values do not seem infeasible.

C_{m_y} dof-yz shows similar values to dof-y, but with ≈ 0.25 difference. As the barrier with dof-yz can move both in heave and sway with the wave, its relative acceleration is small, hence its added mass could be lower than a constrained system. C_{d_y} in dof-yz is similar to dof-y.

6.1.2. 2 parameter fit and the 3 parameter fit

The results of the 2 parameter fit and the 2 parameter fit lead to different results for the cases free in heave. This is due to the correction of $(\overline{V} \cdot \rho - \text{mass}) \cdot 9.81$. This correction only adjusts the offset. It does not adjust the instantaneous volume and area. One could say that due to this, skews the results, as only a part of the error is corrected. However, a least square fit to sinusoidal needs the be placed at the mean; otherwise the results will be infeasible. As was found in the constrained cases for the 2 parameter fit. The results can be found in Figure 6.1 and Appendix C.

Coefficients in z

Figure C.3, shows the added mass in the heave direction. C_{m_z} has a some variation, with values ranging from -1.9 to 7.8. The drag ranges from -11.1 to 13.4. The outliers seem to be the cases 'fixed' and 'dof-y', as was found with the 2 parameter fit. The common factor between these cases is their constraint in the z direction. One would expect the same outliers for the 'sway' and 'dof-yz' case, as these cases share a sway motion. Figure 6.1 shows the results of the different cases, capped to ranges similar to those found by Vugts.

C_{m_z} and C_{d_z} for the fixed cases are high compared to Vugts, with mass coefficients and drag coefficients ranging from -11.1 to 11.6. $C_{m_z} < 0$ is not feasible according to Sarpkaya, [38].

Comparing the C_{m_z} results in heave for a cylinder and a rectangle to Vugts, as shown in Figure 6.1d, shows that the numerical results are approximately a factor 1. lower. Additionally the drag coefficient in heave are all negative. This does not seem feasible.

C_{m_z} and C_{d_z} for sway are undetermined, as the velocity and the acceleration are null.

The case that is free in heave, dof-z, finds low hydrodynamic coefficients, $C_{m_z} \approx 0.1$ and $C_{d_z} \approx 0.1$. C_{d_z} shows resemblance to the theoretical data from Greenhow, Figure 3.6b, $(H/R \approx -0.8)$. C_{m_z} resembles C_{a_z} of Greenhow.

C_{m_z} for dof-y varies between 0 and 7.8, C_{d_z} varies between -4.4 to 13.4. The negative drag was not expected. Both the drag and the mass coefficients are higher than those found in literature.

C_{m_z} for dof-yz spans a small band, resembling dof-z. The coefficient drops below 0 for λ_{short}. C_{d_z} is small and similar to the drag coefficients of dof-z.

Coefficients in y

The coefficients in the y direction vary between -11 and 3. The outliers are the cases constrained in y, opposite to what was found with C_{m_z}.

C_{m_y} in the fixed cases lies between -10.9 and -8.3, the drag coefficient varies between -1.5 and 2.0. The mass coefficients are negative, which is infeasible according to Sarpkaya.

C_{m_y} and C_{d_y} can not be determined in heave, as the velocity and acceleration in the y direction are zero. Looking at Figure C.8, heave, one can see that the load is only due to the water level difference.

C_{m_y} due to sway are all negative, between -0.9 and -2.4. C_{d_y} varies between -0.2 and 1.9

For dof-z, $C_{m_y} \approx -11$, C_{d_y} varies between -0.8 and 1.9.

C_{m_y} for dof-y, lies between 0.2 and 0.5, which is a similar regime as Figure 3.7c. C_{d_y} lies between 0.3 and 0.8, while both Vugts and Greenhow found $C_{d_y} \approx 0$ for a circular and a rectangular cross-section. However, Vugts also presents a triangle in his report, where the drag coefficients from the experiment are an order 0.2 higher than the predicted theoretical value (comparable to Figure 3.7c). While $C_{d_y} = 0.8$ is probably too high, the values do not seem infeasible.

C_{m_y} dof-yz shows similar values to dof-y, but with ~ 0.2 difference. As the barrier with dof-yz can both in heave and sway with the wave, its relative acceleration is small, hence its added mass could be lower than a constrained system. C_{d_y} in dof-yz is similar to dof-y.

6.1.3. Relation motion direction & coefficients

From the results, it seems that a simulation of a motion in one direction can not be used to determine the motion in the other directions.

For a system free to move in sway due to waves, the vertical wave component should be enough to determine the coefficients; as it is in the constrained direction similar to the fixed case in waves.

6.1.4. Reliability

From the above can be concluded that in the imposed motion cases and the constrained case all lead unrealistic results in certain ways. The hydrodynamic coefficients are linked and for example for heave, if C_{m_z} looks feasible, but C_{d_z} has infeasible results; what does this say about the result as a whole? Figure C.8 and C.9, fixed, shows a clear build up of the load. The varying water level difference, dh and water level V, have an impact on the result. dof-z shows a difference, which was in Section 4.5 proven to be due to a difference in the volume and the realised volume in the simulation. This discrepancy has an impact, and this could attribute to the infeasibility of some results. As the volume and area corresponding to the load contain an error, so does the result.

In Appendix C, Figure C.3 shows how trying to correct for the volume difference influences the results. The high coefficients for C_{m_z} and C_{d_z} are closer to the expectation.

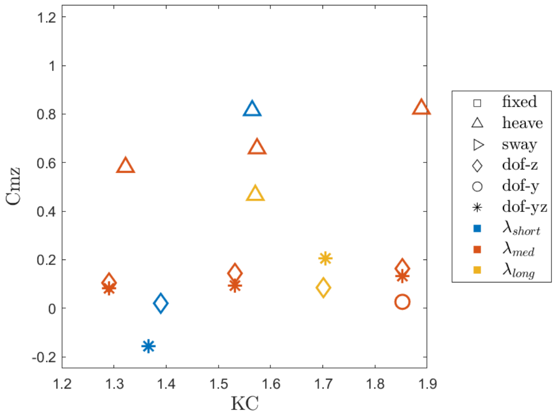

(a) Cmz, 3 parameters

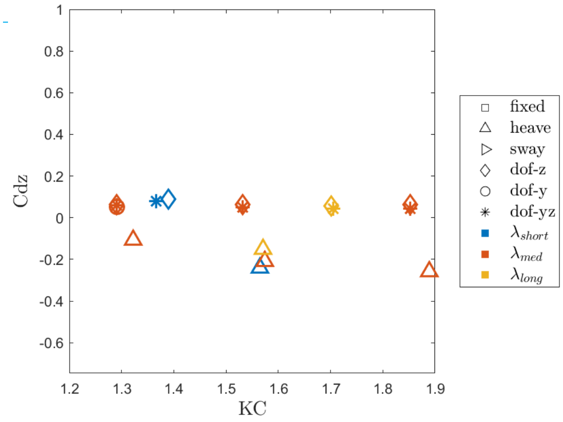

(b) Cdz, 3 parameters

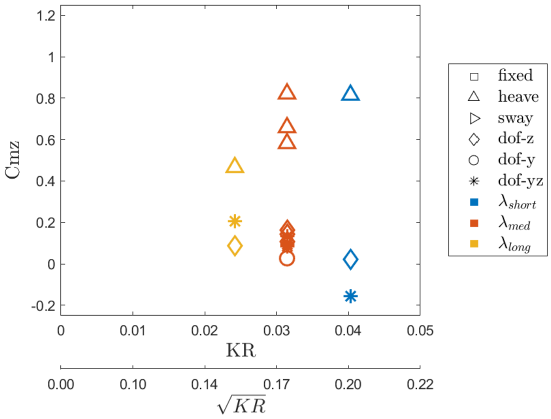

(c) Cmz, 3 parameters

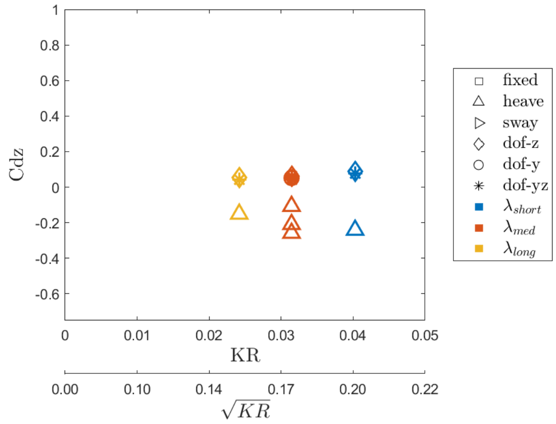

(d) Cdz, 3 parameters

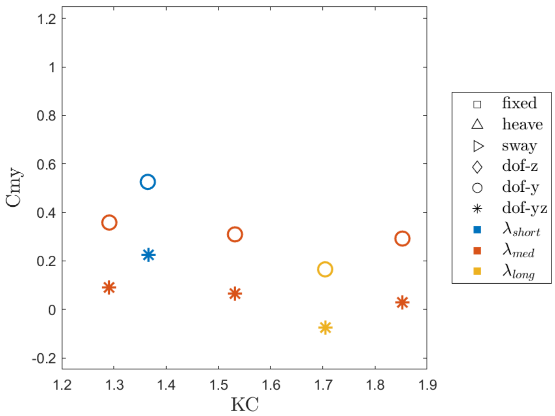

(e) Cmy, 3 parameters

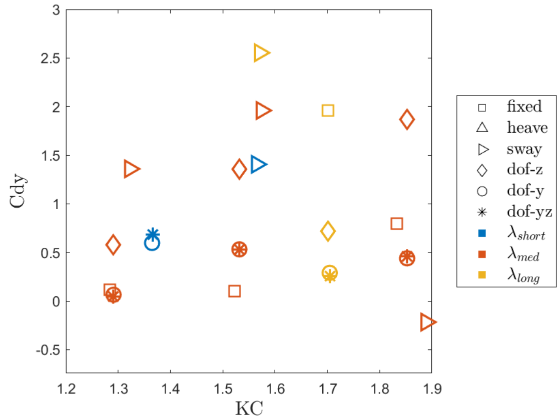

(f) Cdy, 3 parameters

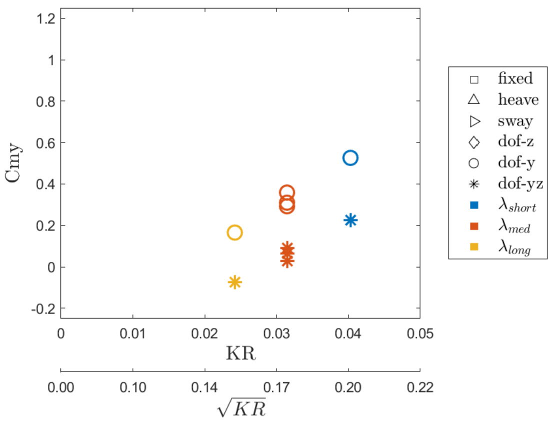

(g) Cmy, 3 parameters

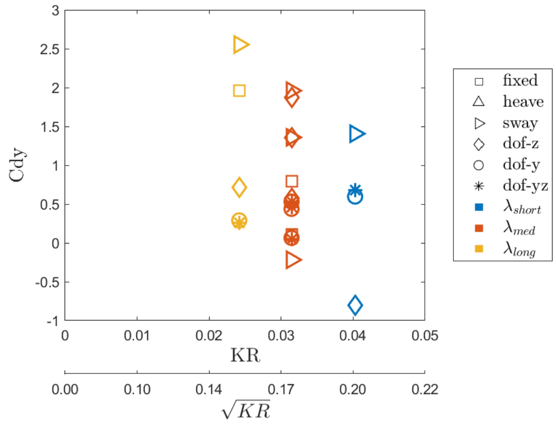

(h) Cdy, 3 parameters

Figure 6.1: Hydrodynamic coefficients with 3 parameter fit

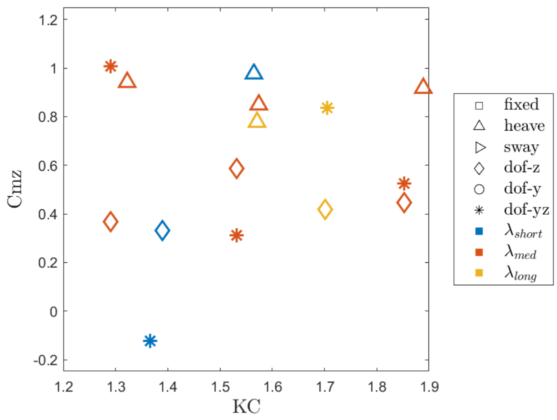

(a) Cmz, 2 parameters

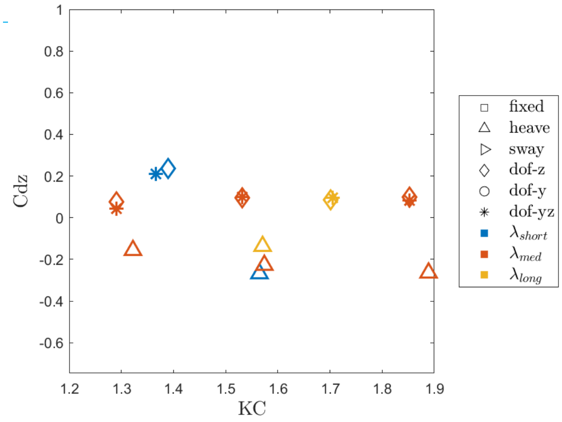

(b) Cdz, 2 parameters

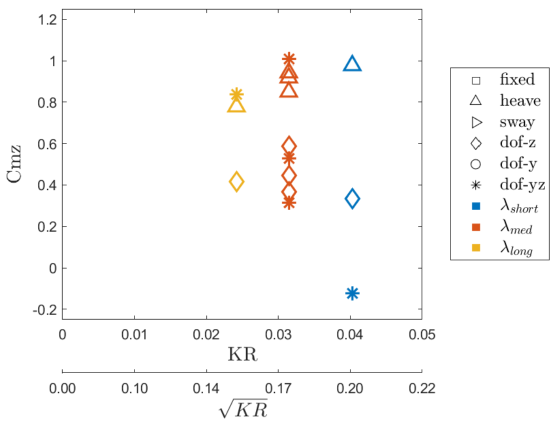

(c) Cmz, 2 parameters

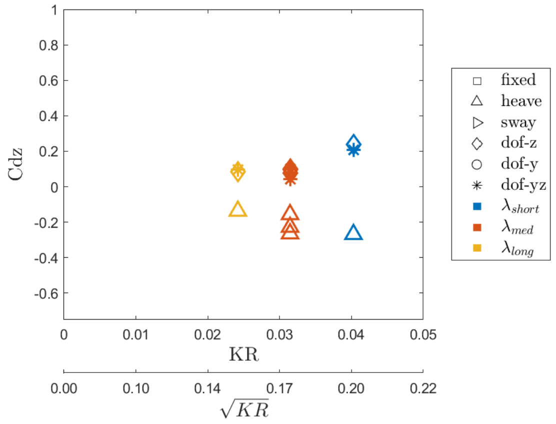

(d) Cdz, 2 parameters

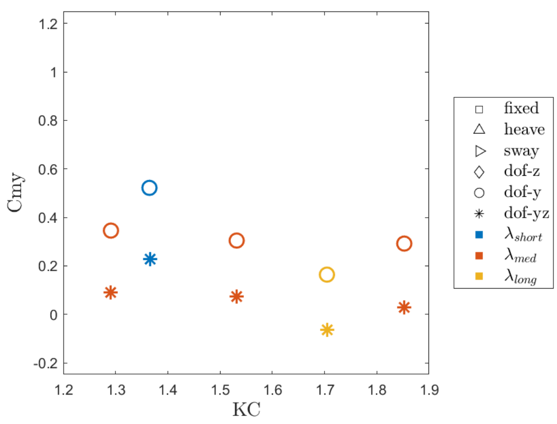

(e) Cmy, 2 parameters

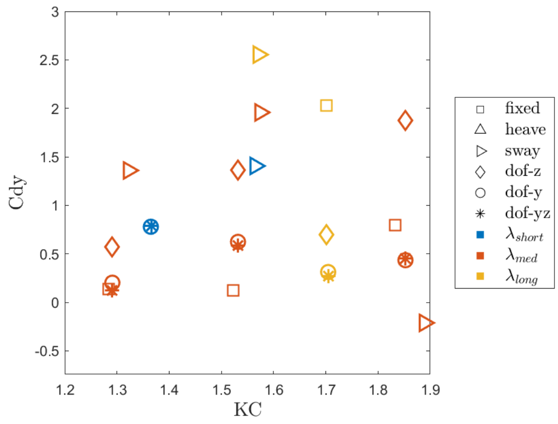

(f) Cdy, 2 parameters

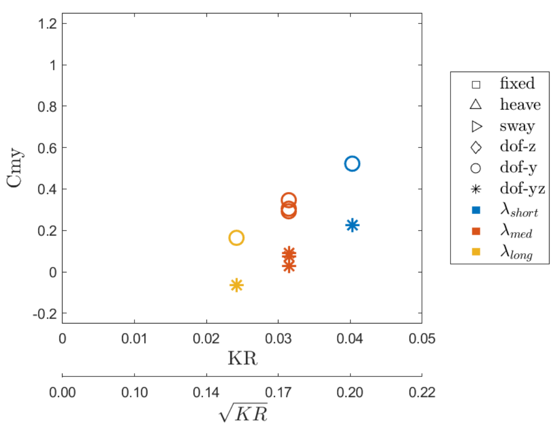

(g) Cmy, 2 parameters

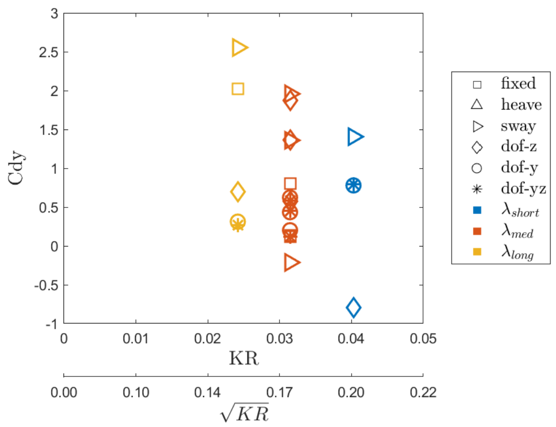

(h) Cdy, 2 parameters

Figure 6.2: Hydrodynamic coefficients with 2 parameter fit

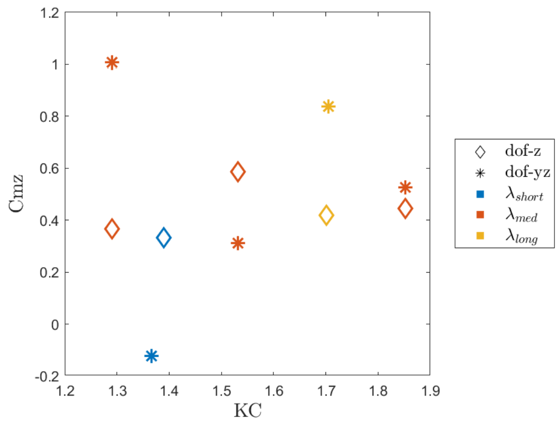

(a) Cmz, 2 parameters

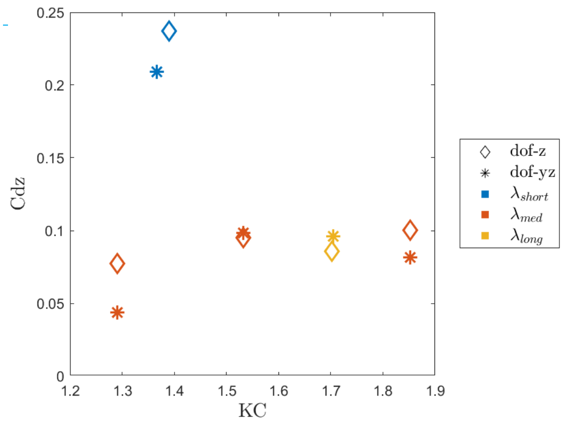

(b) Cdz, 2 parameters

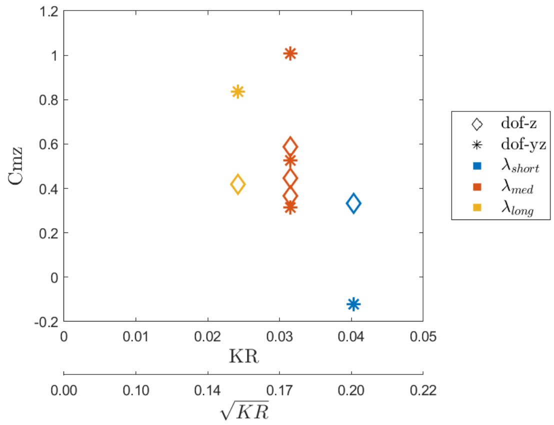

(c) Cmz, 2 parameters

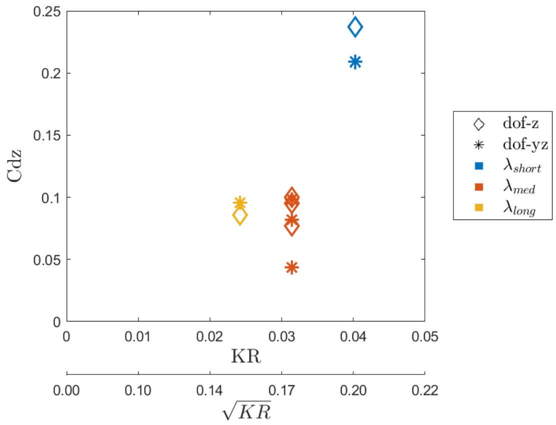

(d) Cdz, 2 parameters

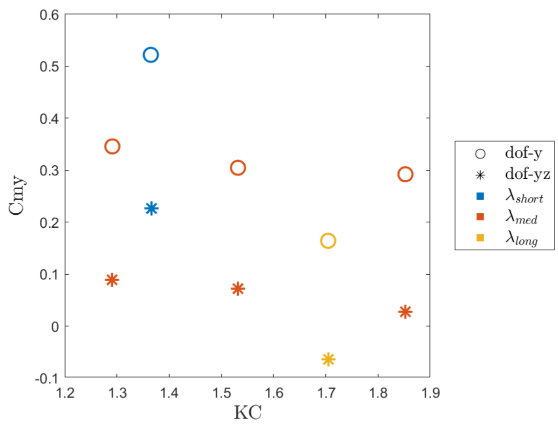

(e) Cmy, 2 parameters

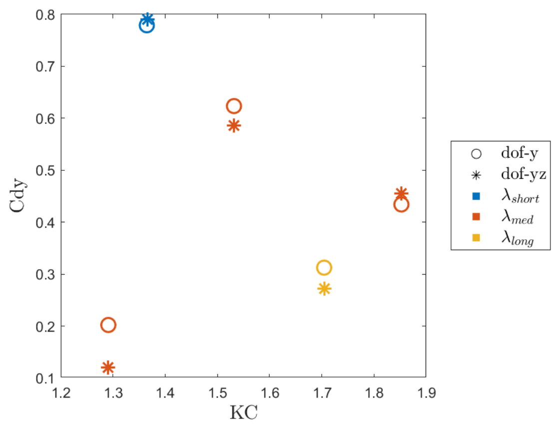

(f) Cdy, 2 parameters

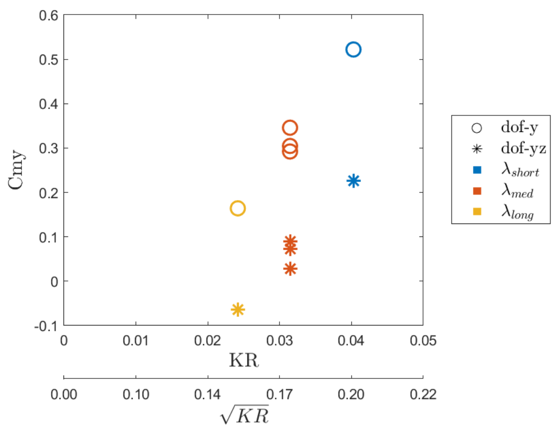

(g) Cmy, 2 parameters

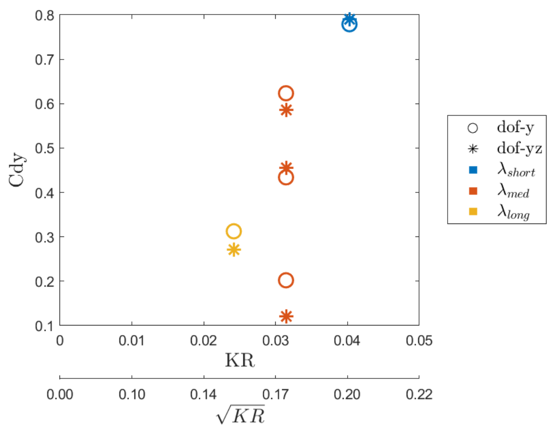

(h) Cdy, 2 parameters

Figure 6.3: Hydrodynamic coefficients with 2 parameter fit

7
Validation

To demonstrate the accuracy of the model, the results of the numerical model were compared to model tests carried out by MARIN.

7.1. Comparison of the data

In this section the data from the MARIN model and the numerical model will be presented. Figure 7.1 shows the results from numerical model next to the experimental results from MARIN. The starting time of the numerical results in the plot has been adjusted to match the starting time of the experiments, to simplify the comparison.

7.1.1. MARIN current

In the MARIN test, the current velocity is gradually ramped up to $v = 0.22$ $[m/s]$. The model is free to move and rotate. The barrier initially overshoots and oscillates and stabilises, see Figure 7.1a. The force data from the MARIN test was originally positive, due to a different coordinate system. It has been converted to make the comparison to the numerical model easier. The model is considered to have reached a stable condition at $t = 71.4$ s. The statistics were carried out on a time window of $t = [71.4 : 214.1]$.
For the numerical model, the domain was initialized with the current velocity. This means that the barrier is subjected to an instantaneous load. The barrier overshoots and starts oscillating. This movement is considered stabilised after 100 $[s]$ in Figure 7.1a. The statics are determined on the time window $t = [90 : 210]$. The forces

Table 7.1: Comparison between MARIN and Fluent, model scale, for a current velocity of 0.22 m/s

	v $[m/s]$	$\overline{F}$ $[N]$	σ_F $[N]$	$\max F$ $[N]$
MARIN, LM_RW_FM23908003003	0.22	-16.53	0.64	-18.64
Fluent, free in sway and heave, dof-yz	0.22	-4.51	0.16	-4.84
Ratio Fluent/MARIN		0.27		0.26

determined with Fluent are a ≈ 4 times lower than those determined in MARIN.

7.1.2. MARIN waves

For the wave tests the statistics on the MARIN model were performed on a time window, $t = [71.4 : 142.75]$. For the numerical model the statistic are performed over 6 wave periods on the time window $t = [47.44 : 65.35]$ $[s]$.

The forces determined with the numerical model for the wave tests correspond well to the experimental results from MARIN. The mean force is 0.6 times lower in the numerical model. The maximum force is 1.8 times higher. As the numerical model is constrained in rotation, unlike the MARIN model, higher loads are to be expected.

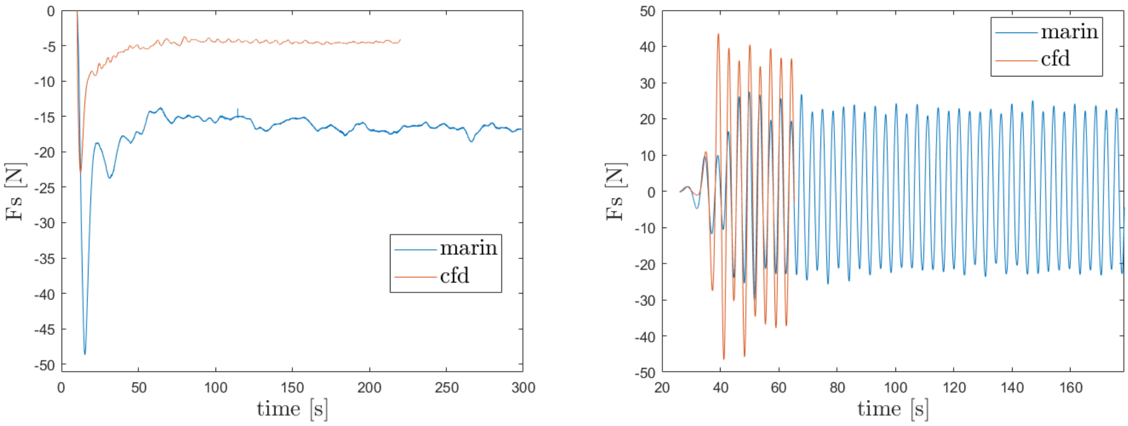

(a) The barrier in current, $v = 0.224\ [m/s]$

(b) The barrier in regular waves, $H = 0.12\ [m]$

Figure 7.1: The numerical model versus the model from MARIN

Table 7.2: Comparison between MARIN and Fluent, model scale, for a wave height of 0.075 m

	$H\ [m]$	effective $H\ [m]$	$\overline{F}\ [N]$	$\sigma_F\ [N]$	$\max F\ [N]$
MARIN, LM_RW_FM23908004002	0.15	0.146	0.30	16.2	25.7
Fluent, free in sway and heave, dof-yz	0.15	0.13	-0.19	27.0	-45.8
Ratio Fluent/MARIN			0.6		1.8

7.2. Discussion

It would be expected that the loads from the loads from both simulations would be higher than those from the experimental data, as the barrier is unable to rotate, unlike the experiments at MARIN. Perhaps the differences are due to 3D effects. In the current case, vortices can build up from the end plates and the bottom of the barrier, while in the wave case the build up gets disrupted by the oscillating velocity.

8 Discussion

In this a thesis project, a model has been set up to evaluate the hydrodynamic coefficients of a floating barrier in regular waves. The barrier is composed of a cylindrical floater and a skirt. As such, it has an exotic shape within the offshore world.

The barrier was simulated using a numerical model as wave tank. This numerical wave tank has been preliminarily verified with the linear wave theory, in order to optimise the mesh resolution. The barrier with 2 degrees of freedom, sway and heave, has been compared to model tests performed at MARIN. Considering the model at MARIN had 3 degrees of freedom and viscosity effects are neglected, the numerical model compares fairly well to the wave model test.

The hydrodynamic coefficients were determined from the response of the numerical model. The barrier loads and motions were in post-processing determined with the Morison equation by a least squares method. The results for the hydrodynamic coefficients vary between the different cases. This can partially be attributed to a difference between the expected and simulated volume. The coefficients derived from cases with a forced motion are not a good match with the results from literature. The coefficients from free motion cases, dof-y, dof-z and dof-yz results do show a good similarities with literature results. These results indicate that the mass coefficient of the barrier in both y and z is close to zero. This is lower than the standard used in the literature, where $C_m \approx 2$. Using $C_m \approx 2$ in the design would result in an overestimation of the loads. This thesis shows that a C_m close to zero could seems the most robust estimation.

From the results, it can be concluded that the free surface has a big impact on the system and the determination of the hydrodynamic coefficients. It also shows that relatively small accumulative errors can have a big impact on the result. As differences in the results from to both the theory and the model experiment are quite big, the setup as it was used here, would not be recommended for the determination of the hydrodynamic coefficients and loads. Perhaps if these discrepancies could be resolved, this could be a reliable tool. The results from this thesis do imply that the hydrodynamic coefficients are lower than the commonly used coefficients.

Improvements to the model could be made by decreasing or resolving the discrepancies between the volume and area in the simulation and in the post-processing. This could also attribute to better results. Next the velocity in the heave direction was taken at $z = -H/2$, relative to the free surface. Perhaps the model could be improved by taking the velocity at a reference point closer to the bottom of the floater. Some of the results of C_m show good comparison to C_a from literature. Even though the approach in this thesis has been checked, perhaps a mistake has been made and all values found here as C_m are representing C_a. Lastly, the hydrodynamic coefficients were determined for a small range of wave lengths and KC, it would be interesting to investigate the hydrodynamic coefficients of higher and lower wave lengths.

References

[1] ENVIRONMENTAL CONDITIONS AND ENVIRONMENTAL LOADS. Technical Report October, Det Norske Veritas, 2007.

[2] John D Anderson. *Fundamentals of Aerodynamics*. McGraw-Hill, New York, 2011. ISBN 978-0-07-339810-5.

[3] Roberto Brambini. MARIN TEST POST-PROCESSING AND ORCAFLEX MODELING. Technical report.

[4] Subrata K. Chakrabarti. *Handbook of offshore engineering*, volume I. 2005. ISBN 9780080443812. URL https://www.sciencedirect.com/science/book/9780080443812.

[5] T.S.J. de Feijter. *Mesoscale hydromechanics of a mobile plastic catching system*. PhD thesis, TU Delft, 2017. URL http://resolver.tudelft.nl/uuid:f1004d60-ea71-4a96-bfb3-3bf34a789092.

[6] Anthony Graham Dixon. *Wave Forces on Cylinders*. PhD thesis, University of Edinburgh, 1980.

[7] DNV GL. DNV RP-H103 Modelling and Analysis of Marine Operations. *Model. Anal. Mar. Oper.*, (February):157, 2014. URL http://www.dnvgl.com.

[8] Bénédicte Dommergues, Roberto Brambini, René Mettler, Zaki Abiza, and Bruno Sainte-Rose. Hydrodynamics and Capture Efficiency of Plastic Cleanup Booms: Part II — 2D Vertical Capture Efficiency and CFD Validation. In *Vol. 2 Prof. Carl Martin Larsen Dr. Owen Oakley Honor. Symp. CFD VIV*, number June, page V002T08A025. ASME, jun 2017. ISBN 978-0-7918-5764-9. doi: 10.1115/OMAE2017-62012. URL http://proceedings.asmedigitalcollection.asme.org/proceeding.aspx?doi=10.1115/OMAE2017-62012.

[9] L. Eça and M. Hoekstra. A procedure for the estimation of the numerical uncertainty of CFD calculations based on grid refinement studies. *J. Comput. Phys.*, 262:104–130, apr 2014. ISSN 00219991. doi: 10.1016/j.jcp.2014.01.006. URL http://dx.doi.org/10.1016/j.jcp.2014.01.006http://linkinghub.elsevier.com/retrieve/pii/S0021999114000278.

[10] Francisco Elizalde-Blancas and Patrick J Roache. An Evaluation of the GCI for Unstructured Grids.

[11] William Finnegan and Jamie Goggins. Linear irregular wave generation in a numerical wave tank. *Appl. Ocean Res.*, 52:188–200, 2015. ISSN 01411187. doi: 10.1016/j.apor.2015.06.006. URL http://linkinghub.elsevier.com/retrieve/pii/S0141118715000802.

[12] Fluent. ANSYS FLUENT User ' s Guide. Technical Report November, 2011.

[13] M. Greenhow and S.I. Ahn. Added mass and damping of horizontal circular cylinder sections. *Ocean Eng.*, 15(5):495–504, 1988. ISSN 00298018. doi: 10.1016/0029-8018(88)90012-1.

[14] Bas Hofland and Mirjam van der Mheen. 2D Physical model tests for The Ocean Cleanup. Technical report.

[15] Leo H. Holthuijsen. *Waves in Oceanic and Coastal Waters*. Cambridge University Press, Cambridge, 2007. ISBN 9780511618536. doi: 10.1017/CBO9780511618536. URL http://ebooks.cambridge.org/ref/id/CBO9780511618536.

[16] ITTC. ITTC - Recommended Procedures and Guidelines Uncertainty Analysis in CFD ,Verification and Validation Methodology and Procedures. Technical report, ITTC, 2002.

[17] ITTC. ITTC – Recommended Procedures and Guidelines ITTC Quality System Manual Practical Guidelines for Ship CFD Applications ITTC – Recommended Procedures and Guidelines. Technical report, ITTC, 2014.

[18] J M J Journée and W W Massie. *Offshore Hydromechanics*. Delft University of Technology, 2nd edition, 2008.

[19] J M J Journée, W W Massie, and R H M Huijsmans. *Offshore Hydromechanics*. Delft University of Technology, 3rd edition, 2015.

[20] Garbis H Keulegan and Lloyd H Carpenter. Forces on Cylinders and Plates in an Oscillating Fluid. *J. Res. Natl. Bur. Stand. (1934).*, 60(5), 1958.

[21] Cheung Hun. Kim. *Nonlinear waves and offshore structures*. World Scientific,, Hackensack, N.J ;, 2008. ISBN 9810248849 9789810248840 9810248857 9789810248857.

[22] Sung-Yong Kim, Kyung-Mi Kim, Jong-Chun Park, Gyu-Mok Jeon, and Ho-Hwan Chun. Numerical simulation of wave and current interaction with a fixed offshore substructure. *Int. J. Nav. Archit. Ocean Eng.*, 8(2):188–197, 2016. ISSN 20926782. doi: 10.1016/j.ijnaoe.2016.02.002. URL http://linkinghub.elsevier.com/retrieve/pii/S2092678216000285.

[23] Alexandr I. Korotkin. *Added Masses of Ship Structures*, volume 88 of *Fluid Mechanics and Its Applications*. Springer Netherlands, Dordrecht, 2009. ISBN 978-1-4020-9431-6. doi: 10.1007/978-1-4020-9432-3. URL http://link.springer.com/10.1007/978-1-4020-9432-3.

[24] D Kristiansen and O M Faltinsen. A study of wave loads on fixed horizontal cylinders in the free surface. *Proc. 8th Int. Conf. Hydrodyn.*, 10(October 2014), 2008.

[25] Enrique J. Laya, Jerome J. Connor, and S. Shyam Sunder. Hydrodynamic Forces on Flexible Offshore Structures. *J. Eng. Mech.*, 110(3):433–448, mar 1984. ISSN 0733-9399. doi: 10.1061/(ASCE)0733-9399(1984)110:3(433). URL http://ascelibrary.org/doi/10.1061/{%}28ASCE{%}290733-9399{%}281984{%}29110{%}3A3{%}28433{%}29.

[26] C M Lee and H D Jones. Prediction of Motion and Hydrodynamic Loads of Catamarans. 1973. ISSN 00253316.

[27] Andrew Eoghan Maguire. *Hydrodynamics , control and numerical modelling of absorbing wavemakers Doctor of Philosophy*. PhD thesis, The University of Edinburgh, 2011.

[28] Marin. 29239_GA Rigid Model.pdf. Technical report, 2016.

[29] Marinwiki. Coordinate systems - MARIN, 2011. URL https://wiki.marin.nl/index.php/Coordinate{_}systems.

[30] M. McIver and P. McIver. The added mass for two-dimensional floating structures. *Wave Motion*, 64: 1–12, 2016. ISSN 01652125. doi: 10.1016/j.wavemoti.2016.02.007. URL http://dx.doi.org/10.1016/j.wavemoti.2016.02.007.

[31] P. McIver and D. V. Evans. The occurrence of negative added mass in free-surface problems involving submerged oscillating bodies. *J. Eng. Math.*, 18(1):7–22, 1984. ISSN 00220833. doi: 10.1007/BF00042895.

[32] Rene Mettler. POS-BA-CA-XXX - Simulation overview Marine. 2016.

[33] Mark Paalvast. Marin Offshore Basin Model Tests. Technical report, MOCEAN, 2015.

[34] Dr. Adina Paytan. Lecture 3: Temperature, salinity, density and ocean circulation. URL http://ocean.stanford.edu/courses/bomc/chem/lecture{_}03.pdfhttp://ocean.stanford.edu/courses/bomc/chem/lecture{%}7B{_}{%}7D03.pdf.

[35] Patrick J Roache. QUANTIFICATION OF UNCERTAINTY IN COMPUTATIONAL FLUID DYNAMICS. *Annu. Rev. Fluid Mech.*, 29(1):123–160, jan 1997. ISSN 0066-4189. doi: 10.1146/annurev.fluid.29.1.123. URL http://www.annualreviews.org/doi/abs/10.1146/annurev.fluid.29.1.123.

[36] Turgut Sarpkaya. A critical review of the intrinsic nature of vortex-induced vibrations. 19:389–447, 2004. doi: 10.1016/j.jfluidstructs.2004.02.005.

[37] Turgut. Sarpkaya. On the parameter β = Re/KC = D2/νT. *J. Fluids Struct.*, 21(4):435–440, 2005. ISSN 08899746. doi: 10.1016/j.jfluidstructs.2005.08.007.

[38] Turgut Sarp Sarpkaya. *Wave Forces on Offshore Structures.* Cambridge University Press, 2010. ISBN 978-0-521-89625-2. URL https://app.knovel.com/hotlink/toc/id:kpWFOS0004/wave-forces-offshore/wave-forces-offshore.

[39] Frederick Stern, Robert Wilson, and Jun Shao. Quantitative V&V of CFD simulations and certification of CFD codes. *Int. J. Numer. Methods Fluids*, 50(11):1335–1355, apr 2006. ISSN 0271-2091. doi: 10.1002/fld.1090. URL http://doi.wiley.com/10.1002/fld.1090.

[40] Tahsin Tezdogan, Yigit Kemal Demirel, Paula Kellett, Mahdi Khorasanchi, Atilla Incecik, and Osman Turan. Full-scale unsteady RANS CFD simulations of ship behaviour and performance in head seas due to slow steaming. *Ocean Eng.*, 97:186–206, 2015. ISSN 00298018. doi: 10.1016/j.oceaneng.2015.01.011. URL http://dx.doi.org/10.1016/j.oceaneng.2015.01.011.

[41] TOC. A feasibility study. Technical report, 2014. URL http://www.theoceancleanup.com/.

[42] TOC and Mocean Offshore bv. CALIBRATION NUMERICAL 2D MODELS. Technical report.

[43] J.K. Vandiver. Dimensionless Parameters Important to the Prediction of Vortex-Induced Vibration of Long, Flexible Cylinders in Ocean Currents. *J. Fluids Struct.*, 7(5):423–455, jul 1993. ISSN 08899746. doi: 10.1006/jfls.1993.1028. URL https://doi.org/10.1006/jfls.1993.1028http://linkinghub.elsevier.com/retrieve/pii/S0889974683710285.

[44] G. Vaz, F. Jaouen, and M. Hoekstra. Free-Surface Viscous Flow computations. Validation of Urans Code Fresco. *ASME 28th Int. Conf. Ocean. Offshore Arct. Eng.*, pages 1–13, 2009. doi: 10.1115/OMAE2009-79398.

[45] J.H. Vugts. The hydrodynamic coefficients for swaying, heaving and rolling cylinders on a free surface. Technical report, 1968.

[46] Eric W. Weisstein. Circular Segment. URL http://mathworld.wolfram.com/CircularSegment.html.

[47] Christian Windt, Josh Davidson, Pal Schmitt, and John V Ringwood. Assessment of Numerical Wave Makers. In *12th Eur. Wave Tidal Energy Conf.*, number 1, pages 1–10, 2017.

[48] J. Wolfram and M. Naghipour. On the estimation of Morison force coefficients and their predictive accuracy for very rough circular cylinders. *Appl. Ocean Res.*, 21(6):311–328, 1999. ISSN 01411187. doi: 10.1016/S0141-1187(99)00018-8.

[49] Zhida Yuan and Zhenhua Huang. Morison coefficients for a circular cylinder oscillating with dual frequency in still water: an analysis using independent-flow form of Morison's equation. *J. Ocean Eng. Mar. Energy*, 1(4):435–444, 2015. ISSN 21986452. doi: 10.1007/s40722-015-0030-6.

[50] Xi Zeng Zhao, Chang Hong Hu, and Zhao Chen Sun. Numerical simulation of extreme wave generation using VOF method. *J. Hydrodyn.*, 22(4):466–477, 2010. ISSN 10016058. doi: 10.1016/S1001-6058(09)60078-0. URL http://dx.doi.org/10.1016/S1001-6058(09)60078-0.

A

Hydrodynamic coefficients

A.1. Determining the added mass and drag using the Fourier series

Following Keulegan and Carpenter, [20], when the velocity is assumed to vary harmonically, $u = u_m \cos(\theta)$, where $\theta = \frac{2\pi t}{T}$, the force is periodic. The force can be assumed to depend on the following dimensions, $F = f(t, T, u_m, D, \rho, \nu)$. In Equation A.1 the force is made nondimensional and the variables are grouped in the Keulegan Carpenter number, the Reynolds number.

$$\frac{F}{\rho u_m^2 D} = f\big(\theta, \frac{u_m T}{D}, \frac{u_m D}{\nu}\big) \tag{A.1}$$

Expanding the F to a Fourier series,

$$\begin{aligned}\frac{F}{\rho u_m^2 D} &= A_1 \sin\theta + A_3 \sin 3\theta + A_5 \sin 5\theta + \, ... \\ &+ B_1 \cos\theta + B_3 \cos 3\theta + B_5 \cos 5\theta + \, ...\end{aligned} \tag{A.2}$$

$$\text{where} \quad A_n = \frac{1}{\pi}\int_0^{2\pi} \frac{F \sin n\theta}{\rho u_m^2 D} d\theta, \quad B_n = \frac{1}{\pi}\int_0^{2\pi} \frac{F \cos n\theta}{\rho u_m^2 D} d\theta \tag{A.3}$$

substituting the velocity into equation A.1

$$\frac{F}{\rho u_m^2 D} = \frac{\pi}{4} \cdot C_m \cdot \frac{2\pi D}{T u_m} \sin\theta - \frac{C_d}{2} \cos\theta |\cos\theta| \tag{A.4}$$

First the B_n coefficients will be determined, by expanding the $|\cos\theta|\cos\theta$ term

$$\begin{aligned}|\cos\theta|\cos\theta &= \sum_{n=0}^{2\pi} \frac{\int_0^{2\pi} |\cos\theta|\cos\theta \cos n\theta d\theta}{\int_0^{2\pi} \cos^2 n\theta d\theta} \\ &= a_0 + a_1\cos\theta + a_2\cos 2\theta + a_3 \cos 3\theta \\ \text{then} \quad & a_n = 0 \text{ for } n \text{ even,} \\ & a_n = (-1)^{\frac{n+1}{2}} \frac{8}{n(n^2-4)\pi} \text{ for } n \text{ odd,} \\ & a_1 = \frac{8}{3\pi}, \; a_3 = \frac{8}{15\pi}, \; ...\end{aligned} \tag{A.5}$$

rewrite A.5 to match A.2

$$\begin{aligned} a_1 \cos\theta &= |\cos\theta|\cos\theta - a_3\cos 3\theta - a_5 \cos 5\theta - ... \\ \cos\theta &= \frac{|\cos\theta|\cos\theta}{a_1} - \frac{a_3\cos 3\theta}{a_1} - \frac{a_5\cos 5\theta}{a_1} - ... \\ B_1' \cos\theta &= \frac{B_1}{a_1}|\cos\theta|\cos\theta - \frac{a_3}{a_1}B_1\cos 3\theta - \frac{a_5}{a_1}B_1\cos 5\theta - ...\end{aligned} \tag{A.6}$$

Comparing Equation A.6 in Equation A.2, coefficients can be rewritten to

$$B_1' = \frac{B_1}{a_1}, \quad B_3' = B_3 - \frac{a_3}{a_1}B_1, \quad B_5' = B_5 - \frac{a_5}{a_1}B_1 \tag{A.7}$$

substituting B_i with B_i',

$$\begin{aligned}\frac{F}{\rho u_m^2 D} &= A_1 \sin\theta + A_3 \sin 3\theta + \ ... \\ &+B_1' \cos\theta + B_3' \cos 3\theta + \ ...\end{aligned} \tag{A.8}$$

To determine the coefficients, the terms in Equation A.8 are matched to those in the nondimensional Morison equation A.4.

$$\begin{aligned}\frac{\pi}{4}\rho C_m \frac{2\pi D}{T u_m} &= A_1 + A_3 \frac{\sin 3\theta}{\sin\theta} + A_5 \frac{\sin\theta}{\sin\theta} \\ C_m &= \frac{2}{\pi^2}\frac{u_m T}{D}\big[A_1 + A_3 + A_5 + 2(A_3 + A_5)\cos 2\theta \\ &+2A_5 \cos 4\theta + \ ... \big]\end{aligned}$$

$$\begin{aligned}\frac{C_d}{2}|cos\theta|cos\theta &= B_1' - B_3' \frac{cos 3\theta}{|cos\theta|cos\theta} - \frac{B_5' \cos 5\theta}{|cos\theta|\cos\theta} + \ ... \\ C_d &= -2B_1' + \frac{2}{|cos\theta|}\big[2(B_3' - B_5') + 4(B_5' - B_3')\cos 2\theta \\ &-4B_5' \cos 4\theta + \ ... \big]\end{aligned} \tag{A.9}$$

(A.10)

assuming C_m and C_d are constant, this results in

$$C_m = \frac{2}{\pi^2}\frac{u_m T}{D} A_1 = \frac{4}{\pi}\frac{u_m}{D\omega} A_1 = \frac{2}{\pi^3}\frac{u_m T}{D}\int_0^{2\pi} \frac{F \sin n\theta}{\rho u_m^2 D} d\theta \tag{A.11}$$

$$C_d = -2B_1' = -2\frac{3\pi}{8}B_1 = -\frac{3}{4}\int_0^{2\pi} \frac{F \cos n\theta}{\rho u_m^2 D} d\theta \tag{A.12}$$

This assumes the coefficient is constant through the wave cycle, or that the A_1 and B_1 are an average over the cycle. If these does not lead to a good fit with the forces, one can look in to the remaining coefficients

$$\Delta R = A_3 \sin 3\theta + A_5 \sin 5\theta + B_2' \cos 3\theta + B_5' \cos 5\theta \tag{A.13}$$

A.1.1. Determining the added mass and damping by means of experiment

The hydrodynamic coefficients can be determined experimentally. In this case the system is subjected to a decay test or a forced oscillation in still water. The damping is in phase with the velocity and the added mass and the spring constant are in phase with the displacement and acceleration, see Equation A.14.

Decay test

In the decay test the system is excited, in still water. An example for heave, from [19],

$$(m+a)\cdot \ddot{z} + b\cdot \dot{z} + c\cdot z = 0 \tag{A.14}$$

In Equation A.14, z can be substituted with $z = \hat{z}e^{\lambda t}$

$$(m+a)\hat{z}\lambda^2 e^{\lambda t} + b\hat{z}\lambda e^{\lambda t} + c\hat{z}e^{\lambda t} = 0 \tag{A.15}$$

$$(m+a)\lambda^2 + b\lambda + c = 0 \tag{A.16}$$

$$\lambda = \frac{-b \pm \sqrt{b^2 - 4(m+a)\cdot c}}{2(m+a)} \tag{A.17}$$

$$b^2 = 4(m+a)c\,; \qquad b_{crit} = 2\sqrt{(m+a)\cdot c} \tag{A.18}$$

with $2\nu = \frac{b}{m+a}$, $\omega_0 = \sqrt{\frac{c}{m+a}}$, the non-dimensional damping ratio κ can be defined as

$$\kappa = \frac{b}{2\sqrt{(m+a)\cdot c}} = \frac{b}{2(m+a)\cdot\omega_0} = \frac{\nu}{\omega_0} \tag{A.19}$$

- $b < 2\sqrt{(m+a)c}$, the system is underdamped
- $b = 2\sqrt{(m+a)c}$, the system is critcally damped, $b = 2(m+a)\omega_0$
- $b > 2\sqrt{(m+a)c}$, the system is overdamped

for an overdamped system,
rewriting Equation A.17, this results in

$$\lambda_{1,2} = \frac{-2\nu \pm \sqrt{4\nu^2 - 4\omega_0^2}}{2} \tag{A.20}$$

$$= -\nu \pm \sqrt{\nu^2 - \omega_0^2} \tag{A.21}$$

$$= -\nu \pm i\sqrt{\omega_0^2 - \nu^2} = -\nu \pm i\sqrt{\omega_z^2} \tag{A.22}$$

thus

$$z = z_a e^{-\nu t}\left(a_1 e^{i\omega_z t} + a_2 e^{-i\omega_z t}\right) \tag{A.23}$$

or

$$z = z_a e^{-\nu t}\left(cos\omega_z t + \frac{\nu}{\omega_z}\sin\omega_z t\right) \tag{A.24}$$

the decay after one period T_z can be defined as

$$\nu Tz = \kappa\omega_0 T_z = \ln\frac{z(t)}{z(t+T_z)} \tag{A.25}$$

if $\nu^2 << \omega_0^2$, ν^2 can be neglected and $\omega_z \approx \omega_0$

$$\kappa = \frac{1}{2\pi}\ln\frac{z(t)}{z(t+T_z)} = b\cdot\frac{\omega_0}{2c} \tag{A.26}$$

Forced oscillation test

In a forced oscillation test the system is subjected to a forced constant oscillation. With this method the response to a given frequency can be determined. An example for heave will be given [19].

$$z(t) = z_a \sin\omega t \tag{A.27}$$

The heave forces can be measured by a transducer

$$F_z(t) = F_a \sin\left(\omega t + \epsilon_{F_z})\right) \tag{A.28}$$

$$(m+a)\cdot\ddot{z} + b\cdot\dot{z} + c\cdot z = F_a \sin\left(\omega t + \epsilon_{F_z}\right) \tag{A.29}$$

the added mass, damping determined as

$$a = \frac{c - \frac{F_a}{z_a}\cos\epsilon_{F_z}}{\omega^2} - m, \quad b = \frac{\frac{F_a}{z_a}\sin\epsilon_{F_z}}{\omega}, \tag{A.30}$$

with the forces and phase difference

$$F_a \sin\epsilon_{F_z} = \frac{2}{NT}\int_0^{NT} F(t)\cdot\cos\omega t\cdot dt$$

$$F_a \cos\epsilon_{F_z} = \frac{2}{NT}\int_0^{NT} F(t)\cdot\sin\omega t\cdot dt$$

$$\epsilon_{F_z} = \arctan\frac{F_a \sin\epsilon_{F_z}}{F_a \cos\epsilon_{F_z}}$$

B
Post-processing

The solver does not return the submerged area and volume as an output. It does however return the amount of submergence of the barrier surface. The algebra used in the post-processing can be found in Subsection B.1. The algorithm used to determine the submerged volume and the submerged projected area in heave and sway, can be found in subsection B.2.

B.1. Volume and area of a circle

The following provides more information on the algebra involved in the algorithm, [46]

$$
\begin{aligned}
D &= R \cdot 2 \\
h &= D/2 - r \\
V_{cirle} &= \pi \cdot D^2/4 \\
a &= 2\sqrt{h(D-h)} \\
s &= D/2 \cdot \theta \\
s &= D/2 \cdot \arcsin(\frac{a}{D}) \\
\theta &= s/R = 2\arccos(\frac{r}{D/2}) = 2\arcsin(\frac{a}{2 \cdot D/2}) \\
r &= D/2 \cdot \cos(1/2 \cdot \theta) \\
V_{yellow} &= D^2/4 \arccos\frac{D/2-h}{D/2} - (D/2-h) \cdot \sqrt{2 \cdot D/2 \cdot h - h^2}
\end{aligned}
$$

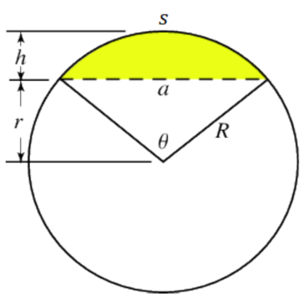

Figure B.1: Circle, [46]

B.2. Volume and area of the barrier

The submerged volume and area can be determined with the algorithm shown below. The base variables were defined in Table 4.3. Figure B.2 shows the notation and definitions.
To be able to differentiate between the water height on the left and right side of the barrier, the barrier is sliced vertically in two equal parts. Thus f becomes f_l and f_r etcetera. The algorithm is then executed for both the f_l and f_r. dh, the difference in water level on the left and the right side of the barrier is defined as, $dh = h_l - h_r$. The values for the whole barrier are then found by averaging the individual components, $V = (V_l + V_r)/2$.

$$
\begin{aligned}
s_{skirt} &= D/2 \cdot 2\arcsin(t_h/(D))\\
s_{b_{skirt}} &= D_b/2 \cdot 2\arcsin(t_h/(D_b))\\
h_{skirt} &= D/2 - D/2 \cdot \cos(1/2 \cdot 2\arcsin(\frac{t_h}{D}))\\
h_{b_{skirt}} &= D_b/2 - D_b/2 \cdot \cos(1/2 \cdot 2\arcsin(\frac{t_h}{D_b}))\\
V_{skirt} &= D^2/4\arccos\frac{D/2 - h_{skirt}}{D/2} - (D/2 - h_{skirt}) \cdot \sqrt{2 \cdot D/2 \cdot h_{skirt} - h_{skirt}{}^2}\\
V_{b_{skirt}} &= D_b^2/4\arccos\frac{D_b/2 - h_{b_{skirt}}}{D_b/2} - (D_b/2 - h_{b_{skirt}}) \cdot \sqrt{2 \cdot D_b/2 \cdot h_{b_{skirt}} - h_{b_{skirt}}{}^2}\\
V_{total} &= D^2/4 \cdot \pi - V_{skirt} + l_{sk} \cdot t_h + D_b^2/4 \cdot \pi - V_{b_{skirt}}\\
A_{total} &= D \cdot \pi - s_{skirt} + l_{sk} \cdot 2 - s_{b_{skirt}} + D_b \cdot \pi\\
s_{submerged} &= A_{total} \cdot f\\
s_{air} &= A_{total} \cdot (1 - f)
\end{aligned}
$$

if $\quad s_{air} - (D \cdot \pi - s_{skirt}) > D_b$

$$h = \frac{s_{air} - (D \cdot \pi - s_{skirt})}{2}$$

$$A_{heave} = D_b$$

$$A_{surge} = D_b + l_{sk} - h - h_{b_{skirt}}$$

$$V_{submerged} = t_h \cdot (l_{sk} - h) + D_b^2/4 \cdot \pi$$

else

$$s = (D \cdot \pi - s_{skirt}) - s_{air}$$

$$\theta = \frac{s + s_{skirt}}{D/2}$$

$$h = D/2 - D/2 \cdot \cos(1/2 \cdot \theta)$$

$$a = 2\sqrt{h(D - h)}$$

$$V_w = D^2/4\arccos\frac{D/2 - h}{D/2} - (D/2 - h) \cdot \sqrt{2 \cdot D/2 \cdot h - h^2}$$

if $\quad (h == D)$

$$A_{heave} = D$$

else

$$A_{heave} = a$$

end

$$A_{surge} = D_b + l_{sk} + h - h_{skirt} - h_{b_{skirt}}$$

$$V_{submerged} = t_h \cdot l_{sk} + D_b^2/4 \cdot \pi + V_w - V_{b_{skirt}} - V_{skirt}$$

end

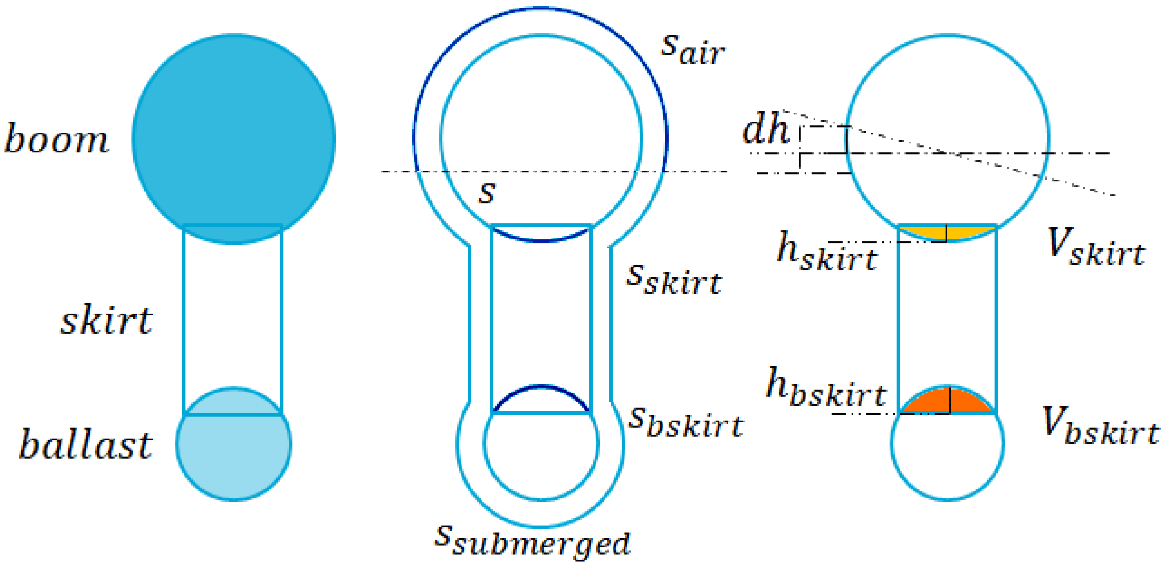

Figure B.2: Overview of the different notations used in post processing

C

Hydrodynamic coefficients results

The results can be found in this appendix. The numerical results from the simulations were fitted to the Morison equation to determine the hydrodynamic coefficients. An overview is given in Table C.1 to Table C.3 and Figure C.1 to C.3. Figure **??** to **??** show the result for the 2 parameter solution, and could provide more insight on the dominating variables per case. The location parameters buz, buy, are displayed relative to mean location over the displayed range. This was done to ensure that the all the results are easy to compare.

Table C.1: Hydrodynamic coefficients, 2 parameter fit

λ	H	motion	KR	Cmy	Cdy	KCy	Cmz	Cdz	KCz	R_{mse_y}	R_{mse_z}
14.3	0.10	fixed	0.04	-10.9	-1.6	1.4	13.5	33.1	1.4	3.2	2.8
14.3	0.10	heave	0.04	-	-	-	1.0	-0.3	1.6	0.8	1.2
14.3	0.10	sway	0.04	-2.4	1.4	1.6	-	-	-	1.0	6.7
14.3	0.10	dof-z	0.04	-11.3	-0.8	1.4	0.3	0.2	1.4	1.2	2.4
14.3	0.10	dof-y	0.04	0.5	0.8	1.4	8.3	21.0	1.4	0.6	1.8
14.3	0.10	dof-yz	0.04	0.2	0.8	1.4	-0.1	0.2	1.4	0.6	2.5
17.3	0.12	fixed	0.03	-9.8	0.8	1.8	1.9	-5.3	1.8	6.1	3.8
17.3	0.12	heave	0.03	-	-	-	0.9	-0.3	1.9	0.5	1.2
17.3	0.12	sway	0.03	-1.4	-0.2	1.9	-	-	-	2.1	6.8
17.3	0.12	dof-z	0.03	-11.1	1.9	1.9	0.4	0.1	1.9	1.4	2.4
17.3	0.12	dof-y	0.03	0.3	0.4	1.9	4.5	3.6	1.9	0.1	3.5
17.3	0.12	dof-yz	0.03	0.0	0.5	1.9	0.5	0.1	1.9	0.1	2.5
17.3	0.08	fixed	0.03	-9.8	0.1	1.3	16.1	37.2	1.3	1.5	2.2
17.3	0.08	heave	0.03	-	-	-	0.9	-0.2	1.3	0.6	1.3
17.3	0.08	sway	0.03	-0.9	1.4	1.3	-	-	-	0.8	4.6
17.3	0.08	dof-z	0.03	-10.4	0.6	1.3	0.4	0.1	1.3	0.5	2.4
17.3	0.08	dof-y	0.03	0.3	0.2	1.3	13.7	32.0	1.3	0.6	2.2
17.3	0.08	dof-yz	0.03	0.1	0.1	1.3	1.0	0.0	1.3	0.6	2.5
17.3	0.10	fixed	0.03	-9.9	0.1	1.5	12.1	23.7	1.5	2.1	2.9
17.3	0.10	heave	0.03	-	-	-	0.8	-0.2	1.6	0.4	1.1
17.3	0.10	sway	0.03	-1.3	2.0	1.6	-	-	-	1.3	5.6
17.3	0.10	dof-z	0.03	-10.7	1.4	1.5	0.6	0.1	1.5	0.8	2.4
17.3	0.10	dof-y	0.03	0.3	0.6	1.5	11.1	22.8	1.5	0.6	2.6
17.3	0.10	dof-yz	0.03	0.1	0.6	1.5	0.3	0.1	1.5	0.6	2.5
20.7	0.10	fixed	0.02	-8.3	2.0	1.7	13.0	20.2	1.7	2.4	2.8
20.7	0.10	heave	0.02	-	-	-	0.8	-0.1	1.6	0.6	1.2
20.7	0.10	sway	0.02	-1.2	2.6	1.6	-	-	-	0.7	4.7
20.7	0.10	dof-z	0.02	-10.5	0.7	1.7	0.4	0.1	1.7	1.1	2.4
20.7	0.10	dof-y	0.02	0.2	0.3	1.7	27.7	52.6	1.7	0.6	5.7
20.7	0.10	dof-yz	0.02	-0.1	0.3	1.7	0.8	0.1	1.7	0.6	2.5

Table C.2: Hydrodynamic coefficients, 2 parameter fit with correction

λ	H	motion	KR	Cmy	Cdy	KCy	Cmz	Cdz	KCz	R_{mse_y}	R_{mse_z}	$(V\rho - m)\cdot g$
14.3	0.10	fixed	0.04	-10.9	-1.6	1.4	13.5	33.1	1.4	3.2	2.8	-
14.3	0.10	heave	0.04	-	-	-	1.0	-0.3	1.6	0.8	1.2	-
14.3	0.10	sway	0.04	-2.4	1.4	1.6	-	-	-	1.0	6.7	-
14.3	0.10	dof-z	0.04	-11.3	-0.8	1.4	0.0	0.1	1.4	1.2	0.1	2.4
14.3	0.10	dof-y	0.04	0.5	0.8	1.4	8.3	21.0	1.4	0.6	1.8	-
14.3	0.10	dof-yz	0.04	0.2	0.8	1.4	-0.2	0.1	1.4	0.6	0.0	2.5
17.3	0.12	fixed	0.03	-9.8	0.8	1.8	1.9	-5.3	1.8	6.1	3.8	-
17.3	0.12	heave	0.03	-	-	-	0.9	-0.3	1.9	0.5	1.2	-
17.3	0.12	sway	0.03	-1.4	-0.2	1.9	-	-	-	2.1	6.8	-
17.3	0.12	dof-z	0.03	-11.1	1.9	1.9	0.2	0.1	1.9	1.4	0.1	2.4
17.3	0.12	dof-y	0.03	0.3	0.4	1.9	4.5	3.6	1.9	0.1	3.5	-
17.3	0.12	dof-yz	0.03	0.0	0.5	1.9	0.1	0.0	1.9	0.1	0.1	2.5
17.3	0.08	fixed	0.03	-9.8	0.1	1.3	16.1	37.2	1.3	1.5	2.2	-
17.3	0.08	heave	0.03	-	-	-	0.9	-0.2	1.3	0.6	1.3	-
17.3	0.08	sway	0.03	-0.9	1.4	1.3	-	-	-	0.8	4.6	-
17.3	0.08	dof-z	0.03	-10.4	0.6	1.3	0.1	0.1	1.3	0.5	0.0	2.4
17.3	0.08	dof-y	0.03	0.3	0.2	1.3	13.7	32.0	1.3	0.6	2.2	-
17.3	0.08	dof-yz	0.03	0.1	0.1	1.3	0.1	0.1	1.3	0.6	0.0	2.5
17.3	0.10	fixed	0.03	-9.9	0.1	1.5	12.1	23.7	1.5	2.1	2.9	-
17.3	0.10	heave	0.03	-	-	-	0.8	-0.2	1.6	0.4	1.1	-
17.3	0.10	sway	0.03	-1.3	2.0	1.6	-	-	-	1.3	5.6	-
17.3	0.10	dof-z	0.03	-10.7	1.4	1.5	0.1	0.1	1.5	0.8	0.0	2.4
17.3	0.10	dof-y	0.03	0.3	0.6	1.5	11.1	22.8	1.5	0.6	2.6	-
17.3	0.10	dof-yz	0.03	0.1	0.6	1.5	0.1	0.0	1.5	0.6	0.0	2.5
20.7	0.10	fixed	0.02	-8.3	2.0	1.7	13.0	20.2	1.7	2.4	2.8	-
20.7	0.10	heave	0.02	-	-	-	0.8	-0.1	1.6	0.6	1.2	-
20.7	0.10	sway	0.02	-1.2	2.6	1.6	-	-	-	0.7	4.7	-
20.7	0.10	dof-z	0.02	-10.5	0.7	1.7	0.1	0.1	1.7	1.1	0.0	2.4
20.7	0.10	dof-y	0.02	0.2	0.3	1.7	27.7	52.6	1.7	0.6	5.7	-
20.7	0.10	dof-yz	0.02	-0.1	0.3	1.7	0.2	0.0	1.7	0.6	0.1	2.5

Table C.3: Hydrodynamic coefficients, 3 parameter fit

λ	H	motion	KR	Cmy	Cdy	KCy	Cmz	Cdz	KCz	R_{mse_y}	R_{mse_z}	f_{3_y}	f_{3_z}
14.3	0.10	fixed	0.04	-10.9	-1.5	1.4	5.6	11.6	1.4	3.2	2.1	-0.5	-2.6
14.3	0.10	heave	0.04	-	-	-	0.8	-0.2	1.6	0.6	0.7	-	-1.0
14.3	0.10	sway	0.04	-2.4	1.4	1.6	-	-	-	1.0	2.9	0.2	
14.3	0.10	dof-z	0.04	-11.3	-0.8	1.4	0.0	0.1	1.4	1.2	0.1	0.2	-2.4
14.3	0.10	dof-y	0.04	0.5	0.6	1.4	3.5	8.0	1.4	0.1	1.4	0.6	-1.6
14.3	0.10	dof-yz	0.04	0.2	0.7	1.4	-0.2	0.1	1.4	0.1	0.0	0.6	-2.5
17.3	0.12	fixed	0.03	-9.8	0.8	1.8	-1.9	-11.1	1.8	6.1	2.2	0.0	-3.7
17.3	0.12	heave	0.03	-	-	-	0.8	-0.3	1.9	0.4	1.0	-	-0.6
17.3	0.12	sway	0.03	-1.5	-0.2	1.9	-	-	-	1.4	2.9	1.6	
17.3	0.12	dof-z	0.03	-11.1	1.9	1.9	0.2	0.1	1.9	1.4	0.1	0.2	-2.4
17.3	0.12	dof-y	0.03	0.3	0.4	1.9	0.0	-4.4	1.9	0.1	2.2	0.0	-3.2
17.3	0.12	dof-yz	0.03	0.0	0.5	1.9	0.1	0.0	1.9	0.1	0.1	0.0	-2.5
17.3	0.08	fixed	0.03	-9.8	0.1	1.3	3.7	5.0	1.3	1.5	1.0	0.2	-2.9
17.3	0.08	heave	0.03	-	-	-	0.6	-0.1	1.3	0.4	0.4	-	-1.4
17.3	0.08	sway	0.03	-0.9	1.4	1.3	-	-	-	0.4	1.5	0.7	
17.3	0.08	dof-z	0.03	-10.5	0.6	1.3	0.1	0.1	1.3	0.5	0.0	-0.2	-2.4
17.3	0.08	dof-y	0.03	0.4	0.1	1.3	1.4	0.1	1.3	0.0	1.0	0.6	-2.9
17.3	0.08	dof-yz	0.03	0.1	0.0	1.3	0.1	0.1	1.3	0.0	0.0	0.6	-2.5
17.3	0.10	fixed	0.03	-9.9	0.1	1.5	1.9	-0.9	1.5	2.1	1.9	0.2	-2.9
17.3	0.10	heave	0.03	-	-	-	0.7	-0.2	1.6	0.3	0.6	-	-0.9
17.3	0.10	sway	0.03	-1.3	2.0	1.6	-	-	-	1.2	2.2	-0.4	
17.3	0.10	dof-z	0.03	-10.7	1.4	1.5	0.1	0.1	1.5	0.8	0.0	0.1	-2.4
17.3	0.10	dof-y	0.03	0.3	0.5	1.5	2.4	1.9	1.5	0.1	1.7	0.6	-2.6
17.3	0.10	dof-yz	0.03	0.1	0.5	1.5	0.1	0.0	1.5	0.1	0.0	0.6	-2.5
20.7	0.10	fixed	0.02	-8.3	2.0	1.7	3.4	1.8	1.7	2.4	1.7	0.4	-2.7
20.7	0.10	heave	0.02	-	-	-	0.5	-0.2	1.6	0.3	0.5	-	-1.2
20.7	0.10	sway	0.02	-1.2	2.6	1.6	-	-	-	0.5	1.6	0.5	
20.7	0.10	dof-z	0.02	-10.5	0.7	1.7	0.1	0.1	1.7	0.9	0.0	-0.6	-2.4
20.7	0.10	dof-y	0.02	0.2	0.3	1.7	7.8	13.4	1.7	0.1	3.9	0.6	-5.2
20.7	0.10	dof-yz	0.02	-0.1	0.3	1.7	0.2	0.0	1.7	0.1	0.1	0.6	-2.5

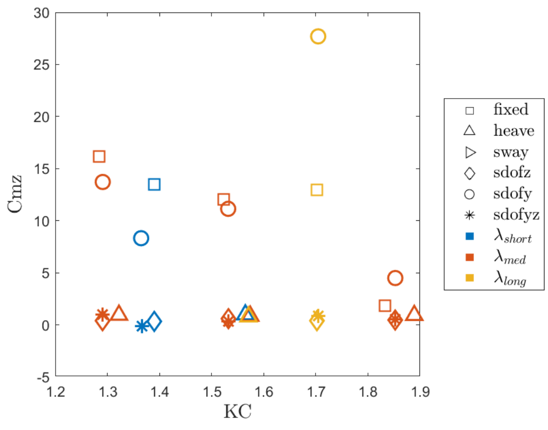

(a) Cmz, 2 parameters

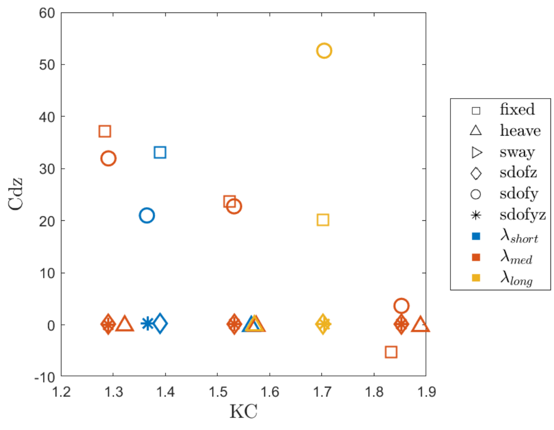

(b) Cdz, 2 parameters

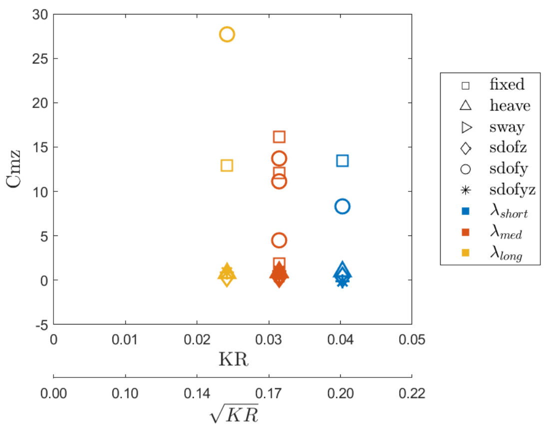

(c) Cmz, 2 parameters

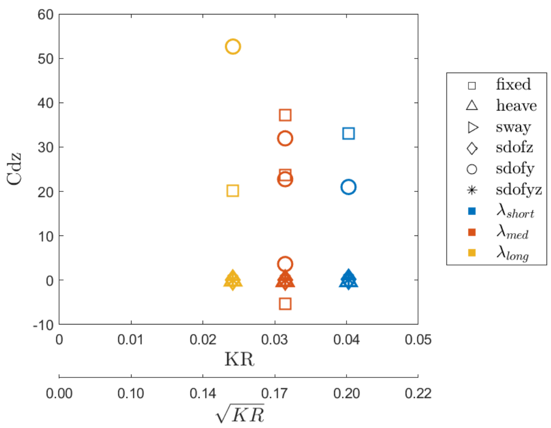

(d) Cdz, 2 parameters

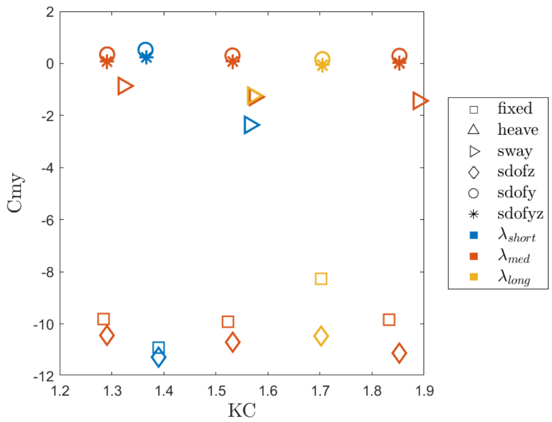

(e) Cmy, 2 parameters

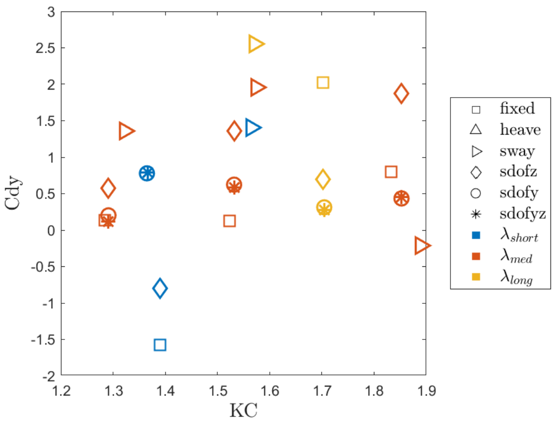

(f) Cdy, 2 parameters

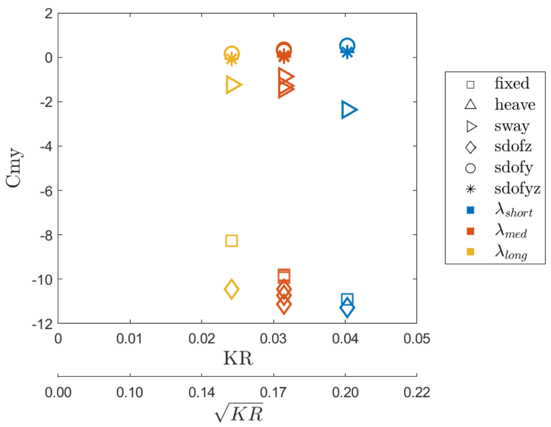

(g) Cmy, 2 parameters

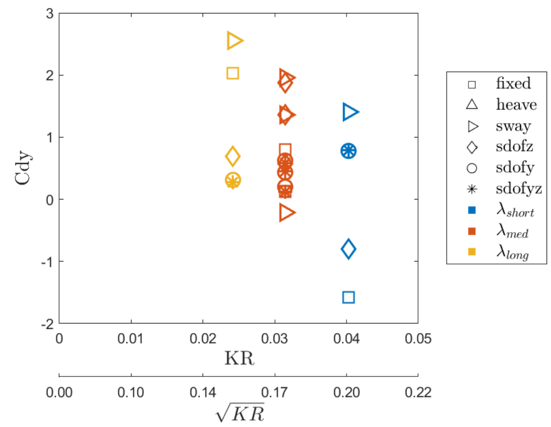

(h) Cdy, 2 parameters

Figure C.1: Hydrodynamic coefficients with 2 parameter fit

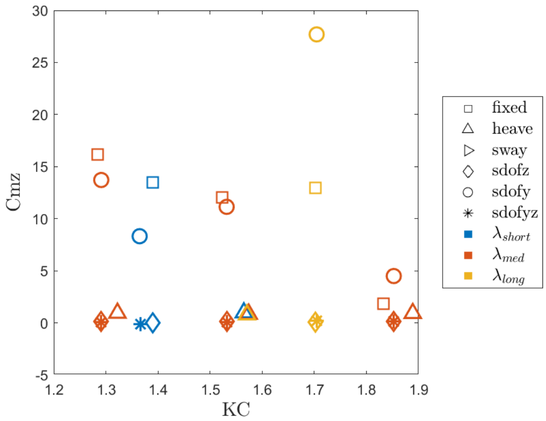

(a) Cmz, 2 parameters & correction

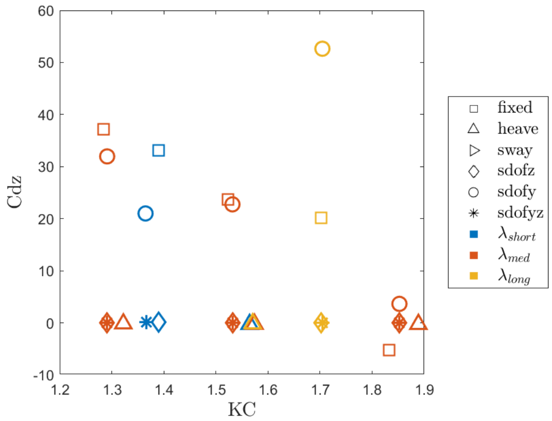

(b) Cdz, 2 parameters & correction

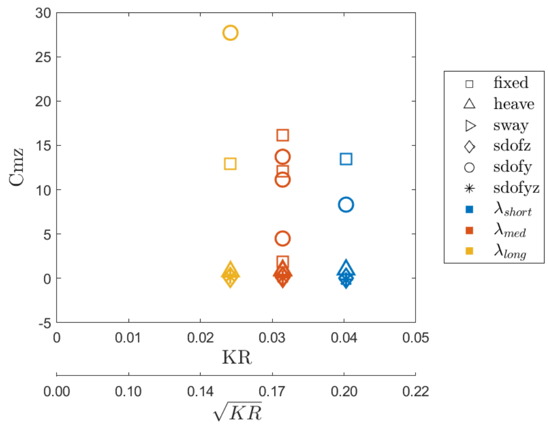

(c) Cmz, 2 parameters & correction

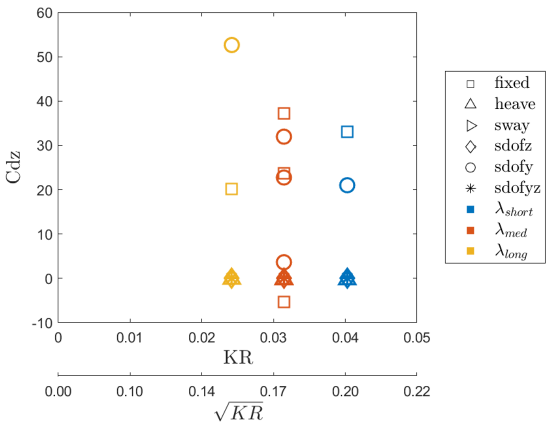

(d) Cdz, 2 parameters & correction

Figure C.2: Hydrodynamic coefficients with 2 parameter fit with correction for z

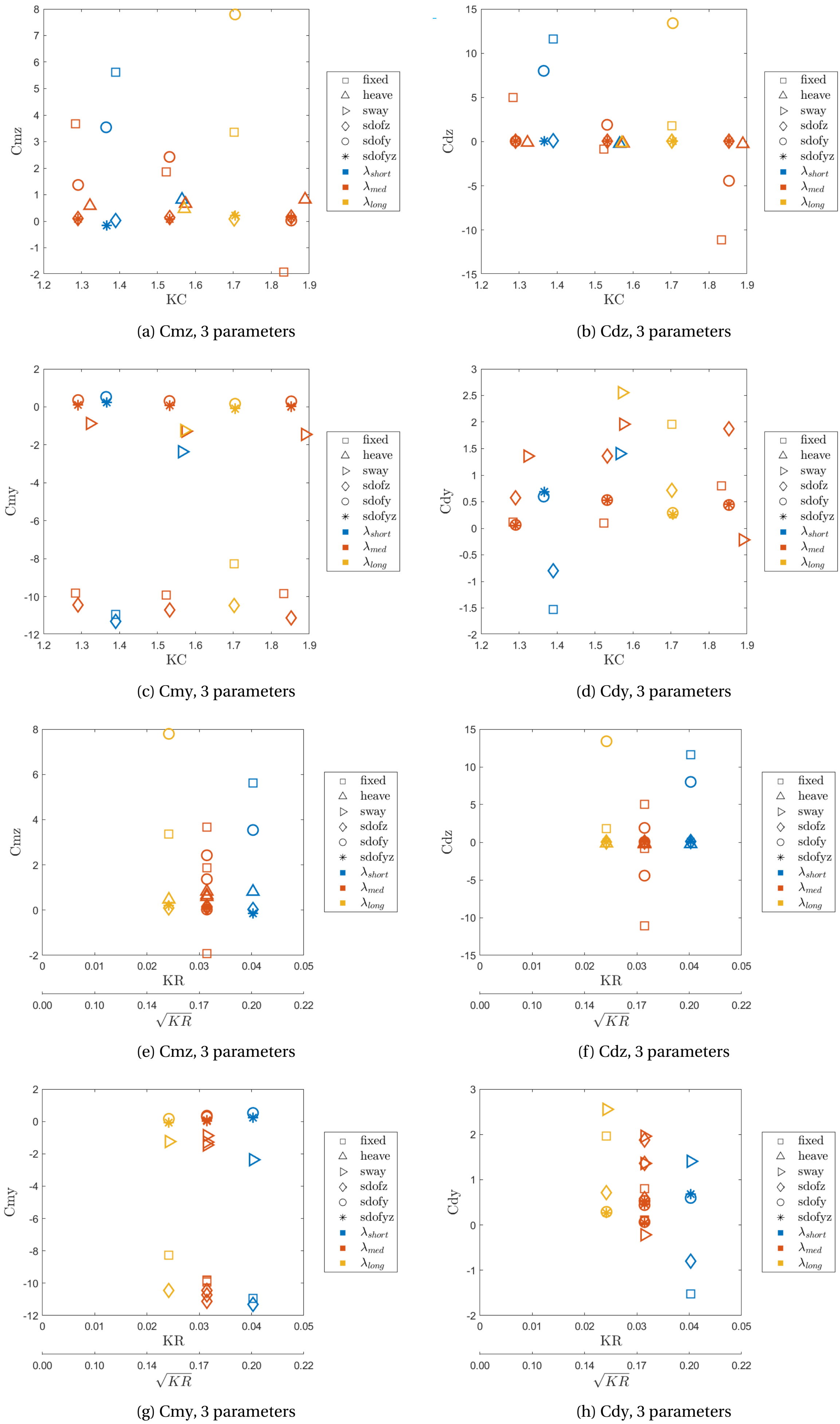

(a) Cmz, 3 parameters

(b) Cdz, 3 parameters

(c) Cmy, 3 parameters

(d) Cdy, 3 parameters

(e) Cmz, 3 parameters

(f) Cdz, 3 parameters

(g) Cmy, 3 parameters

(h) Cdy, 3 parameters

Figure C.3: Hydrodynamic coefficients with 3 parameter fit

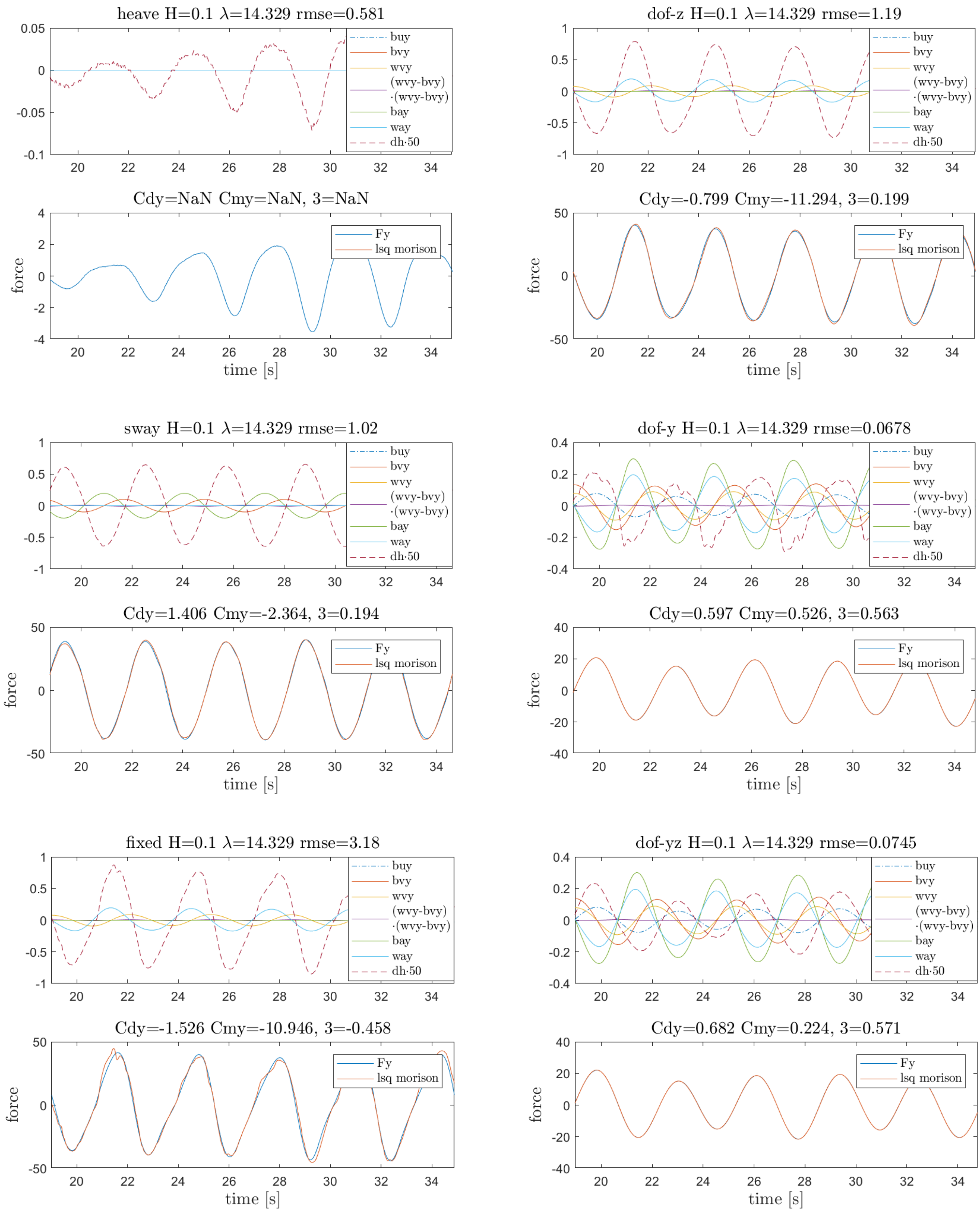

Figure C.4: Fit of the hydrodynamic coefficients in the y direction, $\lambda = 14.329$, with 3 parameters

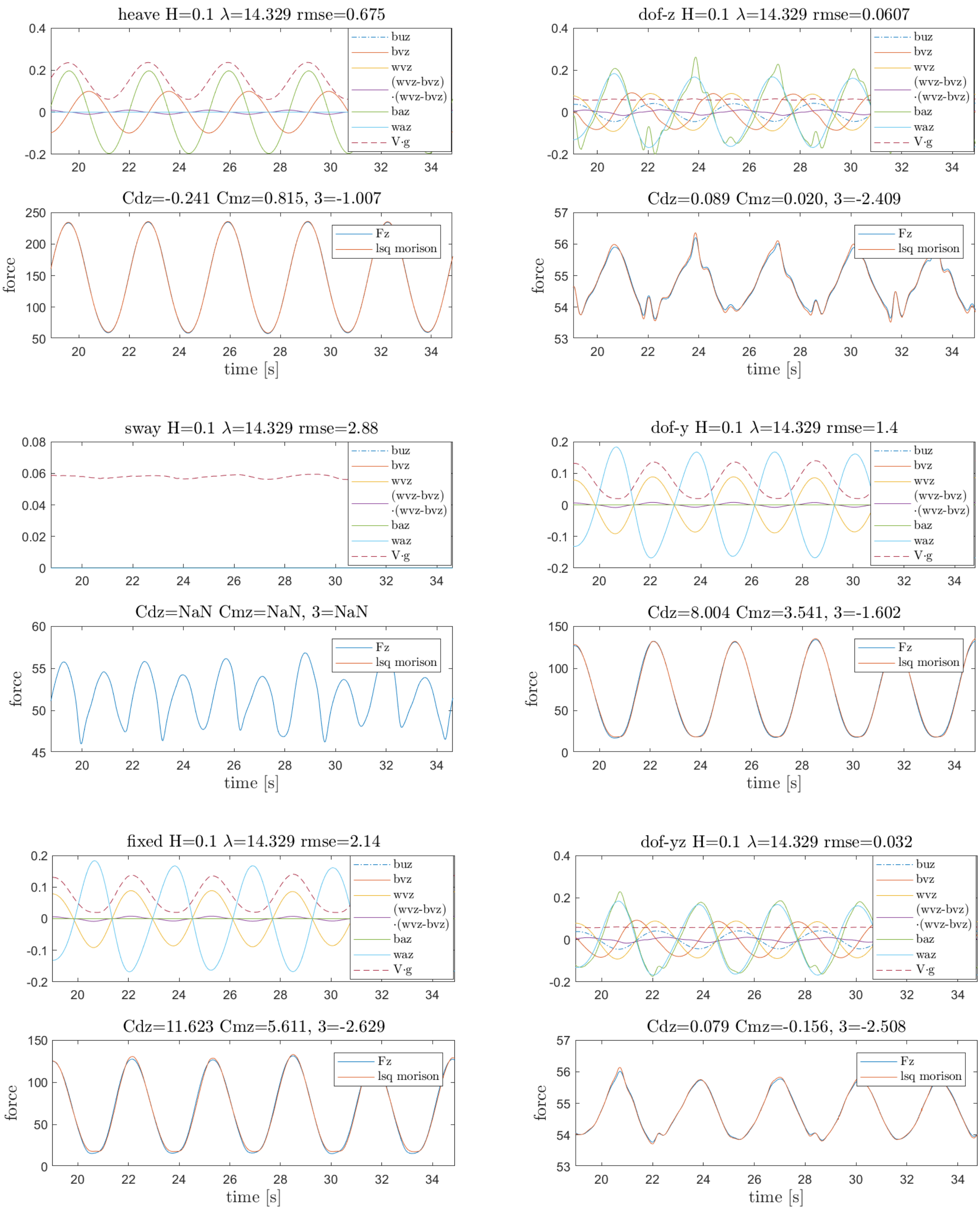

Figure C.5: Fit of the hydrodynamic coefficients in the z direction, $\lambda = 14.329$, with 3 parameters

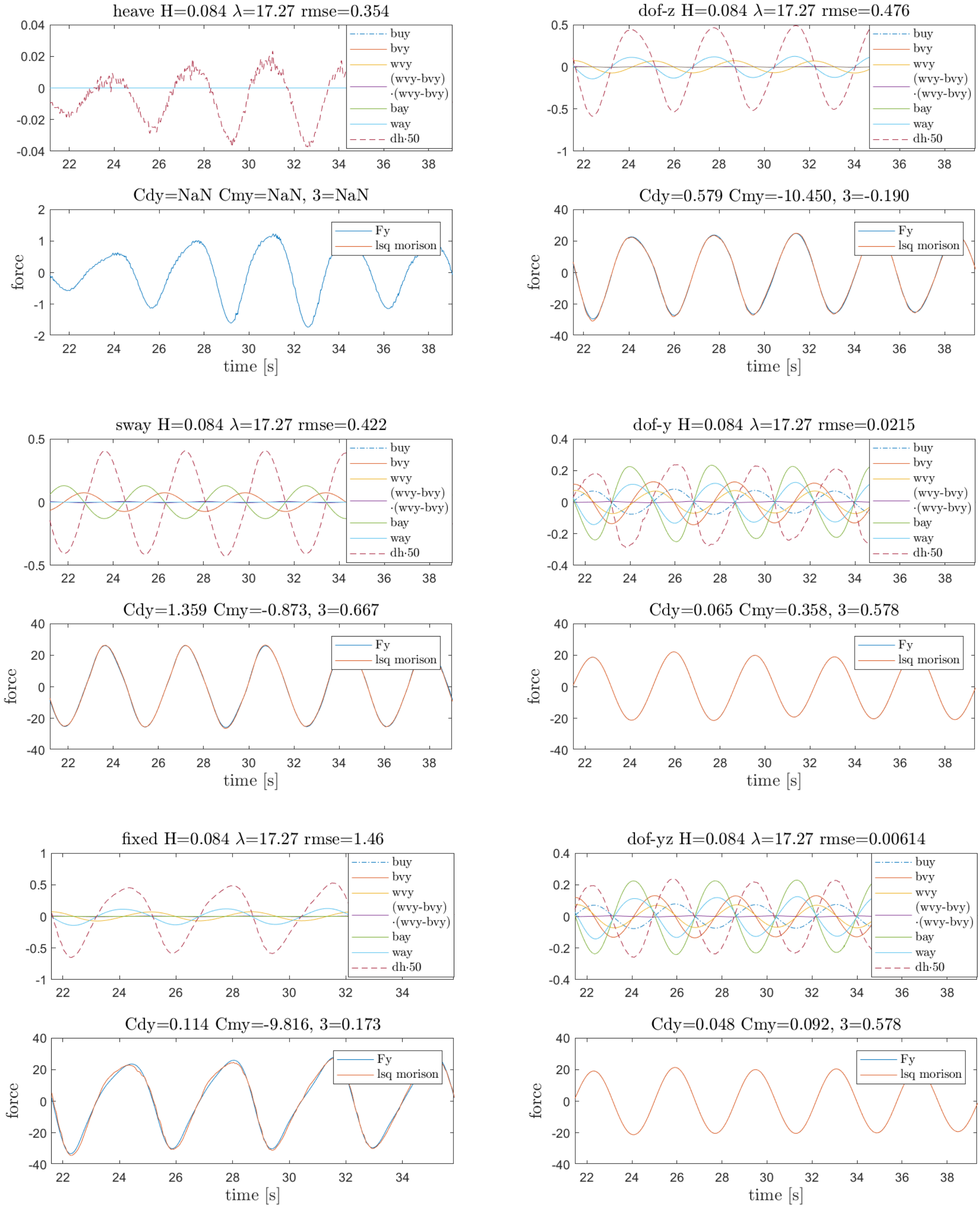

Figure C.6: Fit of the hydrodynamic coefficients in the y direction, $\lambda = 17.27$, $H = 0.084$, with 3 parameters

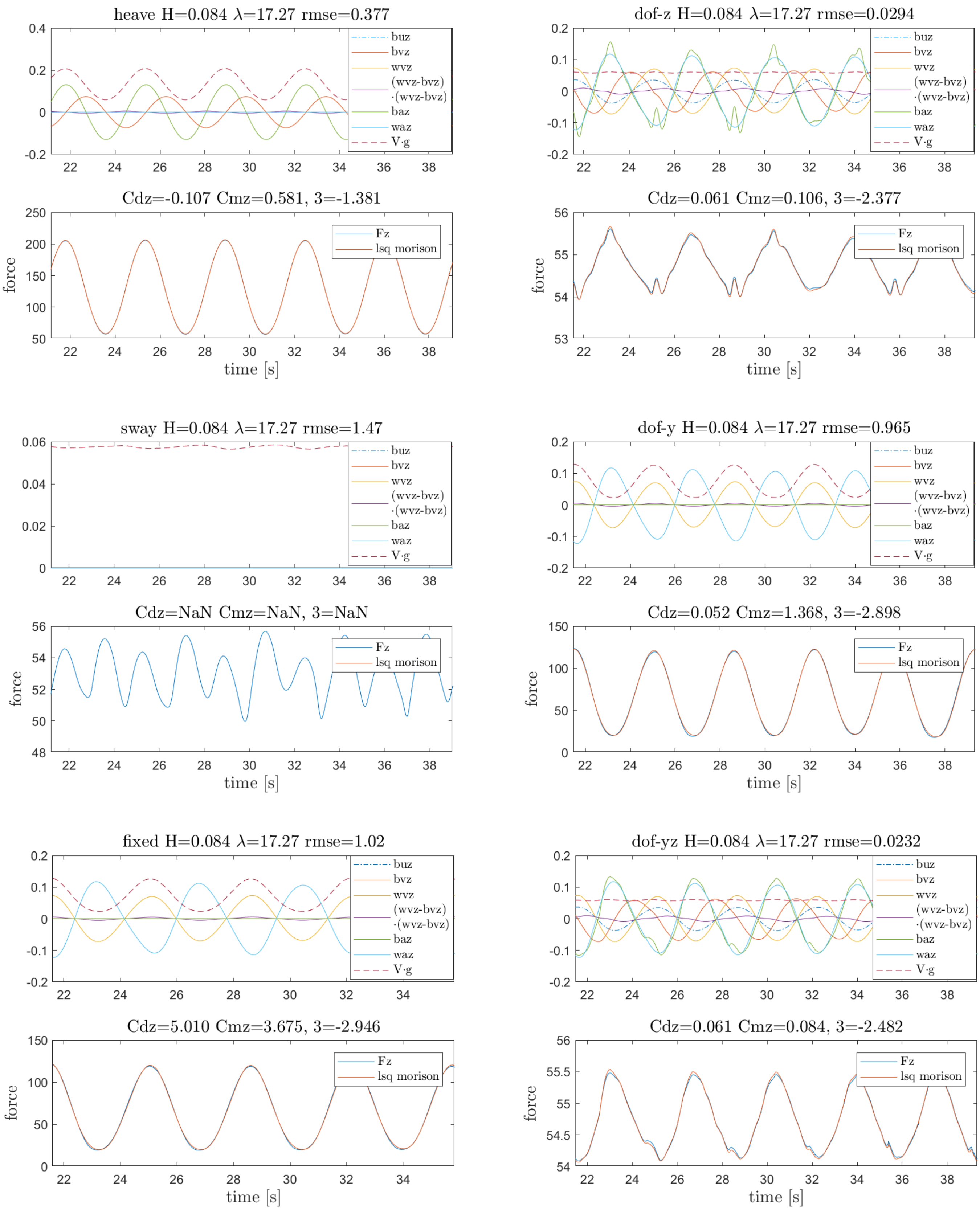

Figure C.7: Fit of the hydrodynamic coefficients in the z direction, $\lambda = 17.27$, $H = 0.084$, with 3 parameters

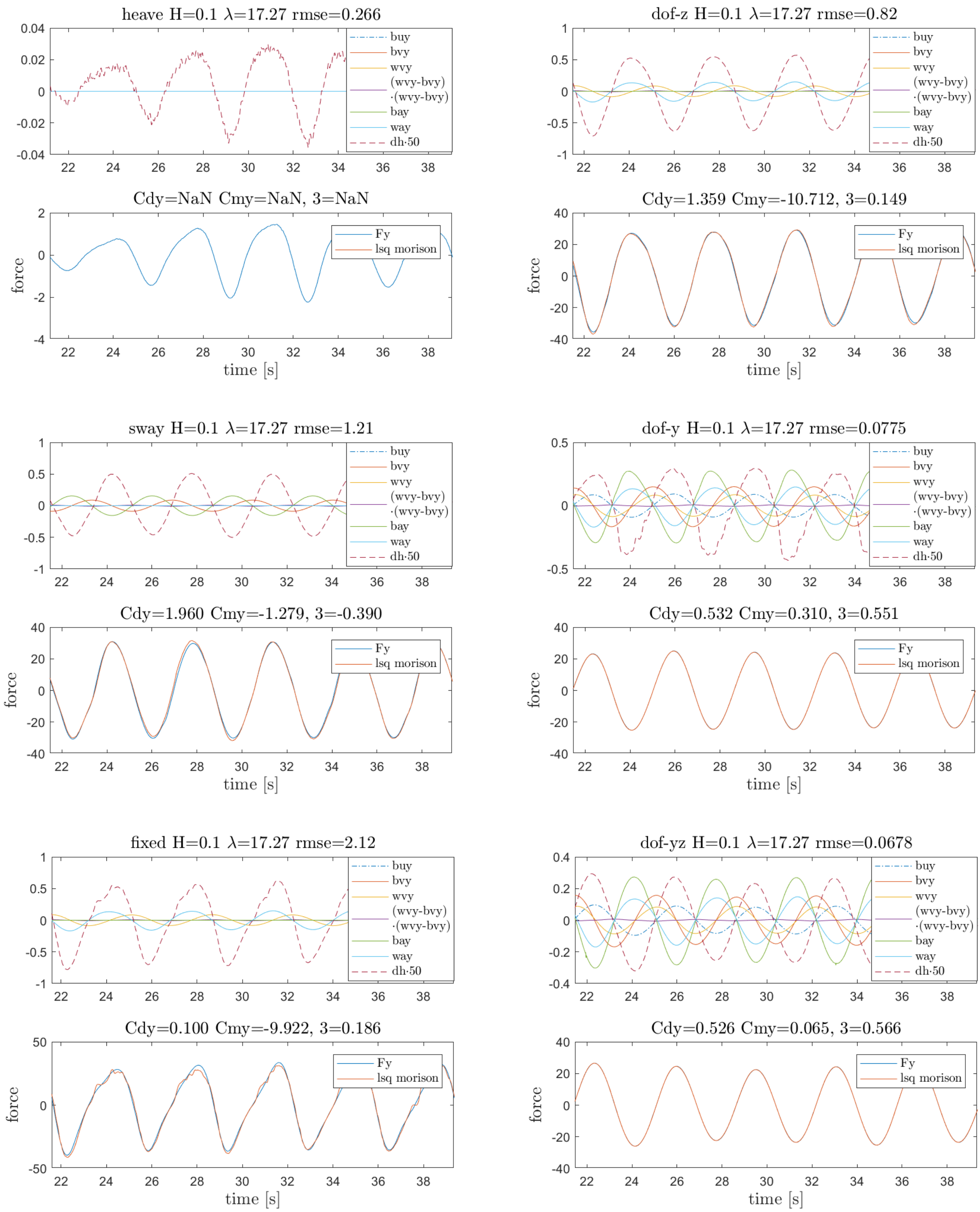

Figure C.8: Fit of the hydrodynamic coefficients in the y direction, $\lambda = 17.27$, $H = 0.1$, with 3 parameters

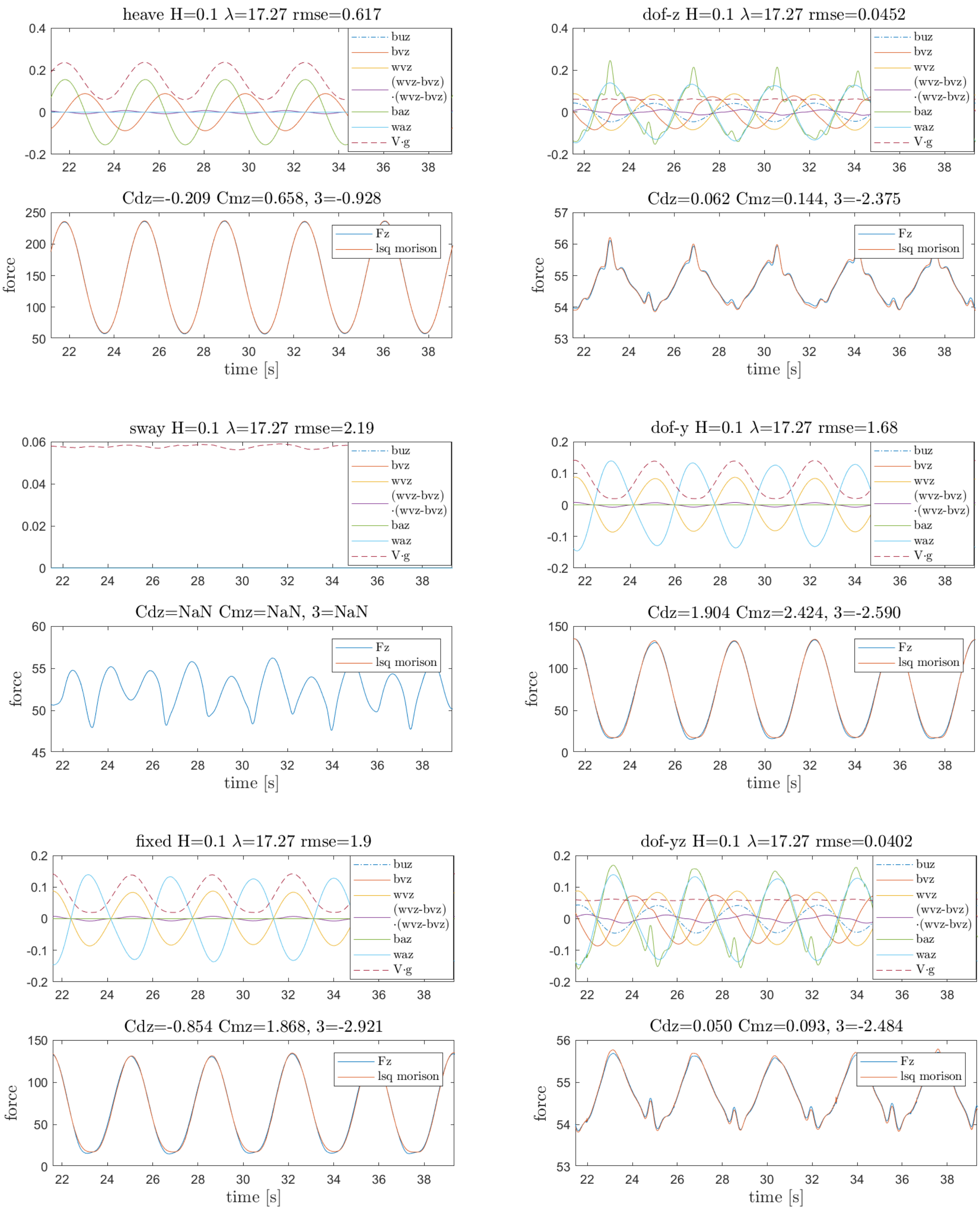

Figure C.9: Fit of the hydrodynamic coefficients in the z direction, $\lambda = 17.27$, $H = 0.1$, with 3 parameters

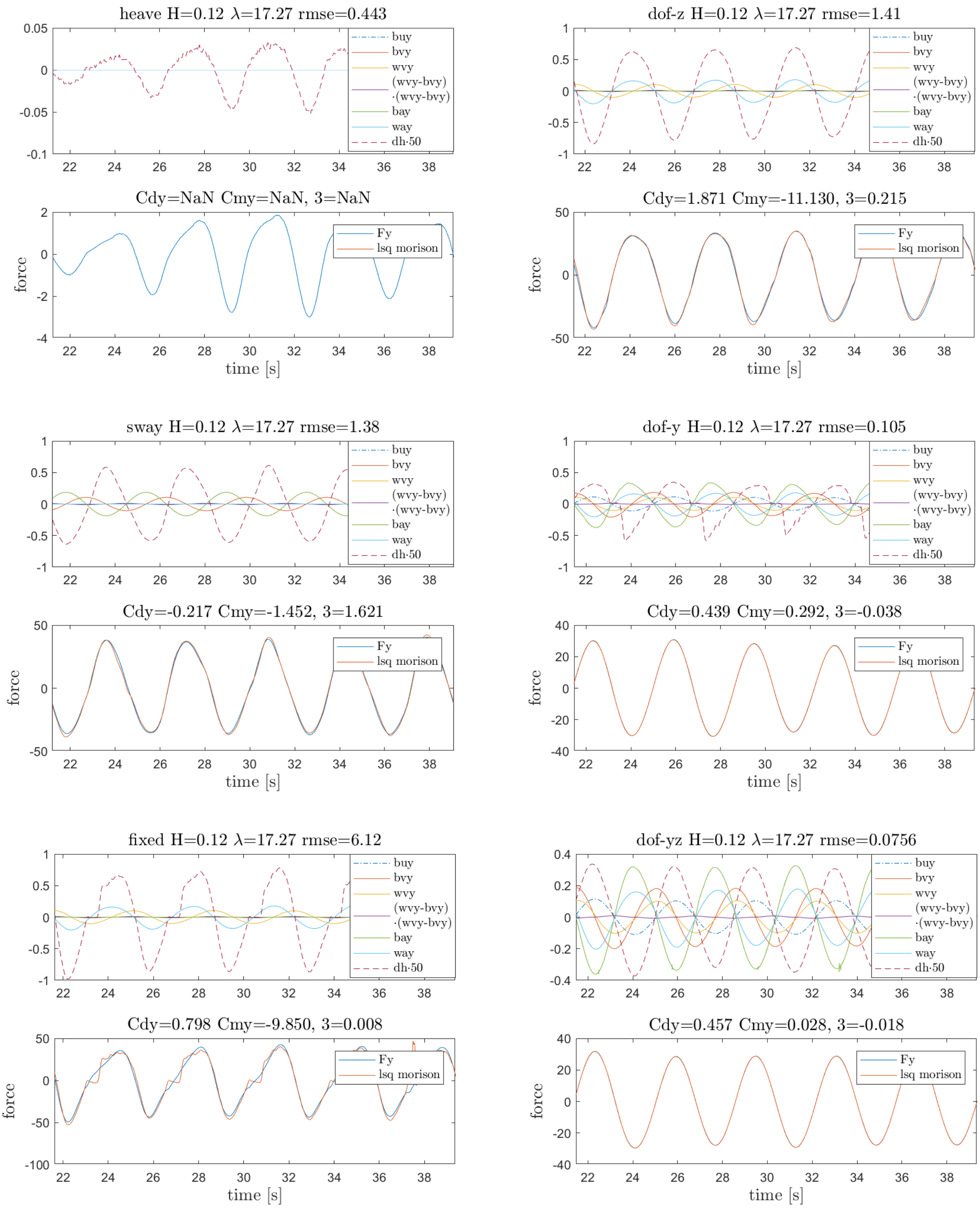

Figure C.10: Fit of the hydrodynamic coefficients in the y direction,$\lambda = 17.27$, $H = 0.12$, with 3 parameters

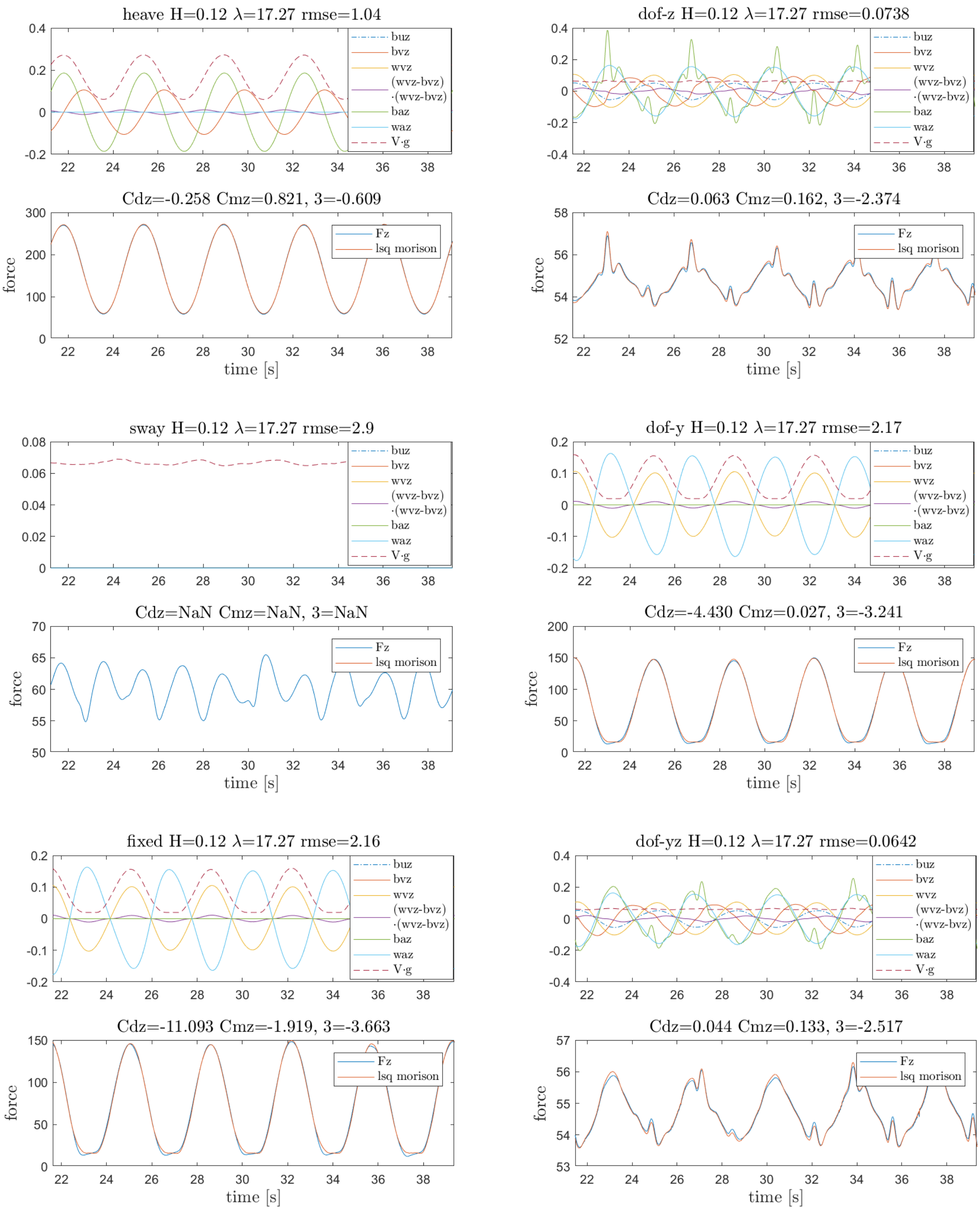

Figure C.11: Fit of the hydrodynamic coefficients in the z direction, $\lambda = 17.27$, $H = 0.12$, with 3 parameters

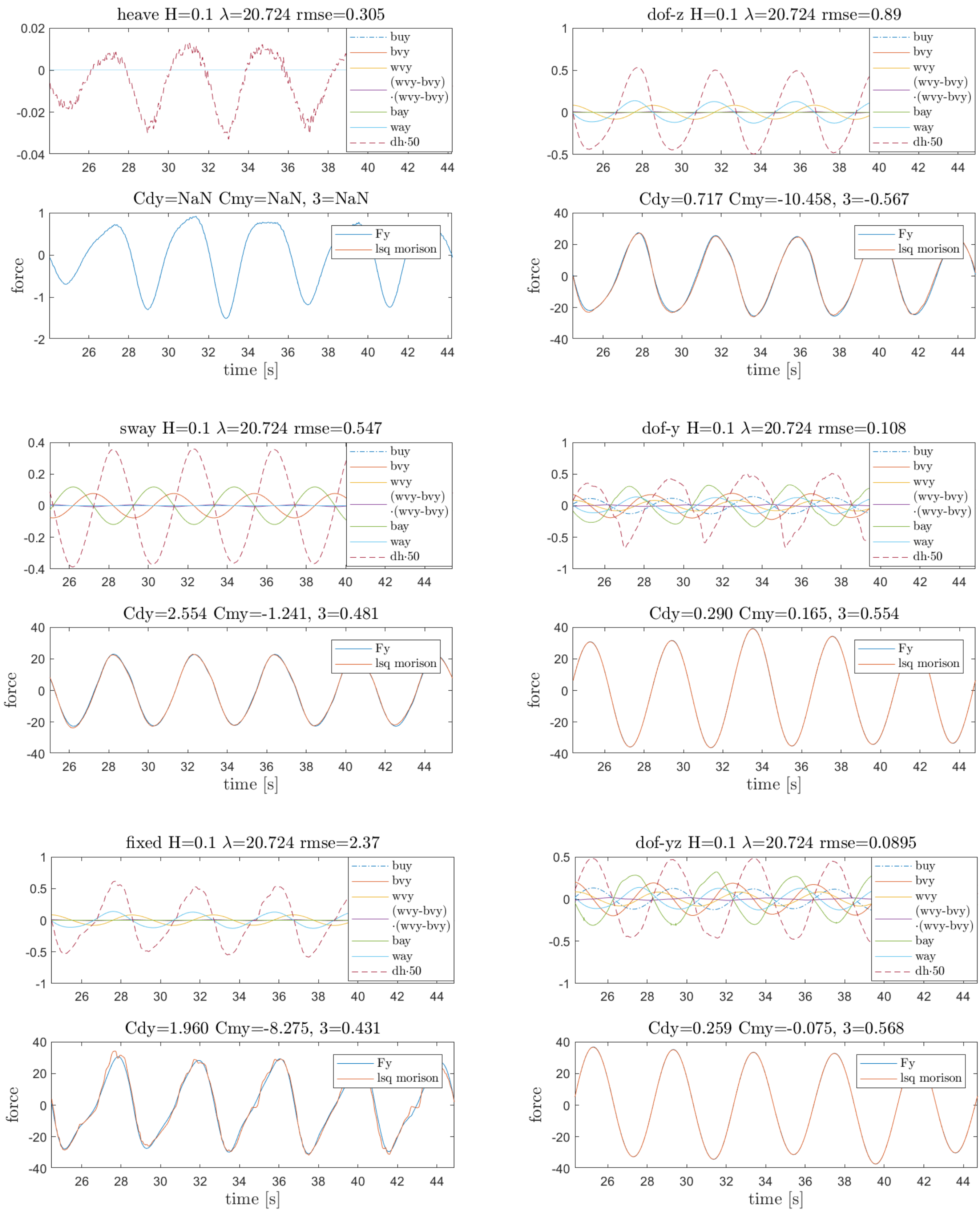

Figure C.12: Fit of the hydrodynamic coefficients in the y direction, $\lambda = 20.724$, with 3 parameters

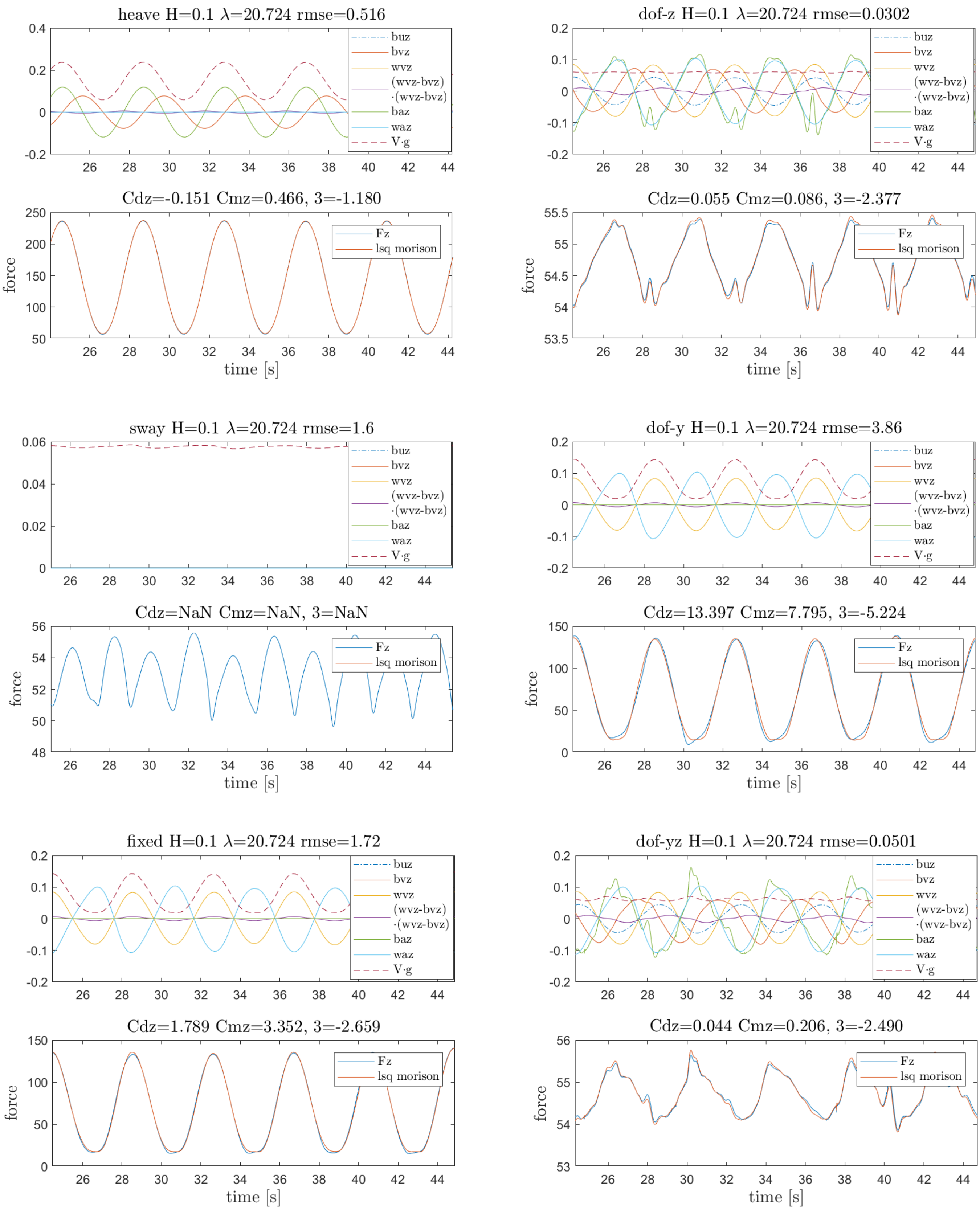

Figure C.13: Fit of the hydrodynamic coefficients in the z direction, $\lambda = 20.724$, with 3 parameters

D

Details

D.1. Mesh around the barrier

Figure D.1 shows a close up of the mesh around the barrier. The mesh resolution around the barrier was kept in line with the mesh resolution in the free surface.

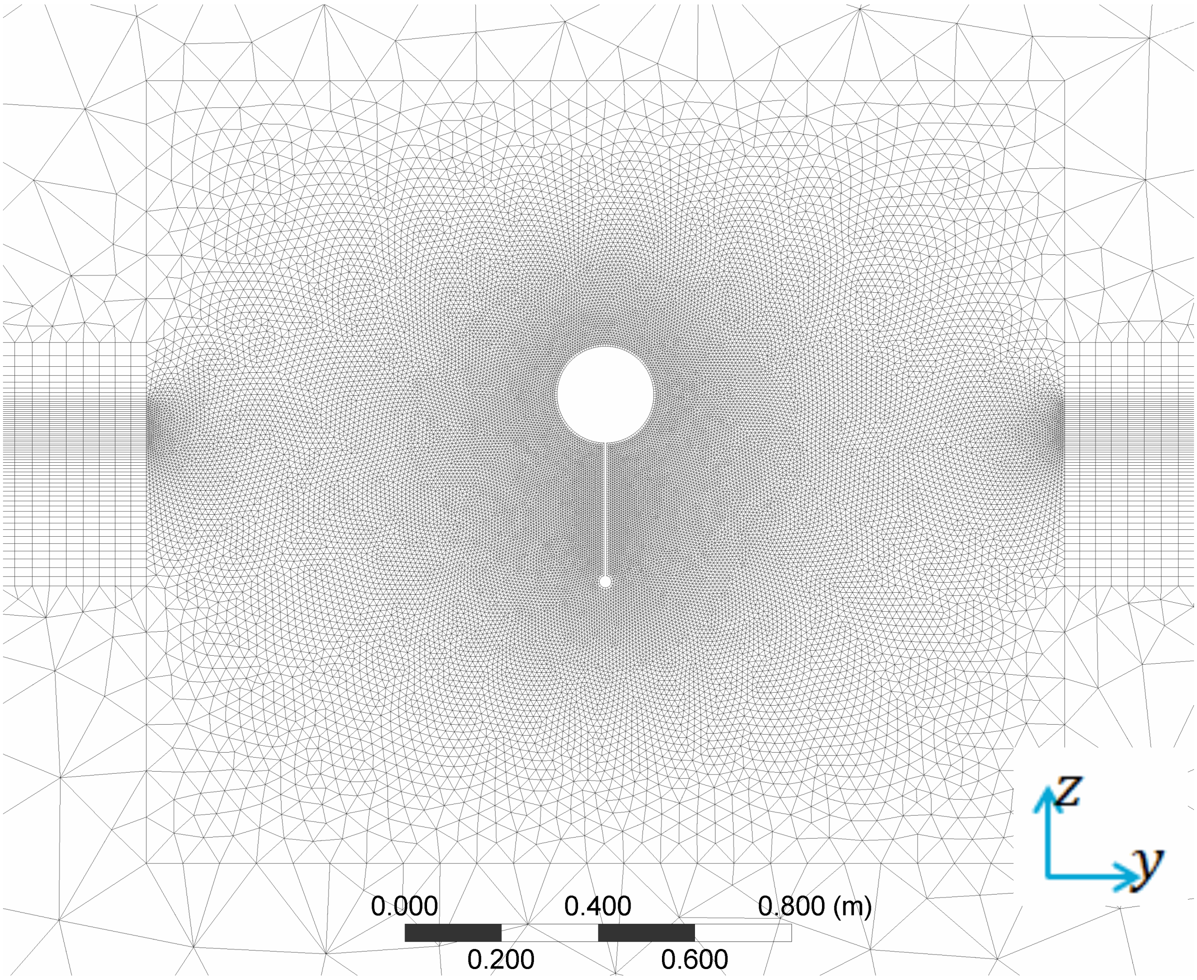

Figure D.1: Close up of the domain around the barrier

D.2. Fluent settings

D.2.1. Stabilisation

Contrary to what might be expected, the simulation seems more unstable with low amplitude waves. Instabilities form in the region closest to the ballast. Similar instabilities were seen in the coupled CFD-FEM simulations. The cause of these instabilities is unknown. With the following combination of dynamic mesh settings, all cases stabilise fairly well. Higher stabilisation factors will lead to slower convergence, lower stabilisation factors lead to slower convergence as well.

The relaxation fo the displacements is done by Fluent with the following equation

Table D.1: Moving dynamic mesh settings in fluent

parameter	value
Stabilisation, coefficient based	0.55
Motion relaxation factor	0.9

$$x_k = \omega(x_{computed,k} + (1-\omega)x_{k-1})$$

here x_k represents the node position at iteration k, $x_{computed,k}$ represents the computed node position based on the flow field and ω represents the relaxation factor [12].

D.2.2. UDF

The forced oscillation was defined with a user defined function, or UDF. An example pf a UDF for a heave motion is given here. Please note that Fluent in 2D uses a different coordinate system from this thesis, it uses the y positive upwards for heave, from which follows x for sway, and z out of plane. The static real variables are replaced with appropriate values when preparing a simulation.

code D.1: UDF for an imposed heave motion

```
#include "udf.h"
#include "dynamesh_tools.h"
#include "math.h"

static real za = 0.05; /*heave*/
static real xa = 0.05; /*sway*/
static real omegas = 2.2; /* rad/s forcing of the system, wave freq*/
static real t0 = 0.0;
static real unk = 0.0;
static real Ux = 0.224;

DEFINE_CG_MOTION(heave,dt,vel,omega,time,dtime)
{
        NV_S(vel, =, 0.0);
        NV_S(omega, =, 0.0);
        vel[0] = 0.0;
        vel[1] = za * omegas * cos(omegas*(time-t0)+0.5*acos(-1.0)); /*velocity in
         ↪ heave*/
        omega[2] = 0.0;/* angular velocity =0.0*/
        if ( ( N_ITER % 15 ) == 1 )
        {
Message("\n time = %f, y_vel = %f, wavefreq= %f\n", time, vel[1], omegas); }
                FILE *sp;
                sp = fopen ("sdofmotion.txt", "a");      /* Open a file to add data to
                 ↪ the end */
if (CURRENT_TIME == CURRENT_TIMESTEP)
{
fprintf (sp, "\ncurrent_time,    dt,    cgx,    cgy,    theta,  velx,    vely,
 ↪ omega,       force_x,       \n");       /* Format output data file */
```

```
        }
fprintf (sp, "%e %e ", CURRENT_TIME, CURRENT_TIMESTEP); /* Current time in */
fprintf (sp, "%e %e ", unk , unk );     /* center of gravity position */
fprintf (sp, "%e ",  unk );        /* Angular position, degrees */
fprintf (sp, "%e %e ", vel[0] , vel[1] );   /* velocity at the center of gravity, m /
↪  s */
fprintf (sp, "%e ", omega[2] ); /* Angular velocity, rad / s */
fprintf (sp, "%e \n ", unk );
        fclose (sp);    /* Close the file */
}
```

For the cases where the barrier is free to move, another UDF was used to specify the properties. An example for a UDF for case dof-yz is shown here.

code D.2: UDF for a barrier free to move, dof-yz

```
#include "udf.h"
#include "dynamesh_tools.h"
#include "math.h"

DEFINE_SDOF_PROPERTIES(sdofs, prop, dt, time, dtime)
{
        real y0,k,y,x0,x,fx,thx,rad,offset;
        rad=radi;
        offset=xoffset;
        k = kspring; /* 0.04;*/ /*n/m*/
        y0 = y0rep;
        x0 = x0rep;
        y = DT_CG(dt)[1];
        x = DT_CG(dt)[0];
        thx= sin(DT_THETA(dt)[2])*0.18;
        fx=- k * (x  - x0 - thx -offset);

        prop[SDOF_MASS]          = mass0; /* mass */
        prop[SDOF_IZZ]           = Izz0; /* Inertia*/
        prop[SDOF_ZERO_ROT_Z]    = TRUE;/* Constraining the rotation around z, pitch
        ↪  */
        prop[SDOF_ZERO_TRANS_X]  = FALSE; /* Allowing the X-translation, sway */
        prop[SDOF_ZERO_TRANS_Y]  = False; /* Allowing the y-translation, heave  */
        prop[SDOF_LOAD_F_X]    = fx;

        FILE *sp;
        sp = fopen ("sdofmotion.txt", "a");     /* Open a file to add data to the end
        ↪  */
        if (CURRENT_TIME == t0)
        {                /* Format output data file */
fprintf (sp, "\ncurrent_time,    dt,    cgx,    cgy,    theta,  velx,    vely,
↪  omega,      force_x,      \n");
        }
fprintf (sp, "%e %e ", CURRENT_TIME, CURRENT_TIMESTEP); /* Current time in */
fprintf (sp, "%e %e ", DT_CG(dt)[0], DT_CG(dt)[1] );    /* center of gravity position
↪  */
fprintf (sp, "%e ",  DT_THETA(dt)[2] );       /* Angular position, degrees */
fprintf (sp, "%e %e ", DT_VEL_CG(dt)[0], DT_VEL_CG(dt)[1] );   /* Speed the center of
↪  gravity, m / s */
fprintf (sp, "%e ", DT_OMEGA_CG(dt)[2] ); /* Angular velocity, rad / s */
fprintf (sp, "%e \n ", fx );
```

```
        fclose (sp);    /* Closing the file */
}
```

code D.3: UDF for a ramped velocity inlet

```
#include "udf.h"
#include "dynamesh_tools.h"
#include "math.h"

static real Ux = 0.224;

DEFINE_PROFILE(rampt,t,i) /*ramp the current */
{
        real x[ND_ND];  /* this will hold the position vector */
        face_t f;
        real AAA;
        real curr_ts;
        curr_ts = N_TIME;
        real a;
        a = CURRENT_TIMESTEP;
        Message("Current timestepsize: %g\n", a);
        real time= RP_Get_Real("flow-time");
        Message("Current time: %g\n", curr_ts);
        AAA= tanh(time*2);
        Message("tanh value AAA: %g\n", AAA);
        Message("time time: %g\n", time);
        begin_f_loop(f, t)
        {F_CENTROID(x,f,t);
        F_PROFILE(f,t,i) =  AAA*Ux;
        }
end_f_loop(f,t)
}
```

D.3. MARIN model

Table D.2 shows the dimensions of the barrier and how it was scaled. The dimensions vary between the sources, were not documented or are missing. The scale model was measured and weighed by an intern of The Ocean Cleanup, [32]. The values measured do not correspond to the values given for full scale by [28] and [3], differences in the order 10 to 20 % were found.
The values delivered by Marin [28] and measured by Mettler, [32], were considered most accurate. The dimensions chosen for use in the numerical model can be found in Table 4.3.

Table D.2: Marin full scale and model scale [28], [32], [3], [8]

	Marin full scale	Unit	Marin model scale	Unit
Scale	1	$[m]$	5	$[m]$
Barrier width	13.1 [28]	$[m]$	2.62	$[m]$
Spring stiffness per spring	$4.74 \cdot 10^3$ [28]	$[N/m]$	189.6	$[N/m]$
Spring stiffness 4 springs	$18.96 \cdot 10^3$	$[N/m]$	758.4	$[N/m]$
Spring stiffness of 1 meter barrier	1447	$[N/m]$	289.46	$[N/m]$
Boom diameter	1	$[m]$	0.2	$[m]$
Skirt length	1.5 [3]	$[m]$	0.275[8] , 0.276 [32]	$[m]$
Skirt thickness		$[m]$	0.0055 [32]	$[m]$
Ballast diameter		$[m]$	0.025	$[m]$
Moment of inertia, I_{xx} per meter barrier		$[kg/m^2]$	0.17 [32]	$[kg/m^2]$
Mass	1860 [28]	$[kg]$	5.58 [32]	$[kg]$

E
Balance Equations

The system is governed by the following three physical principles,

- Mass is conserved
- Force equals mass times acceleration
- Energy is conserved

E.1. Reference frame

In general, a system is approached by either applying the balance equations on a finite control volume fixed in space with the elements moving through it, which is the Eulerian representation of the flow field, or by solving the balance equations on a finite control volume moving with the elements, which is the Lagrangian representation. The Eulerian and Lagrangian presentation of a flow field are visualised in Figure E.1, [2]:

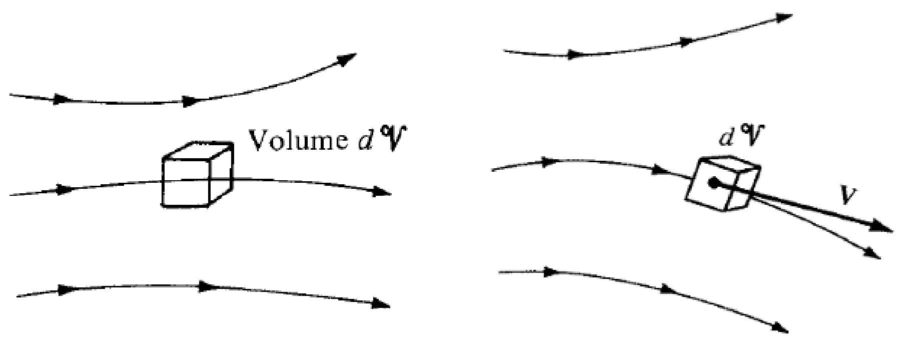

(a) Euler (b) Lagrange

Figure E.1: Control volume specification [2]

E.2. Governing equations

E.2.1. Continuity Equation

The continuity equation, Equation E.1, states that the mass flow out of a control volume through the surface S is equal to the decrease of the mass inside the control volume $\mathcal{V}$. In the following equation, ρ represents the density and the velocity vector is denoted by V:

$$\frac{\partial}{\partial t}\oiiint_{\mathcal{V}} \rho d\mathcal{V} + \oiint_{S} \rho \mathbf{V}\cdot\mathbf{dS} = 0 \tag{E.1}$$

By using the divergence theorem, $\oiint_S \mathbf{A}\cdot\mathbf{dS} = \oiiint_{\mathcal{V}} (\nabla\cdot\mathbf{A})d\mathcal{V}$, this can be rewritten to a partial differential equation:

$$\frac{\partial\rho}{\partial t} + \nabla\cdot(\rho\mathbf{V}) = 0 \tag{E.2}$$

For incompressible flows this reduces to

$$\nabla\cdot(\rho\mathbf{V}) = 0 \tag{E.3}$$

E.2.2. Momentum Equation

The momentum equation states that the time rate change of momentum is equal to the force, thus

$$\frac{d}{dt}(m\mathbf{V}) = \mathbf{F} \tag{E.4}$$

In Equation E.5, the left hand side contains the time rate change of momentum and the right hand side contains the surface forces, the body forces and the viscous force.

$$\frac{\partial}{\partial t}\oiiint_{\mathcal{V}} \rho\mathbf{V}d\mathcal{V} + \oiint_S (\rho\mathbf{V}\cdot\mathbf{dS})\mathbf{V} = -\oiint_S p\mathbf{dS} + \oiiint_{\mathcal{V}} \rho\mathbf{f}d\mathcal{V} + \mathbf{F}_{viscous} \tag{E.5}$$

Using the divergence theorem, this results in

$$\frac{\partial(\rho u_i)}{\partial t} + \nabla\cdot(\rho u_i\mathbf{V}) = -\frac{\partial p}{\partial x_i} - \rho f_i + \mathcal{F}_{i\ viscous} \tag{E.6}$$

Equation E.6 is also denoted as the Navier-Stokes Equation. If the flow is assumed to be inviscid, the viscous force $\mathbf{F}_{viscous} = 0$ drops out of the equation and results in the Euler equation.
In Equation E.6, $F_{x\ viscous}$ can be written as a summation of the shear stresses

$$F_{x\ viscous} = \frac{\partial t_{xx}}{\partial x} + \frac{\partial t_{yx}}{\partial y} + \frac{\partial t_{zx}}{\partial z} \tag{E.7}$$

The shear stresses are defined with the following equations, here $\lambda = -\frac{2}{3}\mu$,

$$\begin{aligned}
\tau_{yx} &= \tau_{xy} = \mu\left(\frac{\partial v}{\partial x} + \frac{\partial u}{\partial y}\right) & \tau_{xx} &= \lambda(\nabla\cdot\mathbf{V}) + 2\mu\frac{\partial u}{\partial x} \\
\tau_{yz} &= \tau_{zy} = \mu\left(\frac{\partial w}{\partial y} + \frac{\partial u}{\partial z}\right) & \tau_{yy} &= \lambda(\nabla\cdot\mathbf{V}) + 2\mu\frac{\partial v}{\partial y} \\
\tau_{zx} &= \tau_{xz} = \mu\left(\frac{\partial u}{\partial z} + \frac{\partial w}{\partial x}\right) & \tau_{zz} &= \lambda(\nabla\cdot\mathbf{V}) + 2\mu\frac{\partial w}{\partial z}
\end{aligned} \tag{E.8}$$

If starting with Equation E.6 the terms are expanded and compressibility is assumed,

$$u\nabla\cdot(\rho\mathbf{V}) + \rho\frac{\partial u}{\partial t} + (\rho\mathbf{V})\cdot\nabla u = -\frac{\partial p}{\partial x} - \rho f_x + \mathcal{F}_{x\ viscous} \tag{E.9}$$

The first two terms of Equation E.9 can be set to zero with the continuity equation, resulting in

$$\rho\frac{\partial u}{\partial t} + \rho\mathbf{V}\cdot\nabla u = -\frac{\partial p}{\partial x} - \rho f_x + \mathcal{F}_{x\ viscous} \tag{E.10}$$

Thus, x component of the Navier-Stokes equation, neglecting the body forces and implementing the stresses,

$$\begin{aligned}
&\rho\frac{\partial u}{\partial t} + \rho u\frac{\partial u}{\partial x} + \rho v\frac{\partial u}{\partial y} + \rho w\frac{\partial u}{\partial z} = -\frac{\partial p}{\partial x} + \frac{\partial}{\partial x}\left(\lambda\nabla\cdot\mathbf{V} + 2\mu\frac{\partial d}{\partial x}\right) \\
&+\frac{\partial}{\partial y}\left[\mu\left(\frac{\partial v}{\partial x} + \frac{\partial u}{\partial y}\right)\right] + \frac{\partial}{\partial z}\left[\mu\left(\frac{\partial u}{\partial z} + \frac{\partial w}{\partial x}\right)\right]
\end{aligned} \tag{E.11}$$

E.2.3. Energy Equation

The energy equation is stated on the third physical principle, energy can not be created or destroyed, it can only change form. The first law of thermodynamics states

$$de = \partial q + \partial w \tag{E.12}$$

In Equation E.12, de denotes the change in internal energy per unit mass, ∂q the amount of heat added to the control volume, ∂w represents the work done on the control volume.
This could also be formulated as th rate of change of energy of the control volume is equal to the rate of heat added to the control volume, plus the rate of work done on the control volume. In a similar fashion to the balance and momentum equation:

$$\begin{gathered}\frac{\partial}{\partial t}\oiiint_{\mathcal{V}} \rho(e+\frac{V^2}{2})d\mathcal{V} + \oiint_{S} \rho(e+\frac{V^2}{2})\mathbf{V}\cdot\mathbf{dS} = \\ \oiiint_{\mathcal{V}} \dot{q}\rho d\mathcal{V} + \dot{Q}_{viscous} - \oiint_{S} p\mathbf{V}\cdot\mathbf{dS} + \oiiint_{\mathcal{V}} \rho(\mathbf{f}\cdot\mathbf{V})d\mathcal{V} + \dot{W}_{viscous}\end{gathered} \tag{E.13}$$

which can be simplified to

$$\frac{\partial}{\partial t}\left[\rho\left(e+\frac{V^2}{e}\right)\right] + \nabla\cdot\left[\rho\left(e+\frac{V^2}{2}\mathbf{V}\right)\right] = \rho\dot{q} + \dot{Q}'_{viscous} - \nabla\cdot(p\mathbf{V}) + \rho(\mathbf{f}\cdot\mathbf{V}) + \dot{W}'_{viscous} \tag{E.14}$$

E.3. Dimensionless numbers

With dimensionless values parameters with different scales can be compared.

E.3.1. Reynolds number

The flow displays similar behaviour for similar ratios of inertial to viscous forces, also known as the Reynolds number, Re.

$$Re = \frac{\rho U L}{\mu} \tag{E.15}$$

E.3.2. Froude number

The Froude number, Fr is defined as the ratio between the inertia forces and the gravitational forces.

$$Fr = \frac{U}{\sqrt{gL}} \tag{E.16}$$

E.3.3. Keulegan Carpenter number

The Keulegan Carpenter number is defined as the ratio between drag forces and inertia and is sometimes called the period parameter. In this relation the velocity amplitude, U_m is used.

$$KC = \frac{U_m T}{D} \tag{E.17}$$

E.3.4. Strouhal number

The Strouhal number is defined as

$$St = \frac{D}{f_{st} U} \tag{E.18}$$

Where f_{st} represents the vortex shedding frequency.

E.3.5. Courant Friedrichs Lewy number

The Courant Friedrichs Lewy condition states that for the simulation to converge, the velocity of an element or wave moving through a cell should be smaller than the velocity of the simulation, which is equalt to the cell size divided by the time step.

$$C = \frac{u\Delta t}{\Delta x} \leq C_{max} \tag{E.19}$$

A multidimensional CFL number can be defined as

$$\text{CFL} = \frac{u_x \Delta t}{\Delta x} + \frac{u_y \Delta t}{\Delta y} \leq C_{max} \tag{E.20}$$

E.3.6. Coriolis force and the Rossby number

The Rossby numbers is a ratio of the convection to the Coriolis force, Equation E.21. When the Rossby number is smaller than 1, the Coriolis force is dominant.

$$Ro = \frac{U}{fL} \tag{E.21}$$

In this equation f describes the Coriolis force with $f = 2\Omega sin\phi$. Here Ω is the angular velocity of the earth, ϕ the latitude, U is the velocity and L is the length of the phenomenon. For a latitude of $\phi = 22°$, for a wave length of $L = 101m$ and a this results in a $Ro = 72$, thus the Coriolis force has no influence.